Study on Hydrogen Absorption Properties of Titanium with Surface Modification

（表面改質したチタンの水素吸蔵特性に関する研究）

学位取得年月　2020年9月

新里　恵多

Abstract

In this thesis, we focused on the Titanium (Ti) and hydrogen (H_2) system. The kinetics of H_2 absorption by Ti is quite slow, then the high temperature of 400 °C is required to realize the reaction. It is generally thought that the oxide layer formed on the Ti surface inhibits the hydrogenation. However, the hydrogenation properties of Ti without oxide layer has not been reported before, and the effective surface modification technique has not been proposed yet. In this thesis, the reaction between Ti with fresh surface and H_2 was studied to understand the essential reaction of Ti with H_2, and the surface modification techniques to improve the hydrogenation properties of Ti was also investigated.

It was clarified that the hydrogenation of Ti with fresh surface occurred even at room temperature. However, the active Ti is quite sensitive for not only hydrogen but also oxygen and water. The reactivity with H_2 was lost due to oxidation after keeping the sample for 1 day even in the highly purified Argon atmosphere with tiny amount of oxygen and water.

To make stable active sites for the hydrogenation of Ti, typical catalysts for H_2 dissociation were dispersed on the Ti surface. Although nickel, palladium, niobium (V) oxide, and vanadium (V) oxide were effective catalysts for hydrogenation of metals such as magnesium, significant effects on the hydrogenation were not observed for Ti. Thus, it was clarified that the influence of surface oxidation on the hydrogenation of Ti was much larger than the activation effects of solid additives. Considering the above results, it was thought that special surface, which can preserve the reactivity with H_2 and simultaneously prevent surface degradation such as the oxide layer formation, is required to improve the hydrogenation properties of Ti.

When Ti powder was ball-milled with organic solvents, such as xylene and acetone, the surface was effectively modified, and the characteristic surface showed high reactivity and selectivity for H_2 even at room temperature. The results of the characterization for the Ti modified by organic solvents samples indicated that graphite like structure is effective for the surface modification of Ti. Thus, the effects of graphite was investigated. As a result, the Ti with the excellent H_2 absorption properties was obtained by ball-milling with graphite. This sample can absorb H_2 at room temperature under 0.1 MPa H_2, and the reactivity was kept for more than 7 days although other samples prepared with organic solvents are inactivated within 1-4 days. From Raman spectrometry and TEM observation for the graphite-dispersed sample, it was identified that the mixed phase of turbostratic and amorphous carbons exists on the Ti surface. The mixed carbon phase can prevent the oxidation of Ti by the "hydrophobic adsorbent effects" for water and oxygen, while H_2 can pass through the carbon matrix. In addition, carbon-dissolved Ti phase (TiC_x) was found at the interface between Ti and carbons by electron energy loss spectrometry using transmission electron microscope. The TiC_x phase was also observed in the Ti ball-milled with acetone, which showed the effects of a function of porous inorganic membrane. Namely, the carbon matrix and the TiC_x layer showed the H_2 separation function.

From the experimental works in this thesis, it is clarified that Ti can essentially react with H_2 at room temperature without any catalyst, suggesting that the Ti surface it active for the dissociation of H_2. It is expected based on the above results that the surface with selective reactivity for H_2 without degradation of the active Ti surface by oxygen and water is effective as surface modification. In fact, formation of the above characteristic surface was achieved by ball-milling with graphite, and the excellent hydrogenation of Ti at room temperature without degradation were demonstrated.

Contents

1 Introduction

1.1 Sustainable energy

Recently, the problems with the limiting fossil fuel production and global warming are growing. Global warming is caused by greenhouse gases (GHG) such as CO_2 and methane, and it enhances the risks of climate change, sea-level rise, and so on. In order to suppress global warming, United Nations Framework Convention on Climate Change (UNFCCC) is found in 1992. In 2015, the 21st conference of the parties (COP21) was held in Paris. The target of suppressing the temperature rise less than 1.5~2 °C has been decided by Paris agreement in COP21. Then, all of the countries have submitted the aim of GHG emission reduction.[1] Thus, the establishment of sustainable energy society is required in the world. The aim of Japan on the Paris agreement is to reduce CO_2 emission to 26% by 2030. The proportion of utilization of renewable energy such as wind power, solar power, and so on, has to be increased in order to reduce the utilization of fossil fuels. However, the renewable energy is localized, and it has fluctuating output by weather and time. Therefore, the secondary energy must be necessary to maintain a balance between demand and supply. Hydrogen is one of the candidates for secondary energy sources because it can store energy chemically with high gravimetric energy density and can be produced from any kinds of primary energy. Especially, it is considered that hydrogen is suitable for the storage and transportation of large amount of energy compared to rechargeable batteries. Therefore, the technology of hydrogen utilization is required in the countries having less primary energy like Japan.

1.2 Metal-hydrogen systems

To establish the hydrogen utilization systems, the development of related technologies is strongly required. The metal-hydrogen systems are attractive in the field of various applications as described below.

Hydrogen storage

Hydrogen as a secondary energy source has the advantages of high abundance, high gravimetric energy density, and so on. However, the volumetric energy density is quite low because hydrogen is a gaseous state under an ambient temperature. In fact, the volumetric energy density of H_2 at 25 °C under 1atm is only 2.69 Wh/L (HHV), which is 2000 times smaller than liquid gasoline (even though considering energy loss).[2,3] Therefore, several kinds of methods must be developed to compactly store and transport H_2. It can be mainly classified by 3 types of hydrogen storage, which are compression, liquefaction, and solidification. In the case of the compression method, the energy density is 767 Wh/L at 35 MPa and 1290 Wh/L at 70 MPa, respectively. Here, this estimation is carried out without considering the weight of the H_2 tank although special H_2 tank for high pressure are necessary. The high pressure H_2 storage has the advantages such as temperature control is not necessary, and hydrogen can be supplied into H_2 tank rapidly. This method has been used for H_2 storage in hydrogen fuel cell vehicles at 70 MPa.[4] By liquefaction of H_2, the energy density is increased to 2330 Wh/L at −253 °C under 1 atm.[4] However, quite low temperature is necessary for liquefaction, which lead to energy loss. Japanese company (Kawasaki Heavy Industries, Ltd.) has been developing a ship for liquid hydrogen transportation from abroad.[5] As a third method, hydrogen can be stored in metals or alloys.[6,7] While the volumetric density depends on the metal, hydrogen can be compactly stored (2936 Wh/L) even at ambient conditions.[8–11]

Heat storage

As a renewable energy system, concentrating solar thermal power (CSP) system has been developing. In this system, electricity can be generated by turbine powered by solar heat. However, the amount of energy generation depends on the time and weather. Thus, heat storage system should be equipped with the solar heat power generation plant in order to maintain the energy supply round the clock.[12] The CSP systems can be classified in to 4 types, which have different types of the heat concentrator and the receivers as shown in figure 1.1. The operating temperatures of each system are shown in table 1.1. Molten-salt has been used as conventional heat storage materials for CSP. However, the utilization of molten-salt for high temperature (> 700 °C) suffers from the corrosion of container.[12] Thermochemical heat storage is one of the promising systems for high temperature heat storage because of its chemical stability, high energy density, theoretically unlimited storage period, and so on.[13,14] Metal-hydrogen system has also been studying for thermochemical heat storage. Although sensible heat and latent heat storage system cannot control the temperature, the operating temperature of metal-hydrogen system can be tuned by the pressure as shown in figure 1.2. The MgH_2 system reported by the group in Max-Planck Institute offers a heat storage material for concentrating solar thermal energy.[15] However, practical use of the Mg−H system is limited by following drawbacks: slow reaction kinetics, requirements of Fe- or Ni-doping, sintering at the high-temperature region, and high operating pressure around 10 MPa for utilizing around 500 °C.[14]

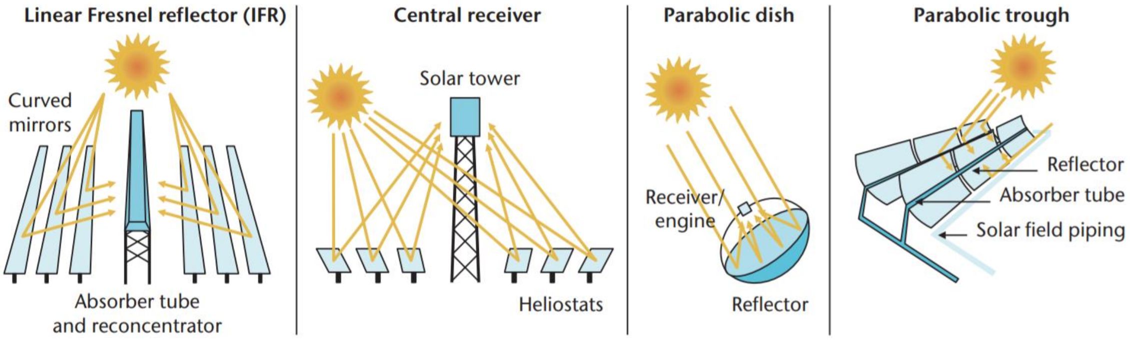

Figure 1.1 Concentrating Solar Power systems cited from IEA Technology Road map.[16]

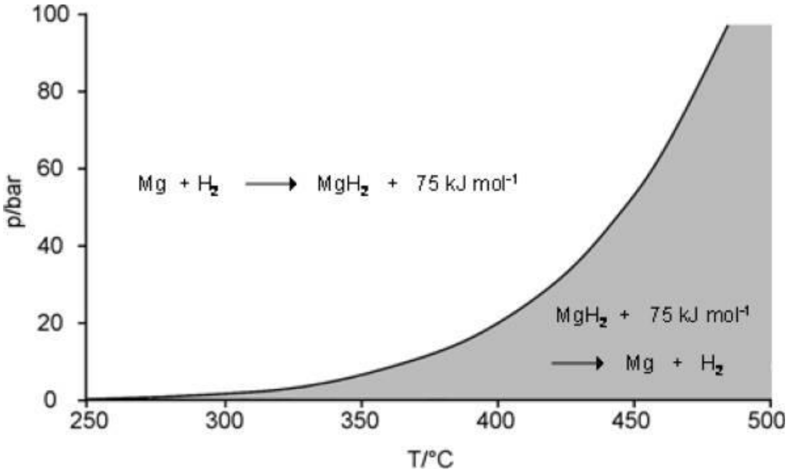

Figure 1.2 Dissociation pressure curve of MgH_2 suggested by Felderhoff *et al*.[15]

Table 1.1 CPS systems and its operating temperatures, the values were cited from report by NEDO.[17]

Types of CPS	Operating temperature (°C)	Efficiency (%)
linear Fresnel	< 400	8~10
parabolic trough	250~500	15
solar tower	850	20~35
dish-Stirling	750	25~30

Chemical compression

After introducing fuel cell vehicles with high pressure H_2 tank in the market in 2014, the hydrogen refueling station (HRS) is required to enhance the utilization of FCV. According to the strategic roadmap for hydrogen and fuel cells presented by Japanese government, the number of hydrogen refueling stations (HRS) will be increased to 320 by 2025, and 900 by 2030.[18] However, the number of HRS in May 2020 is still 131.[19] In order to increase the number of HRS, the cost cut is main issue. Japanese government presented that the cost of components should be decreased from 90 to 50 million yen for compressor, and 50 to 10 million yen for accumulator by early 2020s, respectively. Tsurui *et al.* pointed out that the moving part of mechanical compression is influenced by the hydrogen embrittlement, leading that the construction cost is extremely high to design the moving part with high strength.[20] The thermochemical compressor is one of the alternative methods of H_2 compression to reduce the cost of hydrogen refueling station because of its simplicity without moving part, safety and reliability, and the possibility to consume waste industrial heat.[20–22] When the metal hydride are heated under equilibrium H_2 pressure, the hydrogen pressure exponentially increases with increasing temperature according to van’t Hoff relation as explained in next section.[23,24] In our group, it was reported that H_2 could be compressed up to 82 MPa by only heating within 300 °C as shown in figure 1.3.[25]

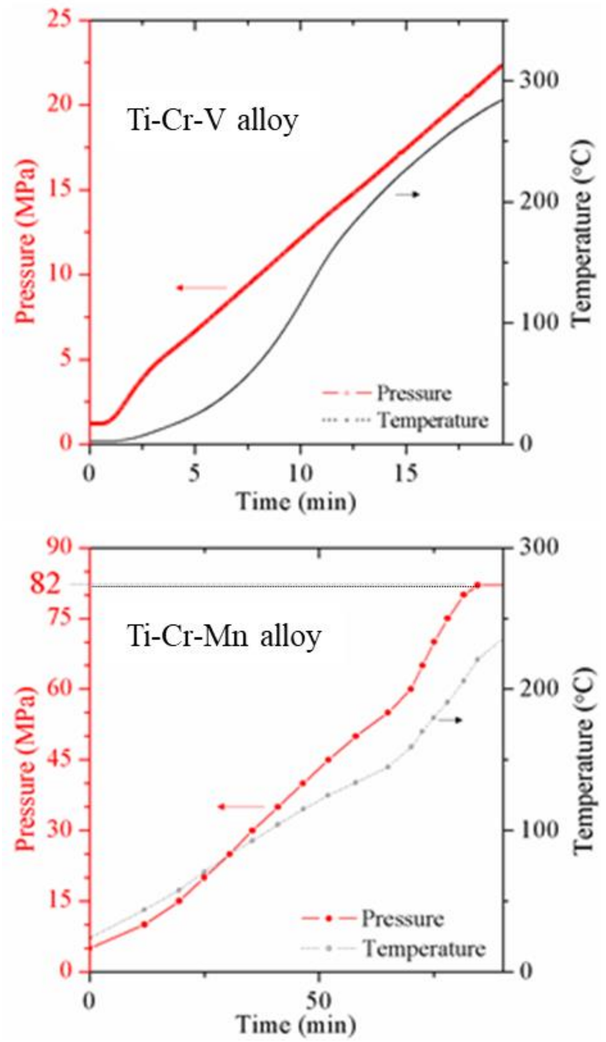

Figure 1.3 Hydrogen compression results by using 2 types of Ti-based alloys press-released by Hiroshima University (February, 2016).[25]

Hydrogen capture

Accidents of hydrogen leakage in closed areas are especially serious due to low ignition energy and wide explosion range of hydrogen (4-75 vol.% in air). Thus, hydrogen capture materials are required to prevent the hydrogen explosion and utilize hydrogen safely. In Japan, hydrogen explosion occurred in Fukushima Daiichi nuclear power plant accompanied by the great east Japan earthquake in 2011. According to the report on this accident, the electricity was totally lost due to the tsunami, then the safety systems were not working.[26] To prevent hydrogen explosion even without the electricity supply, several kinds of methods are presented.[27,28] The metal-hydrogen system is a promising method because some metals can absorb hydrogen automatically below the H_2 explosion limit.[29] The reaction between Mg and H_2 has been studied as a hydrogen capture material.[30]

1.3 Thermodynamics and kinetics

Thermodynamics

Thermodynamics of the reaction between hydrogen and metal is an important factor in order to understand the hydrogen absorption/desorption properties. Figure 1.4 shows the hydrogen absorption curve of $LaNi_5$, a well-known as hydrogen storage material, performed at a fixed temperature. When the hydrogen is introduced gradually, hydrogen pressure is increased from 0.0 to 0.2 MPa. As shown by the inserted figure in the figure 1.4, the hydrogen content is slightly increased with increasing pressure. The phenomenon indicates the formation of solid solution (MH_x) in this region. When the pressure exceeds more than 0.2 MPa, the hydrogen pressure remains constant even though supplying hydrogen continuously, and so the hydrogen content increases to H/M = 6. The region is called the plateau region. The following equilibrium reaction occurs in the plateau region,

$$\mathrm{LaNi_5} + 3\mathrm{H_2} \leftrightarrow \mathrm{LaNi_5H_6}. \qquad \text{(Equation 1.1)}$$

In this region, the ratio of $LaNi_5/LaNi_5H_6$ keep changing. After fully conversion of $LaNi_5$ to $LaNi_5H_6$, the hydrogen pressure starts increasing again.

According to the Gibbs' phase rule, the degrees of freedom (f) can be given by,

$$f = c - p + 2, \qquad \text{(Equation 1.2)}$$

in which c and p are the number of components and phases in the system, respectively. In the region of solid solution, the number of components and phases are 2. Here, the phase of solid solution is regarded as the same phase as metal (M). Thus, f can be calculated to be 2, indicating that the pressure and H content can be chosen freely. In the case of plateau region, the components and the phases are 2 and 3, respectively (the phases of M and MH_2

are distinguished). Therefore, *f* is calculated as,

$$f = 2 - 3 + 2 = 1. \qquad \text{(Equation 1.3)}$$

This equation indicates that only 1 freedom can be chosen from the temperature, H content, and the pressure. Thus, the temperature and pressure should be fixed in the plateau region as shown in figure 1.4.

The formation of solid solution can be written as following reaction,

$$M + \frac{x}{2}\mathrm{H}_2 \leftrightarrow M\mathrm{H}_x. \qquad \text{(Equation 1.4)}$$

In the region of solid solution, the chemical potential of hydrogen gas (μ_g) is equal to that of hydrogen dissolved in α phase (μ_α) as follows,

$$\frac{1}{2}\mu_g = \mu_\alpha. \qquad \text{(Equation 1.5)}$$

Based on ideal gas, the chemical potential of the hydrogen molecule (μ_g) under temperature (T) and pressure (p) can be written by,

$$\mu_\mathrm{g} = kT\ln\left(\frac{p}{p_0}\right) - E_\mathrm{d}, \qquad \text{(Equation 1.6)}$$

where, k is the Boltzmann constant, p_0 is the pressure under the standard condition, and E_d is the energy for the dissociation of hydrogen molecule. Now, the starting point of chemical potential is described from the dissociated hydrogen molecule (2H), so that E_d is included in Equation 1.6. On the other hand, Gibbs free energy of the solid solution phase (G_a) is given by,

$$G_\alpha = H_\alpha - TS_\alpha, \qquad \text{(Equation 1.7)}$$

in which H_α and S_α are enthalpy and entropy of the solid solution phase, respectively. The enthalpy of the solid solution phase ($M\mathrm{H}_x$) is

$$H_\mathrm{a} = xh_\mathrm{a}, \qquad \text{(Equation 1.8)}$$

where, x is the number of the dissolved hydrogen atom and h_a is the dissolution enthalpy of 1 atom. The entropy can be separated by the configurational entropy (S_c) and the excess entropy of solution (S_e),

$$S_\mathrm{a} = S_\mathrm{c} + S_\mathrm{e}. \qquad \text{(Equation 1.9)}$$

S_c can be given by Boltzmann's equation using the configuration number (W),

$$\begin{aligned} S_\mathrm{c} &= k\ \ln(W) = k\ \ln\ (r\mathrm{C}x) \\ &= k\ \ln\ \left(\frac{r!}{x!(r-x)!}\right), \end{aligned} \qquad \text{(Equation 1.10)}$$

where, k is the Boltzmann constant, and r is the number of initial sites of metal for the hydrogen atoms. Equation 1.10 can be expressed by Stirling's approximation as follows,

$$\ln(n!) = n\ln(n) - n, \qquad \text{(Equation 1.11)}$$

with $$S_\mathrm{c} = kr\ \ln\ \left(\frac{r}{r-x}\right) - kx\ ln\left(\frac{x}{r-x}\right). \qquad \text{(Equation 1.12)}$$

The excess entropy of solution (S_e) can be expressed as follows,

$$S_\mathrm{e} = xs_\mathrm{e}. \qquad \text{(Equation 1.13)}$$

Therefore, by using equation 1.7-9, 1.12, and 1.13, the chemical potential of the solid solution phase (μ_a) can be given as follows,

$$\mu_a = \frac{\partial G_a}{\partial x} = h_\mathrm{a} - Ts_\mathrm{e} + kT\, ln\left(\frac{x}{r-x}\right). \qquad \text{(Equation 1.14)}$$

From equation 1.5, 1.6, and 1.14, the equilibrium condition can be written by,

$$\frac{1}{2}\left\{kT \ln\left(\frac{p}{p_0}\right) - E_\mathrm{d}\right\} = h_\mathrm{a} - Ts_\mathrm{e} + kT \ln\left(\frac{x}{r-x}\right) \qquad \text{(Equation 1.15)}$$

Because x is quite small ($x \ll r$) in the region of solid solution,

$$\ln\left(\frac{x}{r-x}\right) = \ln(x) - \ln(r). \qquad \text{(Equation 1.16)}$$

Therefore, the following equation is derived from equation 1.15 and 1.16,

$$\left(\frac{p}{p_0}\right)^{\frac{1}{2}} = K_\mathrm{s}(T) \cdot x, \qquad \text{(Equation 1.17)}$$

$$K_\mathrm{s}(T) = \exp\left(\frac{Ts_e - h_a - \frac{1}{2}E_\mathrm{d} + kT\ln(r)}{kT}\right), \qquad \text{(Equation 1.18)}$$

Equation 1.17 is known as Sievert's law, and $K_\mathrm{s}(T)$ is called Sievert's constant. Because K_s is more than 0, small amount of hydrogen can be dissolved in every material.

At the plateau region, the formation of metal hydride occurs as following reaction,

$$M + \mathrm{H}_2 \leftrightarrow M\mathrm{H}_2. \qquad \text{(Equation 1.19)}$$

The Gibbs free energy change (ΔG) of the above reaction can be written by,

$$\Delta G = \Delta H - T\Delta S \qquad \text{(Equation 1.20)}$$

here, ΔH and ΔS are enthalpy change and entropy change for the reaction, respectively. In the case of hydrogen absorption reaction, ΔH_abs and ΔS_abs are given by,

$$\Delta H_\mathrm{abs} = H_{M\mathrm{H2}} - (H_M + H_\mathrm{H2}) = H_{M\mathrm{H2}} - H_\mathrm{M} = \Delta H_\mathrm{f}, \qquad \text{(Equation 1.21)}$$

$$\Delta S_{\mathrm{abs}} = S^0_{M\mathrm{H2}} - (S^0_M + S_{\mathrm{H2}}), \qquad \text{(Equation 1.22)}$$

where, ΔH_f is the formation enthalpy of hydride. The entropy of gaseous hydrogen S_{H2} can be expressed by,

$$S_{\mathrm{H2}} = S^0_{\mathrm{H2}} - \mathrm{R}\ln(\frac{p}{p_0}), \qquad \text{(Equation 1.23)}$$

where, $\mathrm{S_{H2}}^0$ is the standard entropy under p_0 and R is gas constant. When the hydrogen absorption and desorption is in the equilibrium ($p = p_{\mathrm{eq}}$), Gibbs free energy change for hydrogenation is 0. Therefore, the above equations can be rearranged as follows,

$$\Delta H_{\mathrm{abs}} = T\Delta S_{\mathrm{abs}}, \qquad \text{(Equation 1.24)}$$

$$\Delta H_{\mathrm{abs}} = T\Delta S^0_{\mathrm{abs}} + \mathrm{R}T\ln(\frac{p_{\mathrm{eq}}}{p_0}), \qquad \text{(Equation 1.25)}$$

$$\ln\left(\frac{p_{\mathrm{eq}}}{p_0}\right) = \frac{\Delta H_{\mathrm{abs}}}{\mathrm{R}T} - \frac{\Delta S^0_{\mathrm{abs}}}{\mathrm{R}}. \qquad \text{(Equation 1.26)}$$

Here, p_{eq} is equilibrium pressure of the reaction. Equation 1.26 is known as van't Hoff equation. Thus, the enthalpy and entropy changes of hydrogen absorption can be experimentally known by the plots of ln (p_{eq}/p_0) versus $1/T$. Figure 1.5 shows pressure-concentration-isotherm curves and the van't Hoff plot.[31]

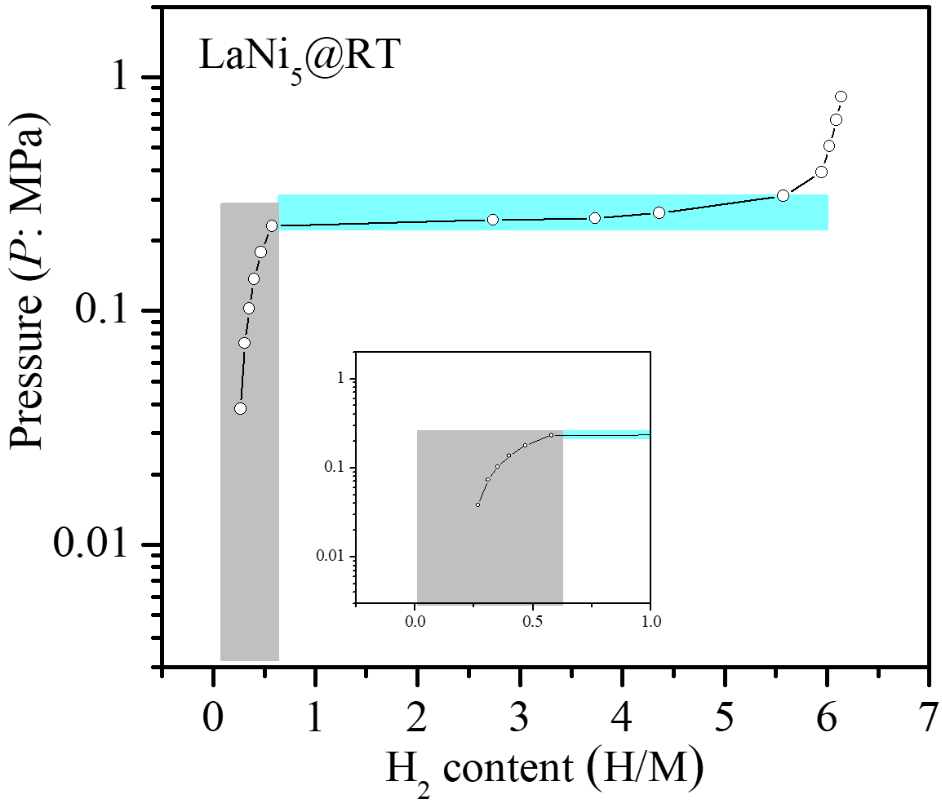

Figure 1.4 hydrogen absorption curve of LaNi$_5$ performed at room temperature.

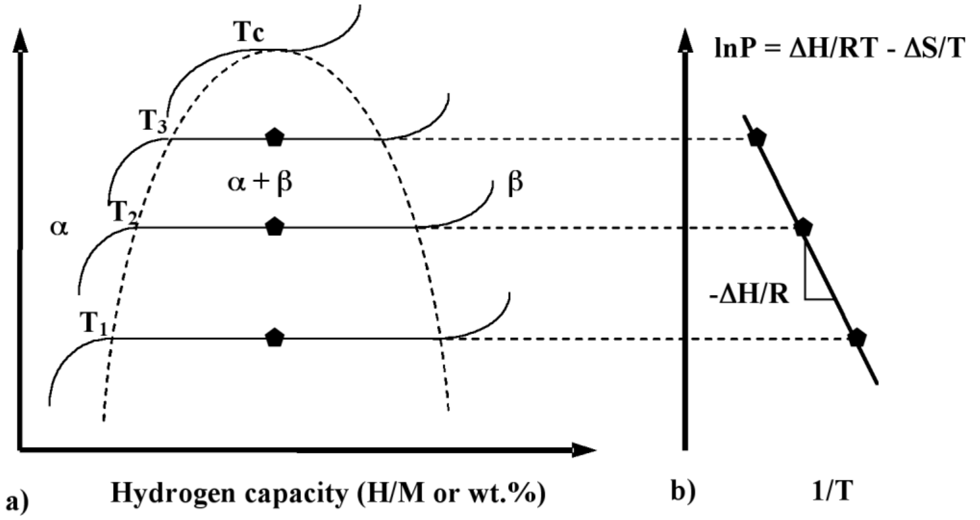

Figure 1.5 (a) Pressure-Concentration-Isotherm curves with different temperatures and (b) the van't Hoff plot, which figures were presented by ref. [31].[31]

Kinetics

The analyses of reaction kinetics can reveal the reaction rate of the reaction, which can thermodynamically proceed. The hydrogen absorption reaction by a metal proceeds by following steps,

(1) physisorption of gaseous H_2 molecule on a metal surface,

(2) dissociation of H_2 molecule into H atoms, and chemisorption of H atoms on metal surface,

(3) surface migration of H atoms into bulk,

(4) diffusion of H atom in bulk of metal, and formation of solid solution phase,

(5) nucleation of the hydride phase (β phase).

If it is assumed that H_2 molecule approaches a metal from the perpendicular direction to the metal surface, the energy diagram of physisorption U (Z) can be described as one-dimensional Lennard-Jones potential, as shown in figure 1.6a. When H_2 molecule approaches a metal surface by distance Z_{phys} from the surface, H_2 molecule interact with the surface through van der Waals attractive force. This interaction is originated in the small polarizability of H_2 molecule. Therefore, the interaction of physisorption is quite small with energy in the range of 3~15 kJ/mol H_2.[32] If the distance Z decreases to less than Z_{phys}, the Coulombic repulsive force is generated between H_2 and metal. In the case of physisorption, covalent bond is not formed between H_2 molecule and metal surface. On the other hand, H atom shows different interaction from physisorption. When two H atoms approach a metal surface, strong attractive interaction originates between H atoms and metal surface. Because H atoms and the surface atoms interact by chemical bonding, the depths of the potential wells are larger than that of physisorption. This interaction is called chemisorption, and the energy of chemisorption is in the range of 500 to 600 kJ/mol H_2.[32] Figure 1.6b shows the potential energy in the case of chemisorption. The figure start from 431 kJ/mol H_2, which is dissociation energy of H_2 molecule, because the zero point is described as the energy of H_2 molecule. Therefore, the energy with more than 431 kJ/mol H_2 has to be supplied firstly to dissociate H_2 molecule in order to form the chemisorption state. However, the temperature more than 1000 °C is required to dissociate H_2 molecule due to large value of the dissociation energy.[33] This fact indicates that the dissociation could not occur at room temperature. On the other hand, it is known that the dissociation of H_2 molecule is easily observed on a metal surface due to its catalytic effect. The combination of the figure 1.6a and 1.6b is shown in figure 1.6c. Molecular hydrogen approaches a metal surface, and then the H_2 molecule is dissociated into 2H atoms at the point P, which exists near Z_{phys}. In the case of figure 1.6c, the crossover point P is below $E = 0$, indicating the spontaneous dissociation of H_2 molecule would happen. Thus, hydrogen can be chemisorbed on a metal surface without supplying large amount of activation energy. Table 1.2 shows the values of adsorption energy of hydrogen on metals. The binding energy of H atom and a metal surface ($E_{\mathrm{Me-H}}$) can be given by,

$$E_{\mathrm{Me-H}} = \frac{E_{ad}+E_{\mathrm{d}}}{2}. \qquad \text{(Equation 1.27)}$$

When molecular H_2 is closer than Z_{phys}, the electrons of surface are donated to antibonding molecular orbitals (σ^*) of H_2. Then intramolecular bond of H_2 is destabilized, and make Metal-H bond. This indicates that the dissociation ability depends on the electronic structure of the metal surface. The H_2 dissociation ability of light elements, which have no *d*-electrons, are low compared with transition metals having *d* orbital-electron.

After the chemisorption, H atoms pass through the sub-surface layer of metal. Figure 1.7 shows a schematic diagram of potential energy from physisorption to diffusion of hydrogen molecule or atoms. The blue solid and dotted lines are the potential curves without and with considering reconstruction of surface atoms, respectively. In the case of potential curve with considering reconstruction of surface atoms, the activation energy for jumping the sub-surface layer is lower than that without considering reconstruction. This indicates that the reconstruction of surface atoms is important for permeation of H_2 into bulk of metal. Then the chemisorbed H atoms diffuse in the bulk when H atom obtains the activation energy E_{diff}. The activation energy for hydrogenation (E_{hydr}) which include several steps, can be drawn as figure 1.7. Usually, the step having the highest activation energy controls the reaction rate and is called as rate-controlling step. In the initial stage of hydrogen absorption processes, this rate controlling step is chemisorption of hydrogen, whereas it changes to the hydrogen diffusion with the increase of hydrogen concentration in the metal.

As a macroscopic view point, the reaction velocity (v) of hydrogen absorption by metal can be given as follows when the reaction is assumed as first-order reaction,

$$v = -\frac{dx}{dt} = kx, \qquad \text{(Equation 1.28)}$$

here, k is reaction constant and x is the concentration of the reactant. This equation indicates the reaction kinetics is faster with a larger value of k and x. The reaction constant can be expressed as,

$$k = k_0 \exp(-\frac{E_{\mathrm{a}}}{\mathrm{R}T}), \qquad \text{(Equation 1.29)}$$

where, k_0 is called the frequency factor, and the term of exponential is known as the

Boltzmann factor, and E_a is the activation energy for the reaction. E_a includes many kinds of activation energy for the reaction steps such as a surface reaction and hydrogen diffusion as discussed before. The frequency factor k_0 represents the frequency of collision with reactants. In the case of solid-gas reaction like hydrogen absorption, the frequency factor can be enhanced by increasing the hydrogen pressure and the number of active sites for reaction. It is reported that the hydrogen absorption kinetics of hydrogen storage materials can be enhanced by increasing the surface area that can be achieved by ball-milling.[34] The reduction of particle size also affects the hydrogen diffusion. Basically, the hydrogen diffusion rate can be improved by increasing temperature. On the other hand, if the particle size is reduced, the high diffusion rate is not necessary to enhance the reaction yields as shown in figure 1.5. The term of exponential represents the probability, where the reactant has energy E_a at the temperature T. If the rate-controlling step is the hydrogen dissociation on the surface, the activation energy can be decreased by adding a suitable catalyst. Kimura *et al.* reported that the activation energy for hydrogen absorption of Mg catalyzed by Nb_2O_5 was lowered down to 31 kJ/mol H_2 from 61 kJ/mol H_2 of Mg without catalyst.[35] Figure 1.6 shows the curve of the Boltzmann factor drawn by using the activation energy of the ball-milled Mg with and without Nb_2O_5. It can be seen that the value of the Boltzmann factor drastically increases when the temperature exceeds over a turning temperature (100 and 250 °C for Mg with and without Nb_2O_5, respectively). This indicates that the reaction rate is drastically increased from those temperatures. In addition, it can be understood that the turning temperature is lower with smaller activation energy as shown in figure 1.6. Therefore, when it is assumed that the frequency factors of samples are the almost same value, the activation energy can be relatively compared by measuring the onset temperature of the reaction.

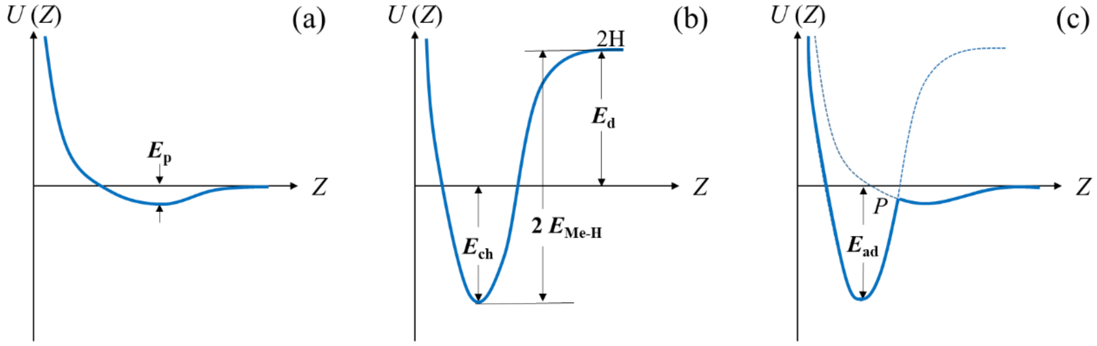

Figure 1.6 Potential diagram of (a) physisorption, (b) chemisorption, and (c) combined schematic of physisorption and chemisorption.[32]

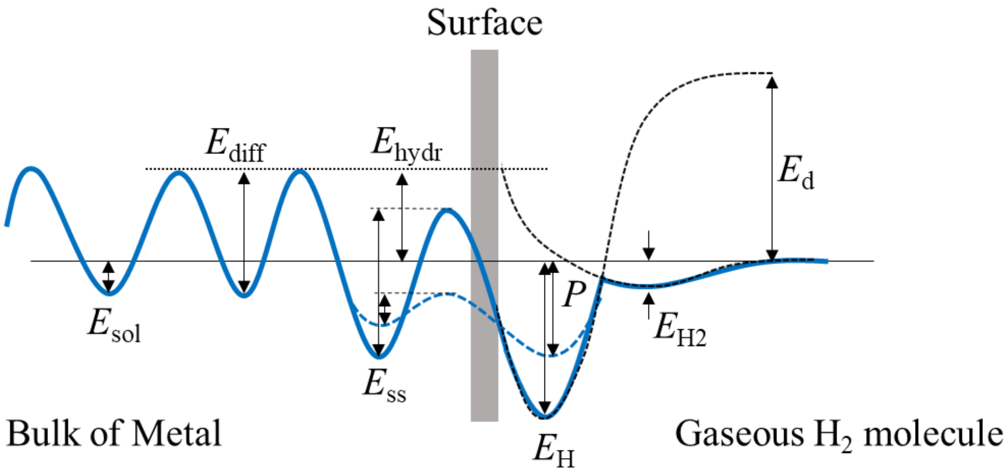

Figure 1.7 Hydrogen migration and diffusion into the bulk of metal. E_{sol} is heat of solution, E_{diff} is activation energy for bulk diffusion, E_{ss} is activation energy for desorption from the H subsurface sites, E_{hydr} is activation energy for hydrogenation, E_{H} is activation energy for desorption from the chemisorbed state, E_{H2} is adsorption energy of the physisorbed H_2, and H_{d} is heat of dissociation of H_2 molecule. This figure is drawn by referring to previous paper reported by Christmann.[32]

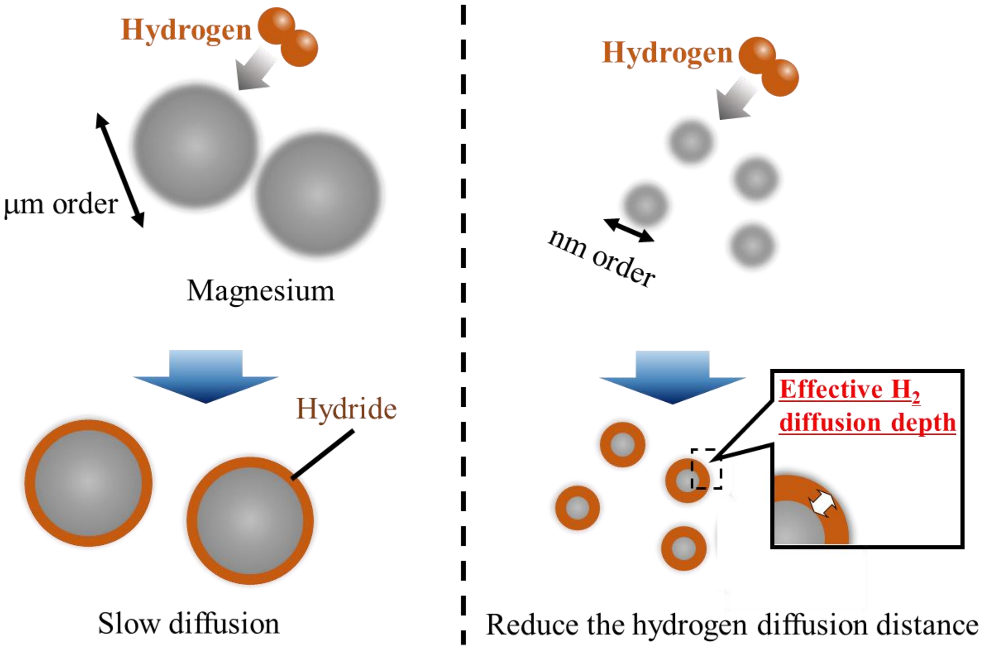

Figure 1.8 Scheme of reaction yields with different particle sizes. The reaction yields can be improved by the reduction of particle size even the same diffusion rate.

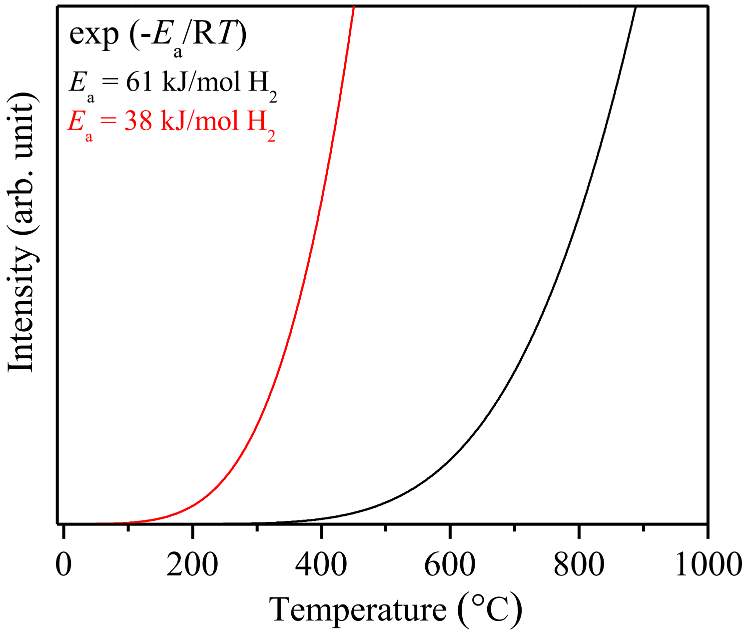

Figure 1.9 The curve of exp (−Ea/R*T*) versus T. The activation energy of Mg with and without catalyst, which was measured by Kimura *et al.*, were used to draw this figure.[35]

Table 1.2 The adsorption energy ($E_{\mathrm{ad,\,0}}$) at the initial state and binding energy between metal and a hydrogen atom ($E_{\mathrm{Me\text{-}H}}$) presented by Christmann.[32]

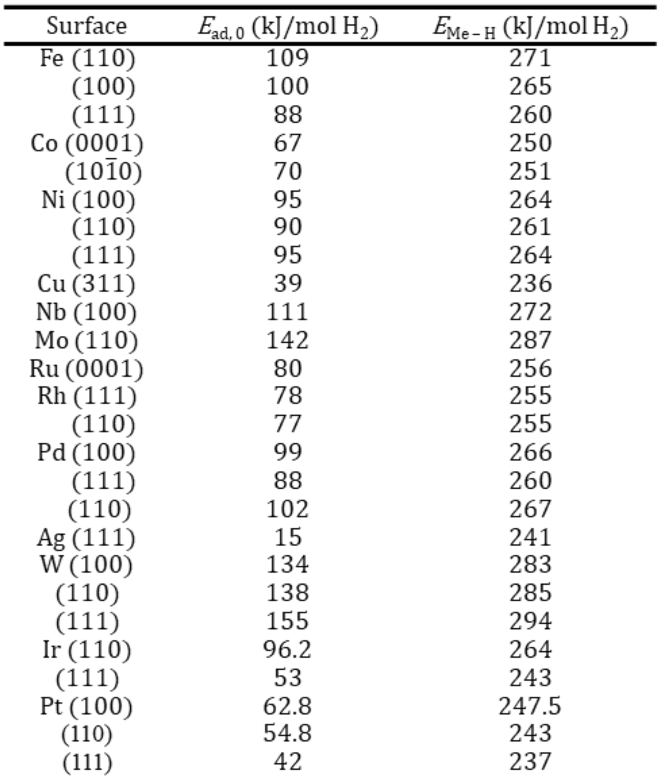

Surface	$E_{\mathrm{ad,\,0}}$ (kJ/mol H_2)	$E_{\mathrm{Me-H}}$ (kJ/mol H_2)
Fe (110)	109	271
(100)	100	265
(111)	88	260
Co (0001)	67	250
$(10\bar{1}0)$	70	251
Ni (100)	95	264
(110)	90	261
(111)	95	264
Cu (311)	39	236
Nb (100)	111	272
Mo (110)	142	287
Ru (0001)	80	256
Rh (111)	78	255
(110)	77	255
Pd (100)	99	266
(111)	88	260
(110)	102	267
Ag (111)	15	241
W (100)	134	283
(110)	138	285
(111)	155	294
Ir (110)	96.2	264
(111)	53	243
Pt (100)	62.8	247.5
(110)	54.8	243
(111)	42	237

1.4 Surface modification for metal-hydrogen system

In metal-hydrogen systems, hydrogen is absorbed through the metal surface. Therefore, the surface of the metal should be active for hydrogen absorption. To produce an active surface, several methods of surface modification have been studied. In simple understanding is *d*-electrons of transition metal can effectively dissociate molecular H_2 as mentioned in section 1.3. However, light elements such as Mg do not have *d*-electrons, indicating that it is difficult to dissociate H_2 molecule into atoms on the surface of these elements. It is reported that transition metals can catalyze the hydrogen dissociation for hydrogen absorption of Mg. On the other hand, although transition metals have the dissociation ability for H_2, the stable oxide layer formed on the surface of metals inhibits the permeation of hydrogen into the bulk. Therefore, initial activation is required to generate a fresh surface.

Surface modification of light element

Metal hydrides composed of light elements such as LiH, NaH, MgH_2, and CaH_2, have a high gravimetric hydrogen density. However, high temperature is required to desorb hydrogen because those metal hydrides are quite stable. Among them, MgH_2 can reversibly react with hydrogen at relatively low temperature as follows,[36]

$$MgH_2 \leftrightarrow Mg + H_2. \qquad \text{(Equation 1.30)}$$

However, the kinetics of hydrogen absorption/desorption reaction is quite slow and high temperature of more than 300 °C is required to realize the above reaction.[37] It is caused by the less surface reactivity of Mg itself for H_2. In order to improve the kinetics, many kinds of additives, which have a high dissociation ability towards H_2, have been investigated to find suitable catalyst since 1970s.[38] Especially, several kinds of transition metals have been investigated as catalysts.[37,39] Furthermore, the catalytic effects of metal oxides such as TiO_2, V_2O_5, Cr_2O_3 etc. have been also reported.[40,41] Barkhordarian *et al.* presented that Nb_2O_5 has remarkable catalytic effects for the hydrogen absorption kinetics of Mg compared to other metal oxides.[42] Kimura *et al.* reported that Mg catalyzed by Nb_2O_5 absorbs hydrogen even at −60 °C.[35] In addition to transition metals and their oxides, there are numerous reports on the catalytic effects of chemical compounds, such as halides, carbides, and hydrides.[43–45] Ma *et al.* investigated the hydrogen storage properties of MgH_2 with titanium compounds (TiF_3, $TiCl_3$, TiO_2, TiN, and TiH_2) systematically. Although Mg without any catalysts did not absorb hydrogen under 2 MPa H_2 at 150 °C, the composites of Mg and titanium compounds absorb hydrogen at the same conditions.[46] As another approach for the improvement of hydrogen absorption kinetics of Mg, the effects of organic materials during ball-milling of Mg have been investigated.[47,48] Imamura *et al.* investigated the effects of several kinds of organic additives for the hydrogen absorption/desorption reaction of Mg systems.[47,49] Especially, they have studied the composite of Mg and graphite ball-milled with organic solvents. The solid-phase reaction between magnesium and graphite can be controlled by organic solvents, and the additives can prevent the excessive breakage of graphite.[49]

Surface Modification of transition metal

Titanium-based alloys are one of the promising hydrogen storage materials because of their low cost compared to conventional alloy ($LaNi_5$). Among the titanium alloys, TiFe is attracting because of its suitable thermodynamic properties for hydrogen absorption/desorption reactions at room temperature. However, high temperature (≥400 °C) and high pressure (≥ 6 MPa) are required to activate the pristine TiFe, while $LaNi_5$ can be easily activated even at 20 °C under 5 MPa H_2. Schlapbach *et al.* have investigated the surface state of $LaNi_5$ and TiFe by X-ray photoelectron spectroscopy (XPS) and Auger electron spectroscopy (AES). Their results showed that the surface of both non-activated alloys were covered by La_2O_3 and TiO_2, respectively as shown by the schematic in figure 1.7. On the other hand, Fe existing on the TiFe surface can also be oxidized easily, while Ni on the $LaNi_5$ surface remains as metallic state. Usually, the transition metals are known to have the ability of H_2 dissociation nevertheless lose this property upon oxidation. Therefore, they concluded that Ni can catalyze hydrogen absorption of $LaNi_5$, while Fe cannot catalyze hydrogen absorption in case of TiFe. Schlapbach *et al.* also reported that the precipitation of metallic Fe occurred at high temperature (200-400 °C), and then TiFe becomes active for H_2.[50,51]

In order to overcome the drawback of TiFe, several studies of surface modification have been reported. Fresh surface can be created by high energy ball-milling. Aoki *et al.* have reported that the ball-milling effect under inert gas for initial activation of TiFe, which could absorb hydrogen even at 10 °C under 2 MPa H_2.[52,53] In addition, Chiang *et al.* performed the ball-milling of TiFe under 0.5 MPa H_2 and hydrogen absorption occurred during ball-milling.[54] However, the ball-milled sample was inactivated after exposing to air and then the reactivation was required. As another approach, the partial substitution of Ti or Fe in TiFe by third elements has been widely investigated in order to obtain the $Ti_{1-x}Fe_{1-y}A_xB_y$ alloys, which could be more easily activated. Bounudina *et al.* reported that $TiFeNi_x$ could absorb H_2 at room temperature under 2 MPa H_2 even after exposing in air. Lee *et al.* have systematically investigated the effect of partial substitution of Fe in TiFe by 3d metals (Cr, Mn, Co, Ni), then these alloys absorbed hydrogen at room temperature without activation.[55,56] For the substitution of Ti in TiFe, there is a report on the effects of zirconium substitution, which could be activated at 400 °C under 1 MPa H_2

although it was not so effective compared to the substitution of Fe.[57] In addition, Mizuno *et al.* have investigated the effect of Ti concentration in $TiFe_x$.[58] The stable phases of Ti-Fe are TiFe and $TiFe_2$, and the TiFe phase has a composition range of $0.98 < Ti/Fe < 1.08$ at room temperature. They revealed that $Ti_{1.2}Fe$ can be hydrogenated at room temperature under 3 MPa without activation, whereas the hydrogenation kinetics of $Ti_{1.05}Fe$ at the same condition was quite slow. As an interesting report, Emami *et al.* succeeded in the activation of TiFe by ball-milling with an organic solvent. In addition, the TiFe sample could be easily activated by the only evacuation at 150 °C for 2 h even though after exposing in air for 1 month.[59] However, the activation mechanism is not well understood until now.

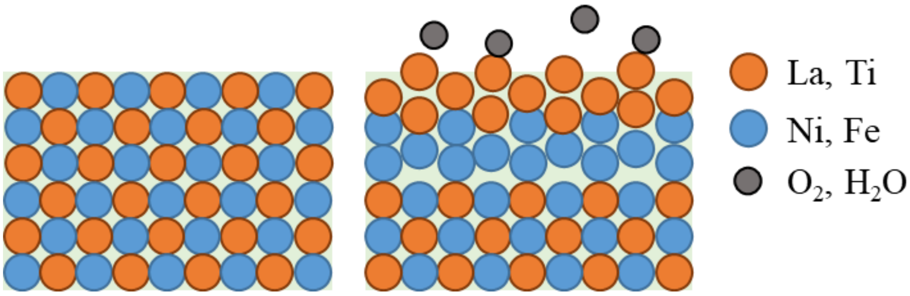

Figure 1.10 Scheme of illustration for surface segregation of alloys

1.5 Titanium-hydrogen system

Many researchers have investigated the thermodynamic properties of the Ti-H system to describe the phase boundaries by experimental or theoretical analyses.[60–63] Titanium can react with hydrogen, and it forms hydride with a various compositions which are classified by 4 kinds of phases, i.e. α, β, δ, and ε phase as shown in figure 1.11.[62] Figure 1.12 shows PCI curves measured by Haag *et al.*[60] at different temperatures, where 300 °C is the lowest temperature so far, although there are results at 250 °C also which were measured by electrochemical technique.[64] The PCI curves indicated that Ti (α phase) was directly transformed into δ phase at 300 °C, while the transformation occurred through β phase at 400 °C. However, quite long time is needed to reach the equilibrium pressure due to slow kinetics at low temperature. TiH_2 has quite low dissociation pressure (10^{-17} Pa at 25 °C) due to large enthalpy change (TiH_2, −142 kJ/mol H_2[61]). It is known that hydrogen absorption of Ti is inhibited by surface oxide layer at low temperature. Hadjixenophontos *et al.* investigated the role of surface oxides on hydrogen absorption kinetics of titanium by using Ti thin film courted by various thickness of TiO_2. They mentioned that the rate-controlling step of the hydrogenation by Ti is the H diffusion through the surface oxide layer. They succeeded the room-temperature hydrogenation of Ti coated by Pd film. Since Pd is well known as a catalyst for H_2 dissociation, it is still unknown that Ti itself is active or not for H_2.

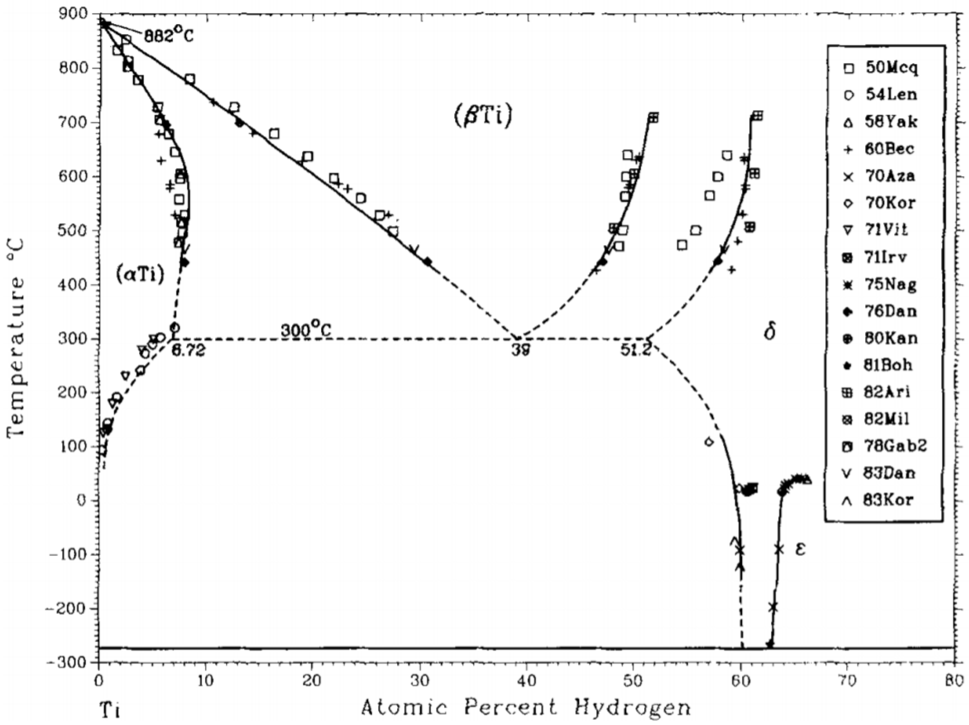

Figure 1.11 Phase diagram of Ti-H presented by *San-Martin et al.*[62]

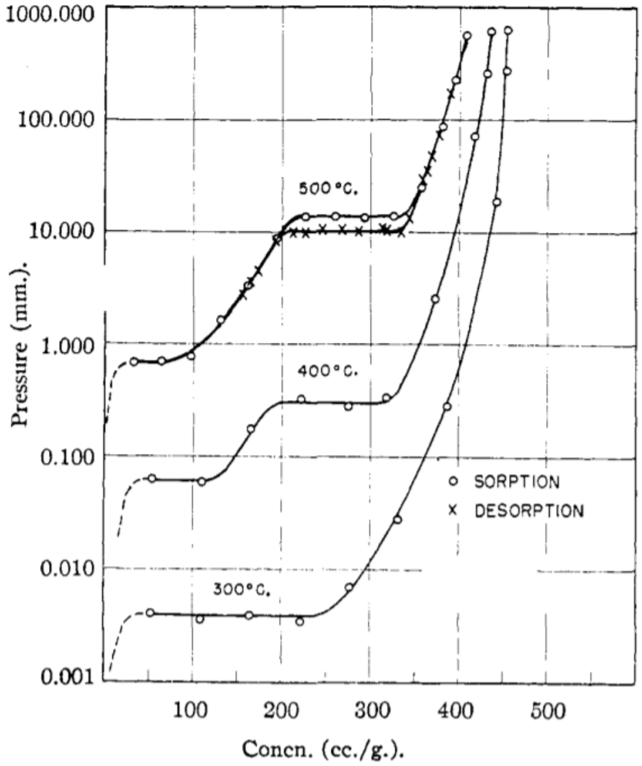

Figure 1.12 PCI curves with different temperatures measured by Haag *et al.*[60]

References

1. INDC - Submissions. https://www4.unfccc.int/sites/submissions/indc/Submission Pages/submissions.aspx.
2. Web page. https://www.nedo.go.jp/content/100080355.pdf.
3. Isothermal Properties for Hydrogen. https://webbook.nist.gov/cgi/fluid.cgi?T=25&PLow=0&PHigh=1000&PInc=1&Applet=on&Digits=5&ID=C1333740&Action=Load&Type=IsoTherm&TUnit=C&PUnit=atm&DUnit=mol%2Fl&HUnit=kJ%2Fmol&WUnit=m%2Fs&VisUnit=uPa*s&STUnit=N%2Fm&RefState=DEF.
4. Web page. https://www.gs-yuasa.com/jp/technic/vol10/pdf/010_01_001.pdf.
5. Kawasaki Hydrogen Road: Paving the way for a hydrogen-based society. http://global.kawasaki.com/en/stories/hydrogen/.
6. Demircan, A., Demiralp, M., Kaplan, Y., Mat, M. D. & Veziroglu, T. N. Experimental and theoretical analysis of hydrogen absorption in $LaNi_5$–H_2 reactors. *Int. J. Hydrogen Energy* **30**, 1437–1446 (2005).
7. Endo, N., Suzuki, S., Goshome, K. & Maeda, T. Operation of a bench-scale TiFe-based alloy tank under mild conditions for low-cost stationary hydrogen storage. *Int. J. Hydrogen Energy* **42**, 5246–5251 (2017).
8. Takeichi, N. *et al.* “Hybrid hydrogen storage vessel”, a novel high-pressure hydrogen storage vessel combined with hydrogen storage material. *Int. J. Hydrogen Energy* **28**, 1121–1129 (2003).
9. Fang, S. *et al.* The application of mathematical models to the calculation of selected hydrogen storage properties (formation enthalpy and hysteresis) of AB2-type alloys. *Int. J. Hydrogen Energy* **25**, 143–149 (2000).
10. Tamura, T., Kazumi, T., Kamegawa, A., Takamura, H. & Okada, M. Protium absorption properties and protide formations of Ti–Cr–V alloys. *J. Alloys Compd.* **356–357**, 505–509 (2003).
11. Hubbard, W. N., Rawlins, P. L., Connick, P. A., Stedwell, R. E. & O’Hare, P. A. G. The standard enthalpy of formation of $LaNi_5$ The enthalpies of hydriding of $LaNi_{5-x}Al_x$. *J. Chem. Thermodyn.* **15**, 785–798 (1983).
12. Web page. https://www.energy.gov/sites/prod/files/2017/04/f34/67464.pdf.

13. Gil, A. *et al.* State of the art on high temperature thermal energy storage for power generation. Part 1-Concepts, materials and modellization. *Renewable and Sustainable Energy Reviews* vol. 14 31–55 (2010).
14. Pardo, P. *et al.* A review on high temperature thermochemical heat energy storage. *Renew. Sustain. Energy Rev.* **32**, 591–610 (2014).
15. Felderhoff, M. & Bogdanović, B. High Temperature Metal Hydrides as Heat Storage Materials for Solar and Related Applications. *Int. J. Mol. Sci.* **10**, 325–344 (2009).
16. Wab page. https://webstore.iea.org/download/direct/422.
17. Web page. https://www.nedo.go.jp/content/100544820.pdf.
18. Web page. https://www.meti.go.jp/english/press/2019/0312_002.html.
19. Web page. http://www.cev-pc.or.jp/suiso_station/.
20. Tsurui, N. *et al.* Hydrogen Desorption Isobar Properties of $Ti_{1.1}CrMn$ at High Temperatures and Pressures. *Mater. Trans.* **59**, 855–857 (2018).
21. Selvaraj, S. *et al.* Study of cyclic performance of V-Ti-Cr alloys employed for hydrogen compressor. *Int. J. Hydrogen Energy* **43**, 2881–2889 (2018).
22. Goshome, K., Endo, N. & Tetsuhiko, M. Evaluation of a BCC alloy as metal hydride compressor via 100 MPa-class high-pressure hydrogen apparatus. *Int. J. Hydrogen Energy* **44**, 10800–10807 (2019).
23. Solovey, V. V, Ivanovsky, A. I., Kolosov, V. I. & Shmal'ko, Y. F. Series of metal hydride high pressure hydrogen compressors. *J. Alloys Compd.* **231**, 903–906 (1995).
24. Lototskyy, M. V, Yartys, V. A., Pollet, B. G. & Bowman, R. C. Metal hydride hydrogen compressors: A review. *Int. J. Hydrogen Energy* **39**, 5818–5851 (2014).
25. Web page. https://www.hiroshima-u.ac.jp/koho_press/press/2015/2015_144.
26. Web page. https://www.tepco.co.jp/cc/press/betu12_j/images/120620j0303.pdf.
27. JP2014115207A - Hydrogen removal facility for nuclear reactor building - Google Patents. https://patents.google.com/patent/JP2014115207A/en?q=~patent%2FWO2015016090A1.
28. JP2014020997A - Hydrogen remover and hydrogen removing method for reactor

containment vessel - Google Patents. https://patents.google.com/patent/JP2014020997A/en?oq=JP2014020997A.

29. WO2015016090A1 - Non-electric hydrogen collecting device - Google Patents. https://patents.google.com/patent/WO2015016090A1/en.
30. Wab page. https://labs.eng.hokudai.ac.jp/labo/loam/wp-content/uploads/2013/06/9b999e6c39e4f3d1cb4b469cdd18dda0.pdf.
31. NIST-MSEL Hydrogen Storage Program: Research - Introduction. https://www.ctcms.nist.gov/hydrogen_storage/research_pct.html.
32. Christmann, K. Interaction of hydrogen with solid surfaces. *Surf. Sci. Rep.* **9**, 1–163 (1988).
33. Moore, G. E. & Unterwald, F. C. Thermal Dissociation of Hydrogen. *J. Chem. Phys.* **40**, 2639–2652 (1964).
34. Zaluska, A., Zaluski, L. & Ström–Olsen, J. O. Nanocrystalline magnesium for hydrogen storage. *J. Alloys Compd.* **288**, 217–225 (1999).
35. Kimura, T., Miyaoka, H., Ichikawa, T. & Kojima, Y. Hydrogen absorption of catalyzed magnesium below room temperature. *Int. J. Hydrogen Energy* **38**, 13728–13733 (2013).
36. Wang, P., Wang, A. M., Zhang, H. F., Ding, B. Z. & Hu, Z. Q. Hydrogenation characteristics of Mg－TiO_2 (rutile) composite. *J. Alloys Compd.* **313**, 218–223 (2000).
37. Hanada, N., Ichikawa, T. & Fujii, H. Catalytic effect of nanoparticle 3d-transition metals on hydrogen storage properties in magnesium hydride MgH_2 prepared by mechanical milling. *J. Phys. Chem. B* **109**, 7188–7194 (2005).
38. Ivanov, E., Konstanchuk, I., Stepanov, A. & Boldyrev, V. Magnesium mechanical alloys for hydrogen storage. *J. Less Common Met.* **131**, 25–29 (1987).
39. Liang, G., Huot, J., Boily, S., Van Neste, A. & Schulz, R. Catalytic effect of transition metals on hydrogen sorption in nanocrystalline ball milled MgH_2-Tm (Tm=Ti, V, Mn, Fe and Ni) systems. *J. Alloys Compd.* **292**, 247–252 (1999).
40. Oelerich, W., Klassen, T. & Bormann, R. Metal oxides as catalysts for improved hydrogen sorption in nanocrystalline Mg-based materials. *J. Alloys Compd.* **315**, 237–242 (2001).

41. Song, M., Bobet, J.-L. & Darriet, B. Improvement in hydrogen sorption properties of Mg by reactive mechanical grinding with Cr_2O_3, Al_2O_3 and CeO_2. *J. Alloys Compd.* **340**, 256–262 (2002).
42. Barkhordarian, G., Klassen, T. & Bormann, R. Fast hydrogen sorption kinetics of nanocrystalline Mg using Nb_2O_5 as catalyst. *Scr. Mater.* **49**, 213–217 (2003).
43. Bhat, V. V *et al.* Catalytic activity of oxides and halides on hydrogen storage of MgH_2. *J. Power Sources* **159**, 107–110 (2006).
44. Malka, I. E., Czujko, T. & Bystrzycki, J. Catalytic effect of halide additives ball milled with magnesium hydride. *Int. J. Hydrogen Energy* **35**, 1706–1712 (2010).
45. Fan, M.-Q. *et al.* Superior hydrogen storage properties of MgH_2–10 wt.% TiC composite. *Energy* **35**, 3417–3421 (2010).
46. Ma, L.-P., Wang, P. & Cheng, H.-M. Hydrogen sorption kinetics of MgH_2 catalyzed with titanium compounds. *Int. J. Hydrogen Energy* **35**, 3046–3050 (2010).
47. Imamura, H., Takahashi, T., Galleguillos, R. & Tsuchiya, S. Hydrogen absorption in modified intermetallic compound systems. *J. Less Common Met.* **89**, 251–256 (1983).
48. Imamura, H. *et al.* High hydrogen storage capacity of nanosized magnesium synthesized by high energy ball-milling. *J. Alloys Compd.* **386**, 211–216 (2005).
49. Shang, C. X. & Guo, Z. X. Effect of carbon on hydrogen desorption and absorption of mechanically milled MgH_2. *J. Power Sources* **129**, 73–80 (2004).
50. Schlapbach, L., Seiler, A. & Stucki, F. Surface segregation in FeTi and its catalytic effect on the hydrogenation. *Mater. Res. Bull.* **13**, 697–706 (1978).
51. Schlapbach, L., Seiler, A. & Stucki, F. Surface segregation in FeTi and its catalytic effect on the hydrogenation II: AES and XPS studies. *Mater. Res. Bull.* **13**, 1031–1037 (1978).
52. Aoki, K., Aoyagi, H., Memezawa, A. & Masumoto, T. Effect of ball milling on the hydrogen absorption rate of FeTi and Mg_2Ni compounds. *Journal of Alloys and Compounds* vol. 203 L7–L9 (1994).
53. Aoyagi, H., Aoki, K. & Masumoto, T. Effect of ball milling on hydrogen absorption properties of FeTi, Mg_2Ni and $LaNi_5$. *J. Alloys Compd.* **231**, 804–809

(1995).

54. Chiang, C. H., Chin, Z. H. & Perng, T. P. Hydrogenation of TiFe by high-energy ball milling. *J. Alloys Compd.* **307**, 259–265 (2000).

55. Lee, S. M. & Perng, T. P. Correlation of substitutional solid solution with hydrogenation properties of $TiFe_{1-x}M_x$(M = Ni, Co, Al) alloys. *J. Alloys Compd.* **291**, 254–261 (1999).

56. Lee, S. M. & Perng, T. P. Effect of the second phase on the initiation of hydrogenation of $TiFe_{1-x}M_x$ (M = Cr,Mn) alloys. *Int. J. Hydrogen Energy* **19**, 259–263 (1994).

57. Jang, T. H., Han, J. I. & Jai-Young, L. Effect of substitution of titanium by zirconium in TiFe on hydrogenation properties. *J. Less-Common Met.* **119**, 237–246 (1986).

58. Mizuno, T. & Morozumi, T. Titanium concentration in $FeTi_x$ ($1 \leq x \leq 2$) alloys and its effect on hydrogen storage properties. *J. Less-Common Met.* **84**, 237–244 (1982).

59. Emami, H., Edalati, K., Matsuda, J., Akiba, E. & Horita, Z. Hydrogen storage performance of TiFe after processing by ball milling. *Acta Mater.* **88**, 190–195 (2015).

60. Haag, R. M. & Shipko, F. J. The Titanium-Hydrogen System[2]. *J. Am. Chem. Soc.* **78**, 5155–5159 (1956).

61. Wang, W. E. Thermodynamic evaluation of the titanium-hydrogen system. *J. Alloys Compd.* **238**, 6–12 (1996).

62. San-Martin, A. & Manchester, F. D. The H-Ti (Hydrogen-Titanium) system. *Bull. Alloy Phase Diagrams* **8**, 30–42 (1987).

63. Shen, C. C. & Wu, K. C. Pressure-composition isotherm curves of a Ti-H system above the eutectoid temperature. *Scr. Mater.* **113**, 150–153 (2016).

64. Kasajima, T., Nishikiori, T., Nohira, T. & Ito, Y. Thermodynamic Evaluation of Ti-H System at Medium-Range Temperatures by Molten Salt Electrochemical Technique. *J. Electrochem. Soc.* **150**, E355 (2003).

2 Purpose of this thesis

Various types of metal-hydrogen systems have been studied to establish the hydrogen energy society. However, most of research devoted in the practical applications for hydrogen storage so far while the fundamental research is imperative for understanding the interaction between the metal and hydrogen. The fundamental research on Ti-hydrogen system is not enough carried out so far, because Ti is not suitable as a hydrogen storage material due to high thermodynamic stability of hydride. On the other hand, from different point of view, Ti is a potential thermochemical heat storage material for high temperature as well as a hydrogen capture material for accidents such as hydrogen leakage. However, it is generally known that the reaction between Ti and H_2 based on the thermodynamic properties is difficult due to existence of stable oxide (TiO_2) layer on the surface, and thermal activation at several hundred °C is required to realize the reaction. In addition, the effective surface modification for hydrogen absorption by Ti is not reported. To utilize Ti as a metal-hydrogen system described in Introduction part, the detailed mechanism of hydrogen absorption by Ti and the effective surface modification should be understood.

In this thesis, the essential hydrogen absorption properties of Ti and its potential surface modification processes to control the reaction are discussed based on results of following experiments.

(1) The reaction between Ti and H_2

In principle, Ti should be active for hydrogen without catalysts, since the hydrogen absorption is exothermic reaction and H_2 can be dissociated easily by *d*-orbital electrons in Ti. However, the hydrogenation of Ti itself at the temperature less than 100 °C has not reported yet. In this work, to understand the essential hydrogen absorption properties, Ti with fresh surface is prepared and the hydrogen absorption properties are investigated.

(2) Surface modification by transition metals and oxides to make active sites

It is well known that transition metals can provide an active site to enhance the reaction with H_2. In this work, surface modification effects of typical transition metals and oxides were investigated, where the additives were chosen by referring research on Magnesium (Mg)-hydrogen system.

(3) Surface modification by organic solvents and graphite to prevent the surface oxidation

As different approach from the above, we also focused on surface modification by using organic materials. It is expected that the Ti surface is modified by reactions with organic materials to realize active and selective hydrogen absorption. In fact, several papers of research on Ti alloys ball-milled with organic solvents for surface modification were reported. In this work, the effects of organic solvents and graphite for surface modification of Ti were investigated.

3 Experiments

3.1 Sample preparation

3.1.1 Starting materials

The starting materials are listed in table 3.1. Nickel (Ni), palladium (Pd), niobium oxide (Nb_2O_5), and vanadium oxide (V_2O_5) were selected as solid additives, which are well known as hydrogen dissociation catalysts for Mg/MgH_2 systems.[1,2] As another surface modification technique, ball-milling in organic solvents (wet-milling) was also performed. The sample preparation by wet milling has been already reported in Mg/MgH_2 systems and TiFe/$TiFeH_2$ systems.[3,4] In this thesis, seven different kinds of organic solvents were investigated for the surface modification of Ti. In addition to above organic solvents, graphite was also investigated as an organic material. Graphite was considered as the effective additive for hydrogenation properties of Ti after the surface modification effects of organic solvents were investigated.

Table 3.1 Information of Starting materials

Material	Purity (%), state	Company
Titanium hydride (TiH_2)	98, 325 mesh	Sigma-Aldrich
Titanium (Ti)	99.7, 100 mesh	Sigma-Aldrich
Nickel (Ni)	≥99, powder	Sigma-Aldrich
Paradigm (Pd)	≥99.9, powder	Sigma-Aldrich
Niobium oxide (Nb_2O_5)	99.99, powder	Sigma-Aldrich
Vanadium oxide (V_2O_5)	≥99.6, powder	Sigma-Aldrich
Acetone	$H_2O \leq 0.001\%$	FUJIFILM Wako Pure Chemical Industries
Cyclohexane	$H_2O \leq 0.001\%$	FUJIFILM Wako Pure Chemical Industries
Hexane	$H_2O \leq 0.001\%$	FUJIFILM Wako Pure Chemical Industries
Tetrahydrofuran (THF)	$H_2O \leq 0.001\%$	FUJIFILM Wako Pure Chemical Industries
Xylene	$H_2O \leq 0.001\%$	FUJIFILM Wako Pure Chemical Industries
cis-1,2-Dimethylcyclohexane	98.0%	Tokyo Chemical Industry
2-Methyl-4-pentanone	$H_2O \leq 0.001\%$	FUJIFILM Wako Pure Chemical Industries
Graphite	99.9995%, 2-15 μm	Alfa Aesar

3.1.2 Ti with fresh surface

In this work, the reaction between Ti with fresh surface (Ti_{Fresh}) and H_2 was studied prior to the investigation of surface modification effects. It is well-known that the surface of Ti is usually covered by the TiO_2 surface layer. Therefore, the oxide layer should be removed in order to know the essential hydrogen absorption properties of Ti. Wang *et al.* reported that surface oxide layer on TiH_2 can be reduced during hydrogen desorption of the hydride.[5,6] According to the reports, it is expected that Ti_{Fresh} can be prepared by the dehydrogenation of TiH_2 without air contamination. TiH_2 was put into a reactor in glove box (Miwa MFG, MDB-2BL, $O_2 < 5$ppm, $H_2O < 2$ppm). After sealing the reactor, it was taken out from glove box. Further, the reactor was connected to a Sievert-type system equipped with rotary pump and turbomolecular pump (figure 3.1). The reactor was heated up to 580 °C under dynamic vacuum conditions using rotary pump and turbomolecular pump for 4 h. Here, the temperature of heat-treatment was determined by the hydrogen desorption profile, which will be explained in results and discussion part. After heating, the reactor was transferred into glove box to investigate hydrogenation properties. All the operations were carried out without exposing the sample to air to minimize influence of air contamination.

3.1.3 Ti with surface modification

Ball-milling technique

Ball-milling is a technique for mixing and pulverization of sample by adding the physical energy to the sample. It is commonly used for mechanical alloying, dispersion of catalyst, particle size reduction, and so on.[7–10] In this work, planetary ball-milling (PM) apparatus (Fritsch P7) was used for mixing Ti (or TiH_2) and additives. In the case of the PM method, the vessel and the disk are rotated simultaneously as shown in figure 3.2. Therefore, centrifugal force is applied to the sample and balls. Two types of ball-milling vessels were used for sample preparation (figure 3.3). Chromium (Cr) steel vessel of 30 cm^3 inner volume with quick connector (Swagelok) was used for the ball-milling of TiH_2 and solid additives (figure 3.3a). This vessel was sealed by O-ring (Viton®, fluorine rubber). However, this O-ring cannot be used for ball-milling with organic solvents due to possibility of corrosion by organic solvents. Therefore, another type of the vessel, which can be sealed by Copper (Cu) gasket, was used for wet-milling. (Figure 3.3b). Here, the temperature of heat-treatment was determined by the hydrogen desorption profile, which will be explained in results and discussion part.

Ti ball-milled with solid additives

Titanium hydride and solid additives (total 300 mg) were mixed with molar ratio of 100:1. The mixture and steel balls (SUJ-2, 7 mm in diameter) were put into the ball-milling vessel. After sealing the vessel, the inside gas was exchanged to 1 MPa H_2 by using the Sievert-type system (figure 3.1). Then the sample was ball-milled for 20 h at 370 rpm under 1 MPa H_2. To avoid temperature increase in the vessel, the ball-milling was stopped for 30 min after every 1 h milling. After the ball-milling, the sample was taken out from the vessel, and then it was transferred into the reactor for heat-treatment. In order to prepare the dehydrogenated TiH_2 with each solid additive, the samples were heated up to 550 °C under dynamic vacuum condition for 4 h using the gas system.

Ti ball-milled with organic solvents and graphite

Ti and graphite were mixed with 1:0.5 molar ratio. Total 300 mg of the mixture and 20 zirconium dioxide (ZrO_2) balls (8 mm in diameter) were put into the ball-milling vessel (30 cm^3 inner volume) with Cu gasket type. The sample was ball-milled for 3 h at 200 rpm under 0.1 MPa Ar. The ball-milling was stopped for 1 min after every 10 min milling. Here, the Ti ball-milled with graphite is denoted as $Ti_{Graphite}$ in this work. Titanium (300 mg) and 20 ZrO_2 balls were put into the ball-milling vessel. Approximately 20 wt.% organic solvent was added using Pasteur pipette. Here, organic solvent was partially vaporized during the operation, thus it was difficult to add 20 wt.% of organic solvent accurately. Considering this problem, about 70 mg of organic solvent was added. After that, the sample was ball-milled with the same conditions of $Ti_{Graphite}$. Here, the volatile by-products were observed in a temperature range of 200 to 300 °C during TG measurement for Ti ball-milled with acetone and 4-methyl-2-pentanone, which were not related to hydrogenation properties. Therefore, after ball-milling of Ti with each organic solvent, the samples were vacuumed at 300 °C for 2 h to remove the residual solvents and volatile by-products. The prepared Ti samples in each organic solvents are called as $Ti_{organic\ material}$ in this thesis.

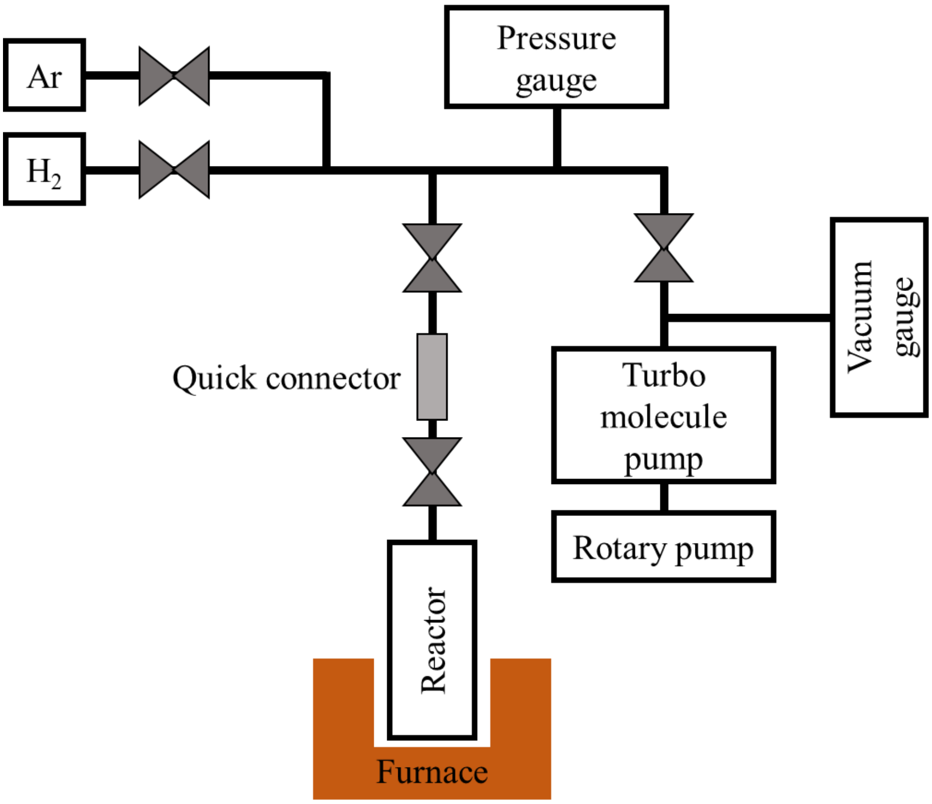

Figure 3.1 Image of the Sievert-type system used for heat-treatment.

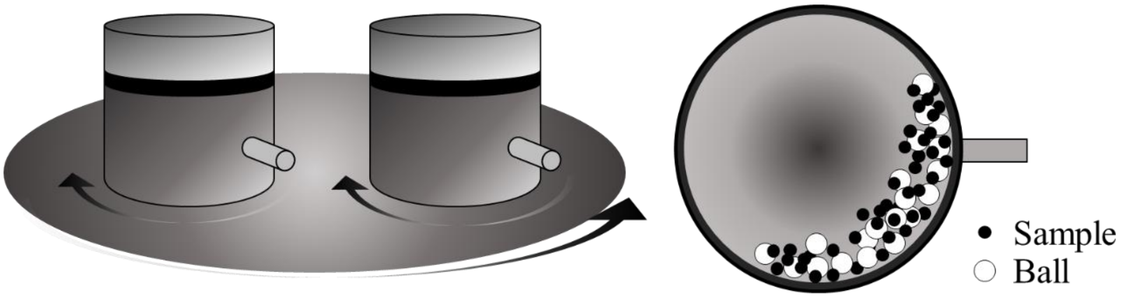

Figure 3.2 Planetary ball-milling

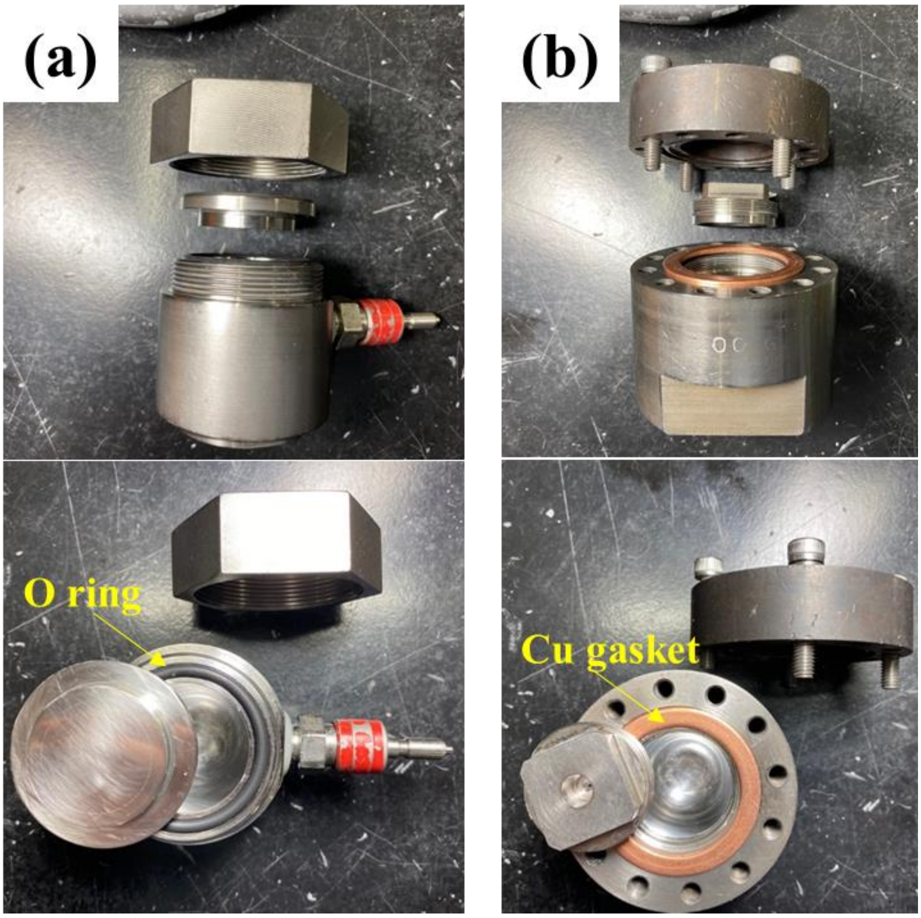

Figure 3.3 Ball-milling vessels sealed by (a) O-ring and (b) Cu gasket.

3-2 Analysis methods

3.2.1 Thermogravimetry-differential thermal analysis (TG-DTA)

Principle

Thermogravimetry (TG) is a technique for analyzing weight change of sample in heating process. A sample pan and an empty reference pan are put on the arms attached with thermocouples (figure 3.4). Both the arms are adjusted to the same height by electromagnet. The heights of both arms are monitored. If weight loss occurs during heating, the height of arm with the sample increases. Then, the current of electromagnet is decreased to adjust the height to original position. Since the change of the current is proportional to the weight loss/gain of the sample, the weight change can be calculated by the value of current. At the same time, the temperature difference between both pans is measured by the thermocouples attached to the arms. The temperature of sample pan in comparison to reference pan is increased during an exothermic reaction while it is decreased during an endothermic reaction, thus enabling to estimate the nature of reaction by this temperature difference. This technique is known as differential thermal analysis (DTA). The TG-DTA curves of a standard sample i.e. $Ca(COO)_2{\cdot}H_2O$ are shown in figure 3.5. This measurement was carried out under Ar flow up to 900 °C at 10 °C/min heating rate. The x-axis is temperature, and y-axis is weight loss (wt.%) for TG and heat flow (arb. unit) for DTA. Three peaks were observed in DTA curve with weight loss of 12.2, 31.2, and 60.8 wt.% at 169, 514, and 733 °C, respectively. These weight changes are corresponding to the reactions reported in previous literature.[11]

$$Ca(COO)_2{\cdot}H_2O \rightarrow Ca(COO)_2 + H_2O\uparrow \quad (12.3\ \text{wt.\%}) \qquad \text{(Equation 3.2)}$$

$$Ca(COO)_2 \rightarrow CaCO_3 + CO\uparrow \quad (31.5\ \text{wt.\%}) \qquad \text{(Equation 3.3)}$$

$$CaCO_3 \rightarrow CaO + CO_2\uparrow \quad (61.6\ \text{wt.\%}) \qquad \text{(Equation 3.4)}$$

In addition, it can be decided by DTA curves whether the reaction is exothermic or endothermic. In order to understand the details of reaction, TG-DTA measurement is often combined with thermal desorption mass spectrometry as described in next section.

Procedure

In this study, TG-DTA apparatus (Rigaku, TG8120) used to investigate the hydrogenation and dehydrogenation temperature of the Ti samples. The TG-DTA apparatus was located in glove box (Miwa MFG, MDB-2BL, H_2O < 0.2ppm) as shown in figure 3.6. When Ti absorbs hydrogen, the weight of sample increases according to the following reaction:

$$Ti + H_2 \rightarrow TiH_2 \text{ (4.2 wt.\%).} \qquad \text{(Equation 3.5)}$$

Therefore, the hydrogenation temperature can be measured by using TG-DTA apparatus under H_2 flow. Hydrogen absorption measurement was carried out by following processes. The Ti sample was heated from room temperature to 40 °C under Ar flow, then the carrier gas was switched to H_2 at 40 °C. After switching the carrier gas, the temperature was kept for 10 min to investigate the hydrogen absorption at around room temperature. After keeping the temperature for 10 min, the sample was heated up to 400 °C. In this work, the reactivity of each sample with H_2 was evaluated by comparing the onset temperatures of weight gain. Here, isotherm measurement is required for quantitative analysis of hydrogen absorption kinetics. However, the temperature immediately increases when Ti absorbs hydrogen due to the large hydrogenation enthalpy change.[12] Therefore, it is difficult to analyze the reaction kinetics quantitatively by this experiment. For the analysis of the hydrogen desorption properties of the TiH_2 samples, sample was heated up to 650 °C under Ar flow. Desorbed gas during heating was analyzed by thermal desorption mass spectroscopy connected with TG-DTA apparatus.

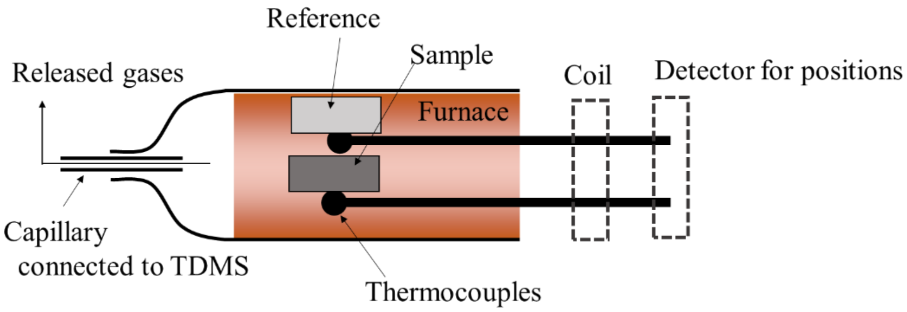

Figure 3.4 Reactor of TG-DTA apparatus

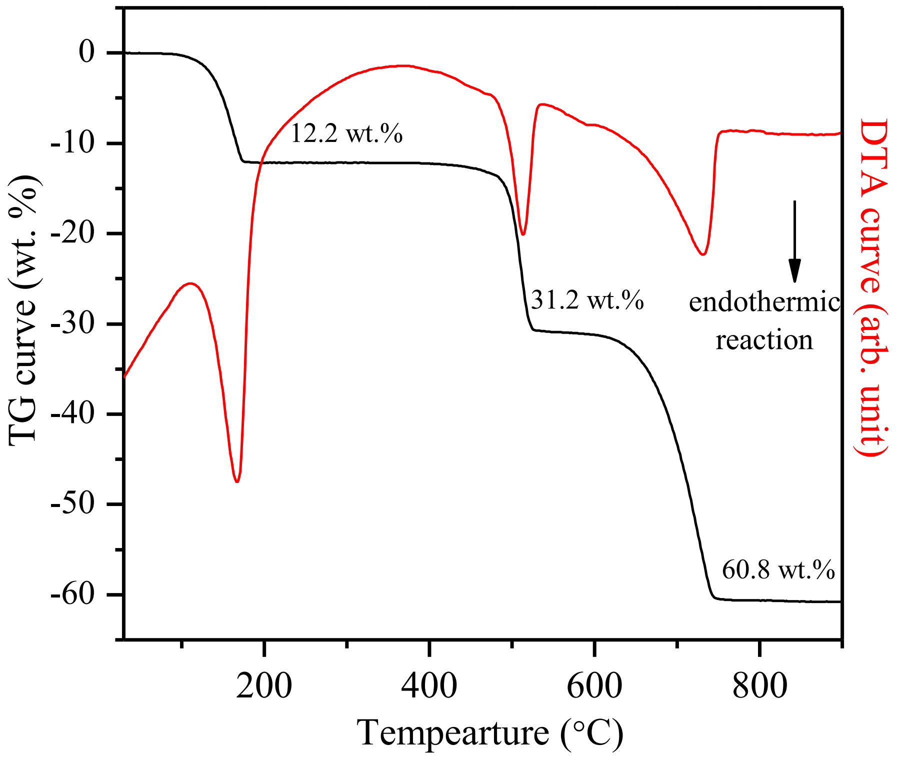

Figure 3.5 TG-DTA curves of $Ca(COO)_2{\cdot}H_2O$ performed under Ar flow at 10 °C/min.

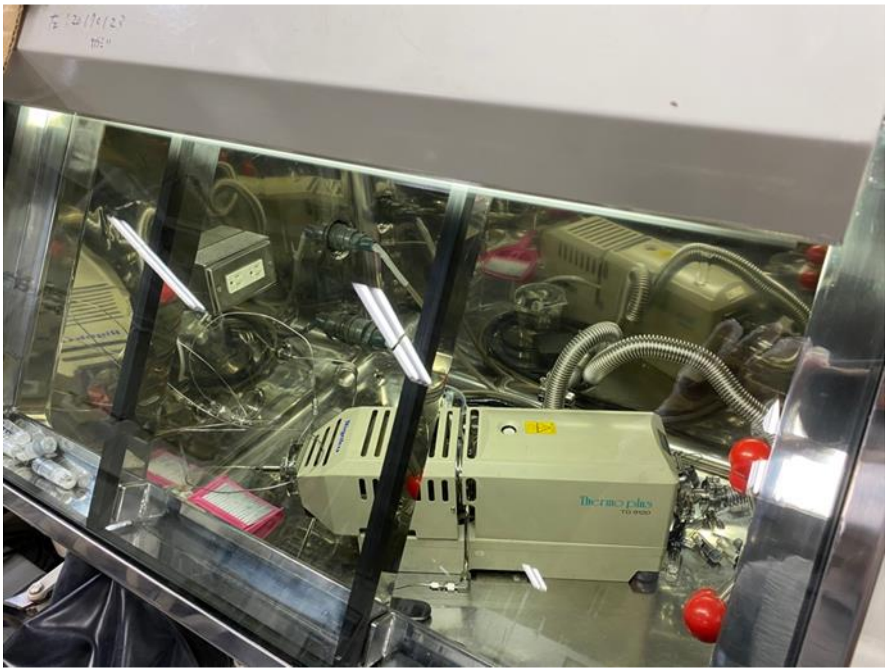

Figure 3.6 A picture of TG-DTA apparatus located in glove box.

3.2.2 Thermal desorption mass spectroscopy (TDMS)

Principle

Mass spectroscopy (MS) is a technique for the identification of molecular mass. By combining MS with TG-DTA measurements, the released gases as well as the reaction temperature and the reaction heat can be determined. The MS measurement is mainly composed of the processes in the ionization of gas, separation, and finally detection of the ionized molecules. There are several kinds of ionization methods. The most conventional method is electron impact ionization (EI method). In the case of EI method, the gases are ionized by bombarding with electrons having energy in the range of 10~70 eV.[13] Here, the gases ionized by EI method are sometimes split into fragment ions due to excess internal energy. After ionization, these gases are accelerated into magnetic field for separation. When the velocity of ion is v, the mass of ion is m, and the valence is z, the kinetic energy of ion can be given by,

$$\frac{1}{2}mv^2 = zeV, \qquad \text{(Equation 3.6)}$$

where, V is the acceleration voltage and e is the elementary electrical charge. The ionized gases are deflected by the magnetic field (B), and follow a circular motion due to the Lorentz force ($B\ zev$) imposed perpendicularly to the traveling direction as shown in figure 3.7. If the radius of the circle is r, the ionized gases feel a centrifugal force equals to mv^2/r, which is balanced with the Lorentz force,

$$mv^2/r = B\,zev. \qquad \text{(Equation 3.7)}$$

From the equation 3.6 and 3.7, following equation is derived.

$$m/z = er^2B^2/2\ V. \qquad \text{(Equation 3.8)}$$

Therefore, the molecules with m/z can be separated by scanning B or V. Here, the valence (z) is usually 1 or 2.

In this work, quadruple mass spectrometer was used, which has advantages of the fast scanning and compactness, although the detection resolution is slightly low compared with other spectrometers.[13] The quadruple mass spectrometer is composed of two twin electrodes as shown in figure 3.8. The modulated voltage V_m is applied to the electrodes as follows,

$$V_m = U + V\cos \omega t, \qquad \text{(Equation 3.9)}$$

where, U is direct current (D.C.) voltage and $V \cos \omega t$ is high frequency voltage of alternating current (A.C.). When ionized molecules pass into the two twin electrodes, they are vibrated by the high frequency voltage. Although most of the molecules collide with the electrodes, only the ionized molecular gases with specific m/z ratio can reach the detector. If the frequency of the A.C. and U/V are constant, the molecules satisfying the following equation can reach the detector,

$$m/z = 0.14\ V/f^2 r_0{}^2, \qquad \text{(Equation 3.10)}$$

$$\text{with} \quad f = \frac{\omega}{2\pi}. \qquad \text{(Equation 3.11)}$$

Therefore, the molecules with different m/z can be separated by scanning V. Figure 3.9 represents the TDMS curves of $Ca(COO)_2 \cdot H_2O$ simultaneously performed with TG-DTA measurement. The m/z = 18, 28, 44 were detected, which are corresponding to H_2O, CO, and CO_2, respectively. The desorbed gases are consistent to the reactions equation 3.2-3.4. Thus, the thermal properties of sample and desorbed gases can be investigated by TG-DTA-TDMS.

Procedure

The thermal desorption mass spectroscopy (Anelva, M-QA200TS) was used for identification of desorbed gas during TG-DTA measurements. The equipment is connected to the TG-DTA equipment by capillary as shown in figure 3.4. The spectrometer was dynamically vacuumed below 10^{-3} Pa by turbomolecular pump and rotary pump. High purity Ar gas was flowed as a carrier gas.

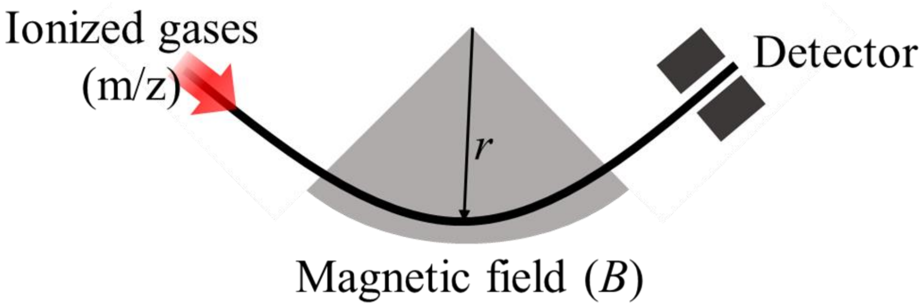

Figure 3.7 Mass spectrometer of magnetic field type

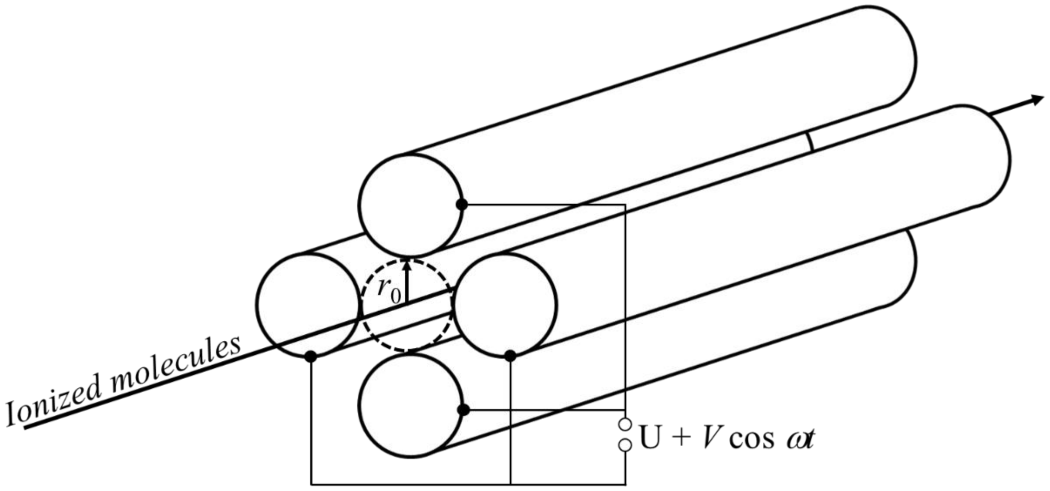

Figure 3.8 Quadruple spectrometer

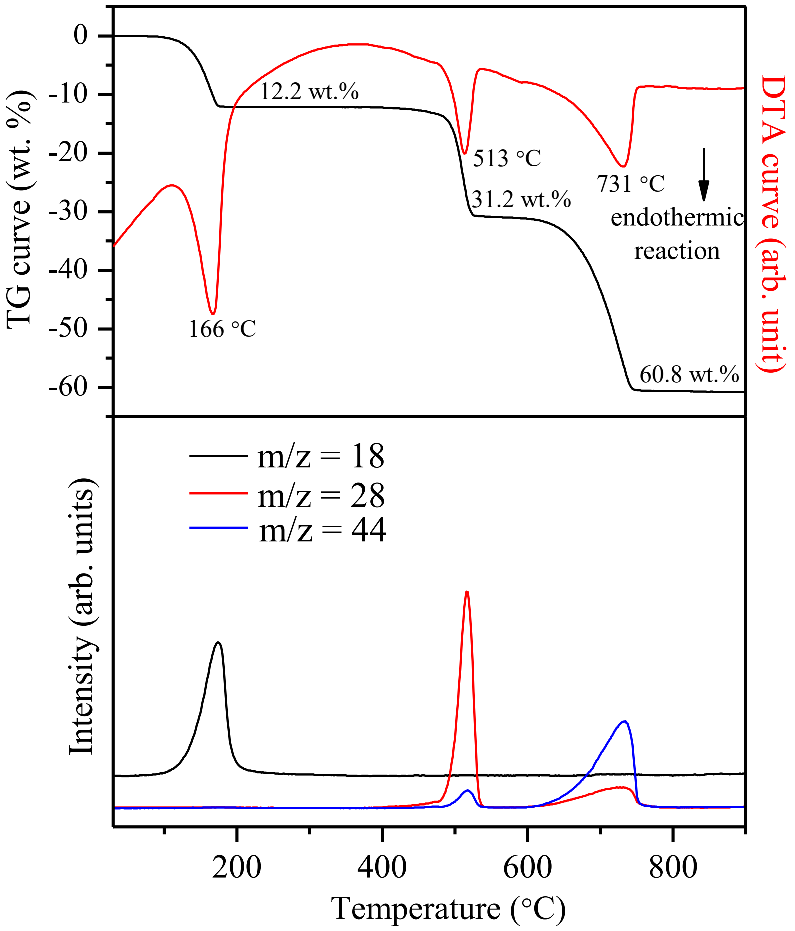

Figure 3.9 TG-DTA-MS curves of $Ca(COO)_2 \cdot H_2O$ performed under 0.1 MPa Ar flow at 10 °C/min heating rate.

3.2.3 Transmission electron microscope (TEM)

Principle

TEM is a microscope, which possesses the high resolution in the order of 0.1 nm. By combining with other spectroscopy, such as energy dispersive spectroscopy (EDS) and electron energy loss spectroscopy (EELS), TEM can be utilized to understand the distribution of elements and the chemical state as well as the morphology. TEM is composed of 3 parts namely, electron gun, electron lens, and vacuum system.

Apparatus

1) Electron gun

Thermal electron gun (TEG) and field emission gun (FEG) are used as electron source. When a filament is heated by Joule heat, electrons are released from the filament if the electrons obtain higher energy than ϕ_w (= $E_0 - E_f$). These electrons are called thermal electrons. Here, the E_0 is ground state energy, E_f is Fermi level energy, and ϕ_w is called work function. Therefore, the filament with smaller work function can effectively release thermal electrons. In high electrical field, electrons are emitted from the surface of material by passing over the Schottky barrier. The current density of electrons is given by,

$$j = aV^2 \exp(-\frac{b\phi_w^{3/2}}{V}), \qquad \text{(Equation 3.12)}$$

where, V is voltage applied between filament and anode, and a and b are constant decided by material and shape of filament, respectively.

2) Electron lens

The cross section of a magnetic field type electron lens are shown in figure 3.10. Copper wire is coiled in area 1. Magnetic field are generated in the center of the lens by the coil. When electron beam is entered into the magnetic fields, the electron beam is rotated and refracted by the force corresponding to Fleming's left-hand rule. After passing through in the magnetic field the electrons are collected at the focal point. This behavior is the same as optical convex lens. Therefore, when the distance between specimen and lens is a, between lens and image is b, and the focal length is f, the relationship of these parameters can be expressed as,

$$\frac{1}{a}+\frac{1}{b}=\frac{1}{f}. \qquad \text{(Equation 3.13)}$$

In addition, the magnification (M) can be given by,

$$M=\frac{b}{a}\approx\frac{b}{f}=\frac{a}{a-f}. \qquad \text{(Equation 3.14)}$$

Therefore, the magnification can be enhanced by reducing the focal length (f), and bringing specimen closer to focal point ($a \approx f$). There are problems about the aberration like the optical lens. The electron beam incident in the outside of lens is more strongly refracted, resulting shifting of focal point (figure 3.11), which is called spherical aberration. The spherical aberration can be reduced by increasing the accelerating voltage. Recently, TEM with spherical aberration correction has been developing. In addition, if the incident electrons have the different kinetic energy, the chromatic aberration occurs because the refractive indexes of these electrons are different. Therefore, it is required to use the electron beam with the aligned energy.

3) Vacuum system

TEM must be working under vacuum condition to increase the mean free path of the electrons. In addition to above purpose, the vacuum system has the advantages for stabilizing the high applied voltage, prolonging the life of filament, and so on. Ion pump and turbomolecular pump are usually used for evacuation in TEM equipment.[14]

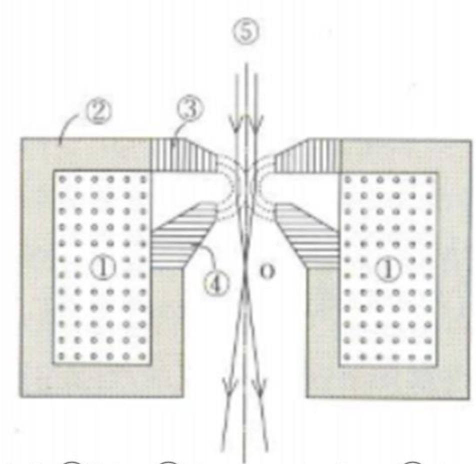

①Coil ②Yoke ③Upper polepiece ④ Lower polepiece ⑤ electron beam and O represents focal point

Figure 3.10 Cross section of a magnetic field type electron lens

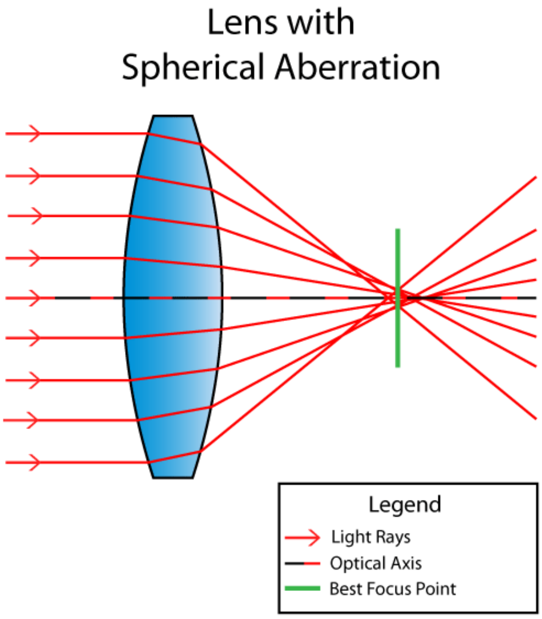

Figure 3.11 Shift of the focal point by spherical aberration cited from reference [15].[15]

Procedure

The morphology and the local chemical state of $Ti_{Graphite}$ and $Ti_{Acetone}$ were analyzed by using scanning transmission electron microscope (STEM, FEI Titan^3 G2 60-300) with an acceleration voltage of 200 kV. The sample was dispersed on a quantifoil Mo TEM grid (EM Japan Co. Ltd., R2/1 type, 200 mesh). The sample was transferred from glove box to TEM using the atmos defend holder (Mel-build corporation) without exposing to air.

3.2.4 Powder X-ray diffraction (XRD)

Principle

Powder X-ray diffraction technique is used for identification of crystal structure. If X-ray irradiates an atom, electrons of the atom are vibrated by alternating electric field of the X-rays. When the electrons are vibrating, electromagnetic wave with the same frequency as that of the vibration is released from the vibrated electron, then the electromagnetic wave expands to sphere direction from the atom. This phenomenon is called Thomson scattering. Electromagnetic wave emitted by Thomson scattering has the same wavelength as one of the incident X-ray. Since atoms have more than 1 electron, all the scattered electromagnetic waves are released associating with each wave. Therefore, the ability of X-ray scattering is higher with larger number of electrons in atom (larger atomic number). Figure 3.12 shows atomic scattering factors, which means the X-ray scattering ability of atoms. This figure indicates that the value is lower with decreasing atomic number or with increasing $\sin\theta/\lambda$. Here, θ is angle of scattered X-ray and λ is the wavelength of X-ray. Therefore, the scattering ability depends on the detection angle as well as the atomic number. Basically, this fact causes that the intensity of diffracted X-ray is lower in higher angle. In addition, the atoms with low atomic number like hydrogen do not affect the XRD profile, indicating it is impossible to determine the position of hydrogen by XRD profile.

The scattered X-rays are detected as peak when the X-ray satisfies Bragg's law. Figure 3.13 shows the schematic of X-ray diffraction from lattice plane. Where, n is number of lattice plane from upper plane, λ is wavelength of incident X-ray, d is distance between lattice planes, and θ is the angle between plane and diffracted X-ray. When the two parallel X-rays of the same wavelength incident to point D on the upper plane and point

B of the next plane, the X-rays are scattered like figure 3.13. In this case, an optical distance of X-rays for $n = 2$ against $n = 1$ is AB+BC. This length can be written by $2d\cdot\sin\theta$. If $2d\cdot\sin\theta$ is an integer multiple of wavelengths (λ), the X-rays are in phase with each other, and then the X-rays intensify. Therefore, the Bragg's law can be written as follows,

$$n\lambda = 2d\cdot\sin\theta \quad (n = 1,\ 2,\ 3\cdots). \qquad \text{(Equation 3.15)}$$

Because the angle and intensity of X-ray diffraction depend on the crystal structure and the atomic number of atoms, the crystal information can be identified by analysis of XRD pattern. Therefore, the crystal structure can be identified by analysis of X-ray diffraction pattern.

Apparatus

1) X-ray sources

A schematic of X-ray tube are shown in figure 3.14. The inside of tube has to be evacuated. When the current was supplied in a filament, the temperature of filament is increased due to Joule heat. At the same time, if voltage is supplied between the filament (cathode) and target (anode), thermal electrons are released from the filament to the target. The electrons are accelerated by the applied voltage and collide with the target. If the bombarded electron has higher energy than the binding energy of the electrons in inner shell of atom in the target, the electron is released from inner shell of atom, leading to a vacancy generation. Another electron at higher energy levels drops into the vacancy with emitting the excess energy as an X-ray. The energy of the difference between L shell and K shell is emitted as the characteristic X-ray. The processes of the characteristic X-ray emission are shown in figure 3.15. Since the energy difference between L shell and K shell is fixed by each element, the wavelengths of characteristic X-rays depend on the targets as shown in table 3.2. In addition to the characteristic X-rays, the continuous X-ray is also emitted due to bremsstrahlung interaction between the irradiated electrons and atoms. Finally, the emitted X-ray makes a spectrum like figure 3.16. The intensity of X-ray released from the target is proportional to the acceleration voltage (V), atomic number of the target (Z), and the current in the filament (i) as follows,

$$I \propto V^2 Z i. \qquad \text{(Equation 3.16)}$$

According to equation 3.16, V and i can be controlled whereas Z is fixed for a given target.

2) Detector

Scintillation counter is conventionally used for the detection of X-ray. Fluorescent substance, such as anthracene and Tl-doped NaI, is used as scintillator. When the scintillator is excited by X-ray, it emits violet light. Then, the violet light collides with photocathode, and photon is emitted. The photon is amplified by photomultiplier tube, and finally converted into electric signals. As the other options, there are proportional counter and p-type semiconductor detector. These counters detect X-rays by the similar mechanism. When X-ray passes through the counter, electrons and cations (or holes) are generated. The electrons are collected to anode, and the cations are collected to cathode, resulting in the supply of current in the electric circuit. Then the number of photons for X-ray is estimated directly by the current. The accepter of the proportional counter is gaseous, while that of the semiconductor detector is solid. The density of substance of the semiconductor type is much higher than one of the proportional counters, indicating X-ray is effectively changed into electric signal by semiconductor. The time resolution and the energy resolution are important factors for X-ray detector. The time resolution is the time required for the transformation from 1 photon to signal. The energy resolution is the minimum distinguishable energy difference. These resolutions of the detectors are shown in table 3.3. The semiconductor detector is better than scintillation type detector. Since the time resolution of the scintillation counter is less, the ratio of intensities with each peak is sometimes different from database due to miscounting. The miscounting occurs at more than 30000 ~ 50000 counts per second.[16] Therefore, if X-ray with the high intensity is used as X-ray source, this problem should be carefully taken in to account.

Procedure

In this work, XRD equipment (Rigaku RINT 2500V) was used for phase identification. Cu target was used as X-ray source (Cu-Kα: $\lambda = 1.54$ Å). The current load of filament and accelerating voltage of thermal electrons were 200 mA and 40 kV, respectively. Silicon semiconductor (Rigaku D/teX Ultra) was used as detector. For XRD measurement, a sample was spread on hand made XRD measurement glass plate. The sample was fixed by grease (Apiezon® H grease, Leef Energy Co. Ltd.). To minimize influence of oxidation due to air during measurement, sample was sealed by using polyimide sheet (Kapton®, Du Pont-Toray Co. Ltd.). The XRD sample plate is shown in figure 3.17. The XRD patterns were analyzed by comparing to databases [ICDD, JICST, COD2019] using the PDXL software.

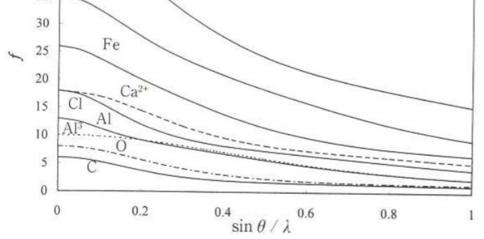

Figure 3.12 Atomic scattering factors cited from [16].[16]

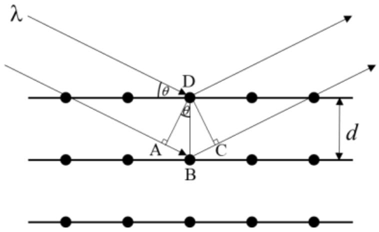

Figure 3.13 X-ray diffraction by crystalline plane

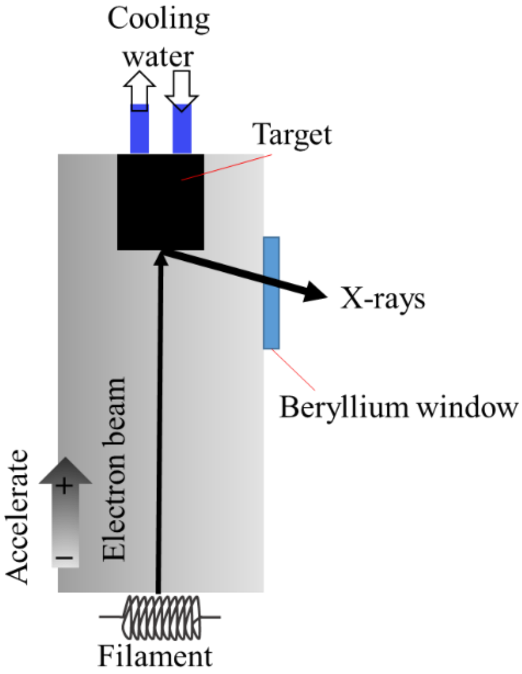

Figure 3.14 X-ray tube

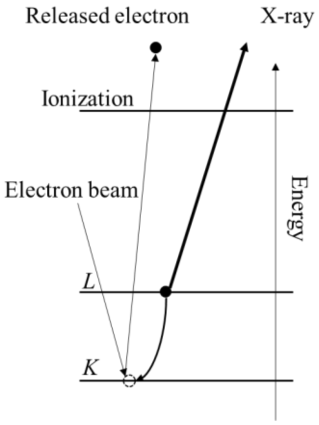

Figure 3.15 Processes of the characteristic X-ray emission

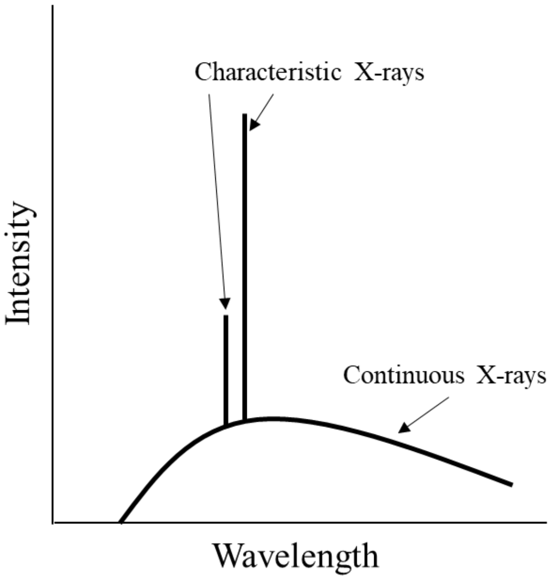

Figure 3.16 The characteristic X-ray and the continuous.

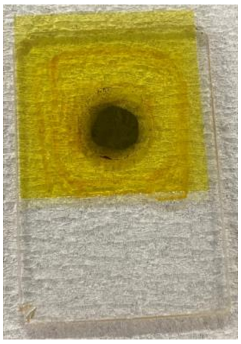

Figure 3.17 Plate for XRD measurement

Table 3.2 Targets for X-ray source and the wavelength of the characteristic X-ray

Target	$K\alpha_1$ (Å)
Ag	0.55941
Mo	0.70930
Cu	1.54056
Ni	1.65791
Co	1.78897
Fe	1.93604
Cr	2.28970

Table 3.3 The resolution of X-ray detectors reported by Shimazu *et al*.[17]

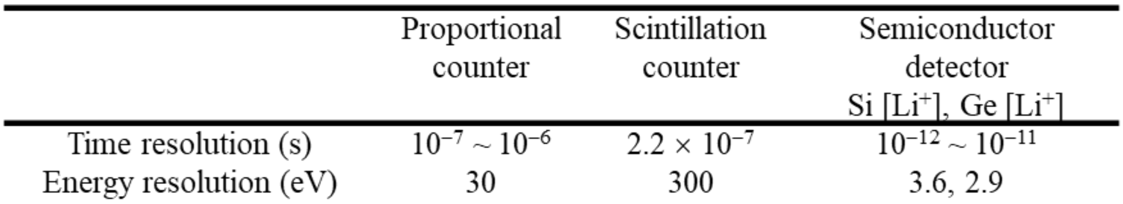

	Proportional counter	Scintillation counter	Semiconductor detector Si [Li^+], Ge [Li^+]
Time resolution (s)	$10^{-7} \sim 10^{-6}$	2.2×10^{-7}	$10^{-12} \sim 10^{-11}$
Energy resolution (eV)	30	300	3.6, 2.9

3.2.5 X-ray photoelectron spectroscopy (XPS)

Principle

X-ray photoelectron spectroscopy (XPS) is a technique used to investigate the chemical state of elements existing at surface layer (several nm). When X-ray is irradiated on to a material surface, photoelectron is released from the material by the photoelectric effect. The energy and its distribution of photoelectrons are measured by XPS measurement. The kinetic energy (E_k) of photoelectron can be expressed by following equation,

$$E_k = h\nu - E_b - \phi. \qquad \text{(Equation 3.17)}$$

Where, $h\nu$ is energy of incident X-ray, E_b is binding energy between electron and atomic nucleus, and ϕ is work function. The energy level is shown in figure 3.18. The binding energy is defined as the energy from the electron level of each orbital to Fermi level. The work function is defined as the energy difference between Fermi level and vacuum level, and it depends on several factors such as element, shape of surface, lattice plane. However, it is not necessary to calculate the work function of the sample for evaluating the binding energy. When the sample is electrically connected with the spectrometer, it can be assumed that their Fermi levels become identical as shown in figure 3.18. Therefore, if the work function of the spectrometer (ϕ_{sp}) is known, the binding energy can be estimated by the equation,

$$E_k' = h\nu - E_b - \phi_{sp}. \qquad \text{(Equation 3.18)}$$

Here, E_k' is kinetic energy evaluated by equipment. ϕ_{sp} depends on each equipment, which is decided by measuring a standard sample such as Ag film. The binding energy of electron is affected by the attractive force with nucleus and repulsive force with other electrons. Therefore, the binding energy is shifted by changing the environment of electrons. Electrons with lower binding energy, which is approximately less than 50 eV, are called valence electrons, and they are strongly affected by surrounded atoms. When a photoelectron is generated from a surface, the photoelectron moves in the surface with repeating elastic scattering and inelastic scattering. If inelastic scattering occurred before the release from the surface, the photoelectron cannot be detected as a peak. In other words, the photoelectron without inelastic scattering can be detected as photoelectron peak. Tanuma *et al*. have calculated the inelastic mean free path (IMFP) as shown in figure 3.19. The figure indicates that electron can move the average of 3 nm in the surface of elements. Thus, the XPS spectrum reflects the electronic state of surface part only.

Apparatus

1) X-ray source

The mechanism of the X-ray generation for the X-ray source is the same as that of the XRD equipment, although the energy range of X-ray is different. In the case of Cu Kα (1.54 Å) used as incident X-ray for XRD, the energy of X-ray is 8.05 keV. On the other hand, the energy of X-ray for XPS measurement is 1.49 keV (Al Kα) or 1.25 keV (Mg Kα). In the XPS measurement, the discussion of chemical shift with 0.1~1 eV is necessary to evaluate the valence state. However, the natural width of X-ray is 0.8~0.6 eV. To reduce the width of X-ray, monochromator is often used.

2) Separator

Concentric Hemispherical Analyzer (CHA) is usually used to separate electrons having different energy. Figure 3.20 shows the schematic drawing of CHA. Before the electron goes into CHA, the kinetic energy of electrons is reduced to a constant energy (pass energy) by electrostatic lens. As explain in the principle of TDMS, if the kinetic energy of electrons and the Lorentz force of separator are balanced, the electron can reach the detector. When the radii of inner and outer hemispheres are r_1 and r_2, respectively, the voltage gradient $V(r)$ can be expressed as:

$$V(r) = -V_{\mathrm{p}} \frac{r_1 r_2}{r_0^2 (r_2 - r_1)}. \qquad \text{(Equation 3.19)}$$

Here, V_{p} is the applied voltage between r_1 and r_2. r_0 is the radius of center between both hemispheres (figure 3.20). The kinetic energy E_0, which pass through on the r_0, is called pass energy. The pass energy can be expressed as,

$$E_0 = \frac{eV_{\mathrm{p}}}{(\frac{r_2}{r_1} - \frac{r_1}{r_2})}. \qquad \text{(Equation 3.20)}$$

And the energy resolution (ΔE_{A}) of CHA is

$$\Delta E_{\mathrm{A}} = \frac{wE_0}{2r_0}. \qquad \text{(Equation 3.21)}$$

Where, w is width of incident and outgoing slits. This equation suggests that the energy resolution is increased by decreasing width of slits and pass energy, and increasing r_0. On the other hand, the decrease of width of slits and pass energy leads to the lower count of electrons.

Procedure

The XPS measurements were carried out using two apparatuses of ESCA lab 250Xi (Thermo fisher), and JPS-9200 (Japan Electro Optical Laboratory Co. Ltd.) with Al-Kα (1486.6 eV) to analyze chemical states of surface. The samples were fixed on a sample holder by using carbon tape. To avoid charge up, flood gun was used during the XPS measurements. The spectra were calibrated by C1s (285.0 eV) of each sample. The samples were transferred into XPS equipment from glove box using transfer vessel.

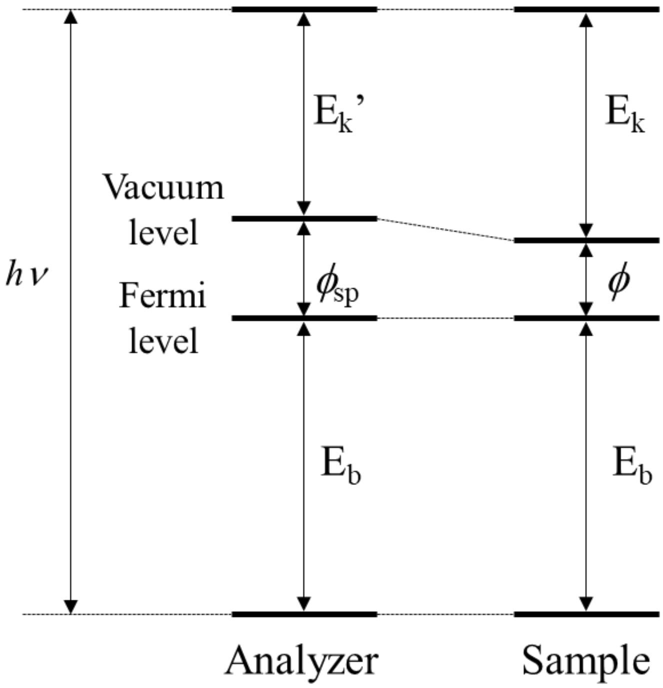

Figure 3.18 Model of energy level when analyzer and sample are electrically connected.

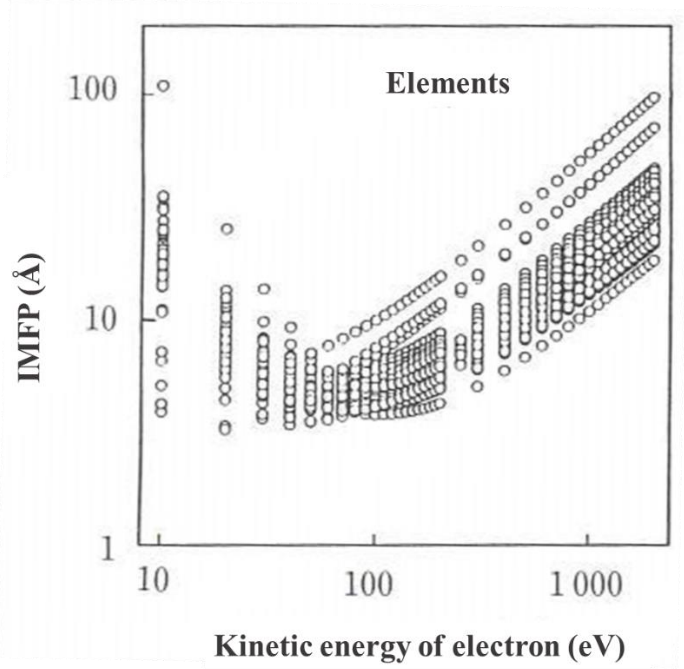

Figure 3.19 Inelastic mean free path (IMFP) of elements calculated by Tanuma *et al*.[18]

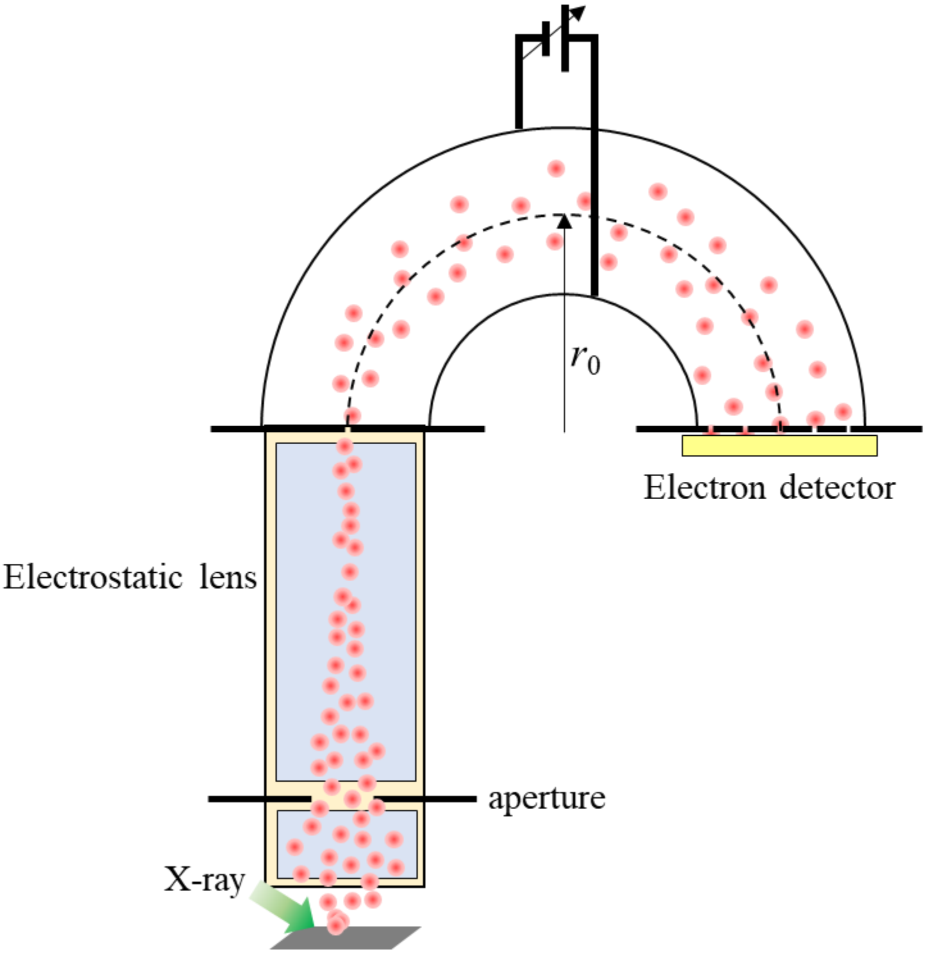

Figure 3.20 Schematic of concentric hemispherical analyzer (CHA).

3.2.6 Raman scattering spectroscopy

Principle

Raman scattering spectroscopy is a spectroscopy, which focus on the energy range between 10 and 1000 cm^{-1}. Rotational and vibrational modes of atoms have the energy in this region. Therefore, the chemical bonding states between atoms can be determined by Raman spectroscopy. In the case of diatomic molecule, the molecule can be considered as mass points connected by a spring as shown in figure 3.21. Therefore, the vibrational energy can be expressed by harmonic oscillator model as shown follows,

$$E_{\nu} = h\nu_0(\text{v} + \frac{1}{2}) \qquad (\nu = 0,\ 1,\ 2,\ \cdots). \quad \text{(Equation 3.22)}$$

Where, h is Plank constant, ν_0 is frequency of vibration at ground state, and ν is quantum number of vibrations. According to Hooke's law, the frequency of the vibration ν_0 is given by,

$$\text{v}_0 = \frac{1}{2\pi}\sqrt{\frac{k}{m'}}, \quad \text{(Equation 3.23)}$$

$$m' = \frac{m_1 m_2}{m_1 + m_2}, \quad \text{(Equation 3.24)}$$

where, k is the force constant, and m' is effective mass, and m_1 and m_2 are mass of each mass point. Here, the force constant between both points represents the strength of binding.

When electromagnetic wave irradiates atoms, the electric field interacts with the atoms. Then the atomic nucleus is vibrated by the electric field as shown in figure 3.22. Energy transformation between incident light and atom occurred during the interaction, resulting in the transformation of vibration energy levels. The induced dipole moment μ is given by,

$$\mu = \alpha E, \qquad \text{(Equation 3.25)}$$

where, α is polarizability, and E is electric field of incident light. These parameters can be expressed as,

$$E = E_0 \cos 2\pi \nu_i t, \qquad \text{(Equation 3.26)}$$

$$\alpha = \alpha_0 + \left(\frac{\partial \alpha}{\partial Q}\right)_0 Q, \qquad \text{(Equation 3.27)}$$

$$Q = Q^0 \cos 2\pi \nu_i t, \qquad \text{(Equation 3.28)}$$

here, α_0 is polarizability in equilibrium position, E_0 is amplitude of electric field, Q is displacement of atomic nucleus, and Q^0 is maximum displacement of atomic nucleus. Therefore, μ can be expressed as:

$$\mu = \alpha_0 E_0 \cos 2\pi \nu_i t + 1/2 \, (\partial \alpha / \partial Q)_0 Q^0 E_0 [\cos 2\pi(\nu_i + \nu)t + \cos 2\pi(\nu_i - \nu)t]. \qquad \text{(Equation 3.29)}$$

The first term on the right side of equation represents the same frequency of vibration as incident light. On the other hand, $(\nu_i + \nu)$ and $(\nu_i - \nu)$ appear in second term, which indicate that the frequency is increased or decreased, respectively. Therefore, the scattering lights include the electromagnetic wave with higher and lower energy compared with incident light as shown in figure 3.23, for which the energy difference is corresponding to the difference of vibration energy level. This phenomenon is called Raman scattering, and these lights are denoted as Stokes and anti-Stokes scattering, respectively. According to the equation 29, the selection rule of Raman scattering is

$$(\partial \alpha / \partial Q)_0 \neq 0. \qquad \text{(Equation 3.30)}$$

This indicates that the polarizability of molecule must be changed.

Procedure

The Raman spectroscopy was performed to analyze chemical bonding in the sample. The light source was an Ar ion laser (Spectra-physics, Inc., Stabilite 2017) operated at 488.0 nm with an output power of 4 mW. The scattered light was analyzed by a triple monochromator (JASCO, TRS-600) with a liquid-N_2 cooled charge coupled device (CCD) detector (Princeton Instruments, Inc., model LN/CCD-1100-PB). The Ti sample was pressed using pellet maker with 10mm diameter at 180 MPa for 5 min to make a pellet for Raman spectroscopy. The pellet sample was fixed on the sample stage using carbon tape. The sample stage was put into hand-made vessel, which can avoid air contamination during the measurement.

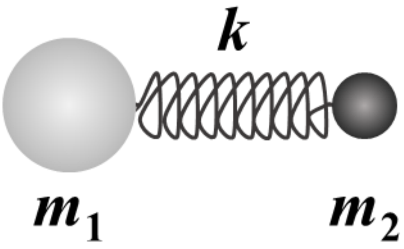

Figure 3.21 Schematic view of stretching vibration for diatomic molecule

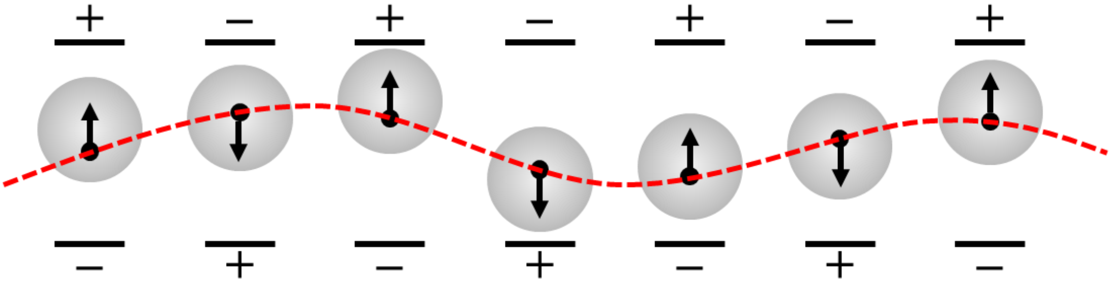

Figure 3.22 Induced dipole moment

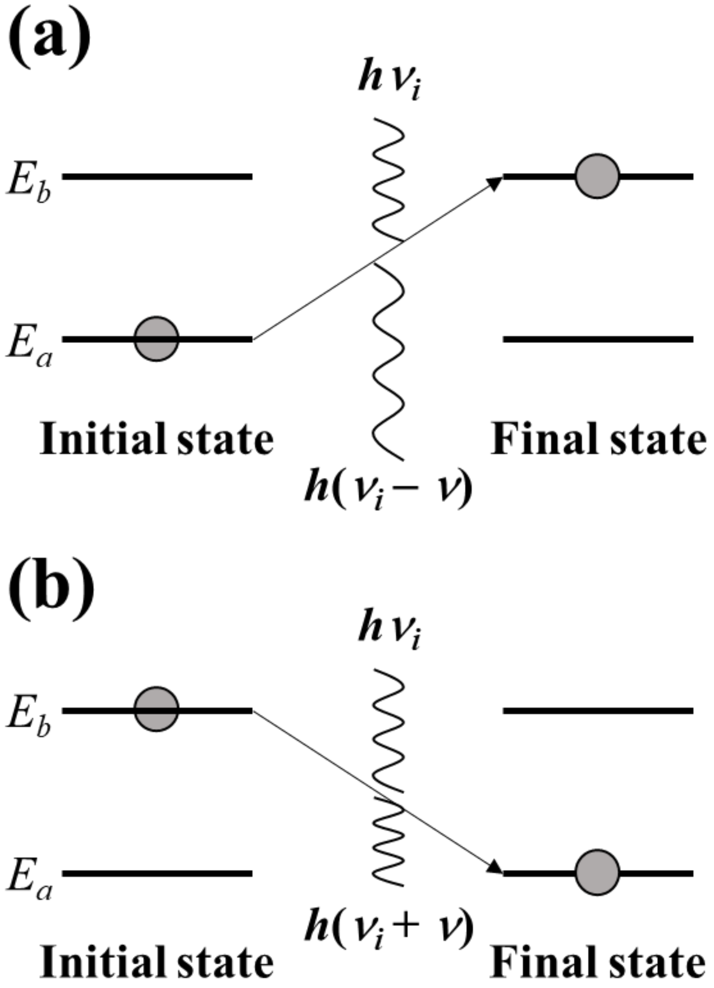

Figure 3.23 Energy diagram of Raman scattering. (a) Stokes scattering (b) anti-Stokes scattering.

References

1. Barkhordarian, G., Klassen, T. & Bormann, R. Fast hydrogen sorption kinetics of nanocrystalline Mg using Nb_2O_5 as catalyst. *Scr. Mater.* **49**, 213–217 (2003).
2. Denis, A., Sellier, E., Aymonier, C. & Bobet, J. L. Hydrogen sorption properties of magnesium particles decorated with metallic nanoparticles as catalyst. *J. Alloys Compd.* **476**, 152–159 (2009).
3. Imamura, H., Tabata, S., Shigetomi, N., Takesue, Y. & Sakata, Y. Composites for hydrogen storage by mechanical grinding of graphite carbon and magnesium. *J. Alloys Compd.* **330–332**, 579–583 (2002).
4. Emami, H., Edalati, K., Matsuda, J., Akiba, E. & Horita, Z. Hydrogen storage performance of TiFe after processing by ball milling. *Acta Mater.* **88**, 190–195 (2015).
5. Wang, C. *et al.* XPS study of the deoxidization behavior of hydrogen in TiH_2 powders. *Powder Technol.* **302**, 423–425 (2016).
6. Wang, C., Pan, L., Zhang, Y., Xiao, S. & Chen, Y. Deoxidization mechanism of hydrogen in TiH_2 dehydrogenation process. *Int. J. Hydrogen Energy* **41**, 14836–14841 (2016).
7. Koch, C. C., Cavin, O. B., McKamey, C. G. & Scarbrough, J. O. Preparation of 'amorphous' $Ni_{60}Nb_{40}$ by mechanical alloying. *Appl. Phys. Lett.* **43**, 1017–1019 (1983).
8. Hanada, N., Ichikawa, T. & Fujii, H. Catalytic effect of Ni nano-particle and Nb oxide on H-desorption properties in MgH_2 prepared by ball milling. *J. Alloys Compd.* **404–406**, 716–719 (2005).
9. Imamura, H., Kitazawa, I., Tanabe, Y. & Sakata, Y. Hydrogen storage in carbon/Mg nanocomposites synthesized by ball milling. *Int. J. Hydrogen Energy* **32**, 2408–2411 (2007).
10. Ivanov, E., Konstanchuk, I., Stepanov, A. & Boldyrev, V. Magnesium mechanical alloys for hydrogen storage. *J. Less Common Met.* **131**, 25–29 (1987).
11. Arii, T. *et al.* Thermal Analysis. *KODANSHA Co., Ltd.*
12. Wang, W. E. Thermodynamic evaluation of the titanium-hydrogen system. *J. Alloys Compd.* **238**, 6–12 (1996).

13. Toshiyuki, S. & Hisanobu, W. Introduction of equipment for analytical chemistry. *SANKYO SHUPPAN CO., Ltd.* (1998).
14. Toshiaki, O., Shigeo, H., Yuichi, I. & Kiichi, H. Transmission Electron Microscope. *Maruz. Co., Ltd.* (2002).
15. Web page. https://photographylife.com/what-is-spherical-aberration.
16. Akiba, E. *et al.* Practice of Powder X-ray analysis-Rietveld Refinement-. *Asakura Publ. Co., Ltd.*
17. Shimazu, M. & Nakazawa, H. Semiconductor Detector and Its Applications to the X-ray Diffraction Method. *J. Mineral. Soc. Japan* **11**, 411–431 (1974).
18. Sawada, T. *et al.* X-ray photoelectron spectroscopy. *Maruz. Co., Ltd.*

4 Results and discussion

4.1 The reaction between Ti and H_2

In order to determine the dehydrogenation conditions of TiH_2 to prepare Ti metal, the hydrogen desorption profile of pristine TiH_2 was obtained. TG-DTA-MS result of the pristine TiH_2 measured under 0.1 MPa Ar flow up to 650 °C at 5 °C/min is shown in figure 4.1.1. Three endothermic peaks with weight loss were observed from 400 °C to 650 °C. In the MS measurement, the intensity of $m/z = 2$ corresponding to hydrogen (H_2) increased with the weight loss, indicating that TiH_2 was decomposed in the above temperature region. Figure 4.1.2 shows the XRD results of TiH_2 before and after the TG-DTA-MS measurement. The diffraction peaks of the pristine TiH_2 before the heating were assigned to the TiH_2 phase, whereas the diffraction pattern after the TG-DTA-MS measurement was ascribed to the Ti phase. Thus, XRD results suggested the TiH_2 transformation in to Ti during the TG-DTA-MS measurement. From these results, the appropriate temperature to prepare dehydrogenated TiH_2 was determined to 580 °C, which was corresponding to the third peak temperature of the MS profile. The XRD result of the dehydrogenated TiH_2 through heat treatment is also shown in figure 4.1.2, which confirmed that Ti phase was generated by the heat treatment at 580 °C, indicating the hydrogen desorption was completed.

After the dehydrogenation treatment, the hydrogen absorption measurement of the dehydrogenated TiH_2 was carried out under 0.1 MPa H_2 flow at a temperature from 40 to 400 °C. The hydrogenation curves of the dehydrogenated TiH_2 and the pristine Ti as a reference sample are shown in figure 4.1.3. About 4 wt.% of weight gain was observed during the all TG measurements, and this value is close to the theoretical hydrogen capacity of TiH_2 (4.2 wt.%). It was confirmed by the XRD measurements that Ti is converted to TiH_2, as shown in figure 4.1.4. Therefore, the weight gain during TG measurement is corresponding to hydrogen absorption by Ti. The hydrogenation of the pristine Ti occurred at 355 °C, namely the thermal activation is required to realize the reaction. On the other hand, when the hydrogen absorption measurement of the dehydrogenated TiH_2 was conducted immediately after the dehydrogenation treatment, H_2 was absorbed even at 40 °C (just after switching carrier gas). This result suggests that the Ti should have an active surface to hydrogen just after dehydrogenation, and then there was no need of any catalysts and/or heat-activation. However, the hydrogenation temperature was increased to 125 and 225 °C after keeping the sample in the glove box for 1 and 7 days after the sample preparation. It was considered that surface oxidation of Ti proceeded by the small amount of oxygen (less than 5 ppm) and water (less than 2 ppm) included in the glovebox. In other words, the surface of Ti just after dehydrogenation had a clean surface, and it was easily inactivated under the conditions with very low O_2 and H_2O concentration because of the high reactivity. As a result, hydrogenation temperature was increased for the Ti samples kept for long time even in the glovebox. Ti 2p XPS spectra for the pristine Ti, TiH_2, and the dehydrogenated TiH_2 are shown in figure 4.1.5. For the pristine Ti, two peaks were observed at 459.0 eV and 464.8 eV, respectively. These peaks were assigned to the doublet of $Ti2p_{3/2}$ (459.0 eV) and $Ti2p_{1/2}$ (464.8 eV) of Ti^{4+} (TiO_2).[1] Considering the detectable depth of XPS measurement, the thickness of the TiO_2 layer was roughly estimated to be more than 10 nm. Thus, it was concluded that the surface of the pristine Ti was covered by the TiO_2 layer and the hydrogenation was inhibited by the surface oxide layer. The spectrum of the pristine TiH_2 is similar to the one of the pristine Ti, suggesting TiH_2 was also covered by the TiO_2 layer. On the other hand, the highest intensity peak in the Ti 2p XPS spectrum of the dehydrogenated TiH_2 was observed at 454.0 eV. This peak can be assigned to the $Ti2p_{3/2}$ peak of Ti^0 (metallic Ti).[1] This result indicated that the fresh surface of Ti was generated by the dehydrogenation of TiH_2. The peak with low intensity was also observed in the area of Ti^{3+}~Ti^{4+}. The fresh Ti surface could be partially oxidized because the metallic Ti is quite active for O_2 and H_2O as discussed above. It is reported that the reduction reaction of TiO_2 formed on the TiH_2 surface during H_2 desorption. Wang *et al.* suggested the following reaction,[2,3]

$$TiO_2 + 4H\text{ (atom)} \rightarrow Ti + 2H_2O\text{ (gas)}. \quad (4.1.1)$$

Before desorbing H_2, H atoms are recombined on the Ti surface to form H_2. Because the H atoms are unstable, the Gibbs free energy change of above reaction is negative in the temperature range of H_2 desorption, thermodynamically (figure 4.1.6). Thus, Ti with the fresh surface (Ti_{Fresh}) was obtained by the dehydrogenation of TiH_2, and it was experimentally clarified that Ti_{Fresh} can react to H_2 even at around room temperature without any catalysts and surface modification, if the TiO_2 layer could be removed from the Ti surface.

To understand the difference of surface properties between Ti and Mg, the hydrogenation properties of Mg with fresh surface were also investigated. Although it is though that the surface of Mg should be clean to absorb hydrogen[4], there is no report for the reaction between Mg with fresh surface and H_2 at room temperature. Figure 4.1.7 is the hydrogen desorption curve of the pristine MgH_2. The hydrogen desorption was observed between 400 and 450 °C. In addition, the phase change from MgH_2 to Mg was confirmed by XRD measurements (figure 4.1.8). The pristine MgH_2 was dehydrogenated using TG-DTA-MS apparatus, and then the carrier gas was changed from Ar to H_2 after cooling the TG-DTA-MS apparatus to investigate the hydrogen absorption properties. However, the hydrogen absorption did not proceed even by heating up to 250 °C as shown in figure 4.1.9. This result must be due to the difference in surface properties between Ti and Mg. Ti has *d*-electrons and it is active for H_2 without catalysts, whereas Mg does not have *d*-electrons and then a catalyst for hydrogen dissociation is required for room temperature hydrogenation.

Thus, the H_2 absorption properties of Ti_{Fresh} could be understood. Two kinds of strategies for surface modification of Ti have been considered. One is to add typical solid catalysts to make an active site for hydrogen absorption. Another is to synthesize a special surface in order to prevent oxidation and keep the active Ti surface. These methods were investigated and the results are placed in next section. Considering the results of Ti_{Fresh}, the hydrogen absorption properties were evaluated after keeping for the sample more than 1 day in the glovebox to clarify the surface modification effects.

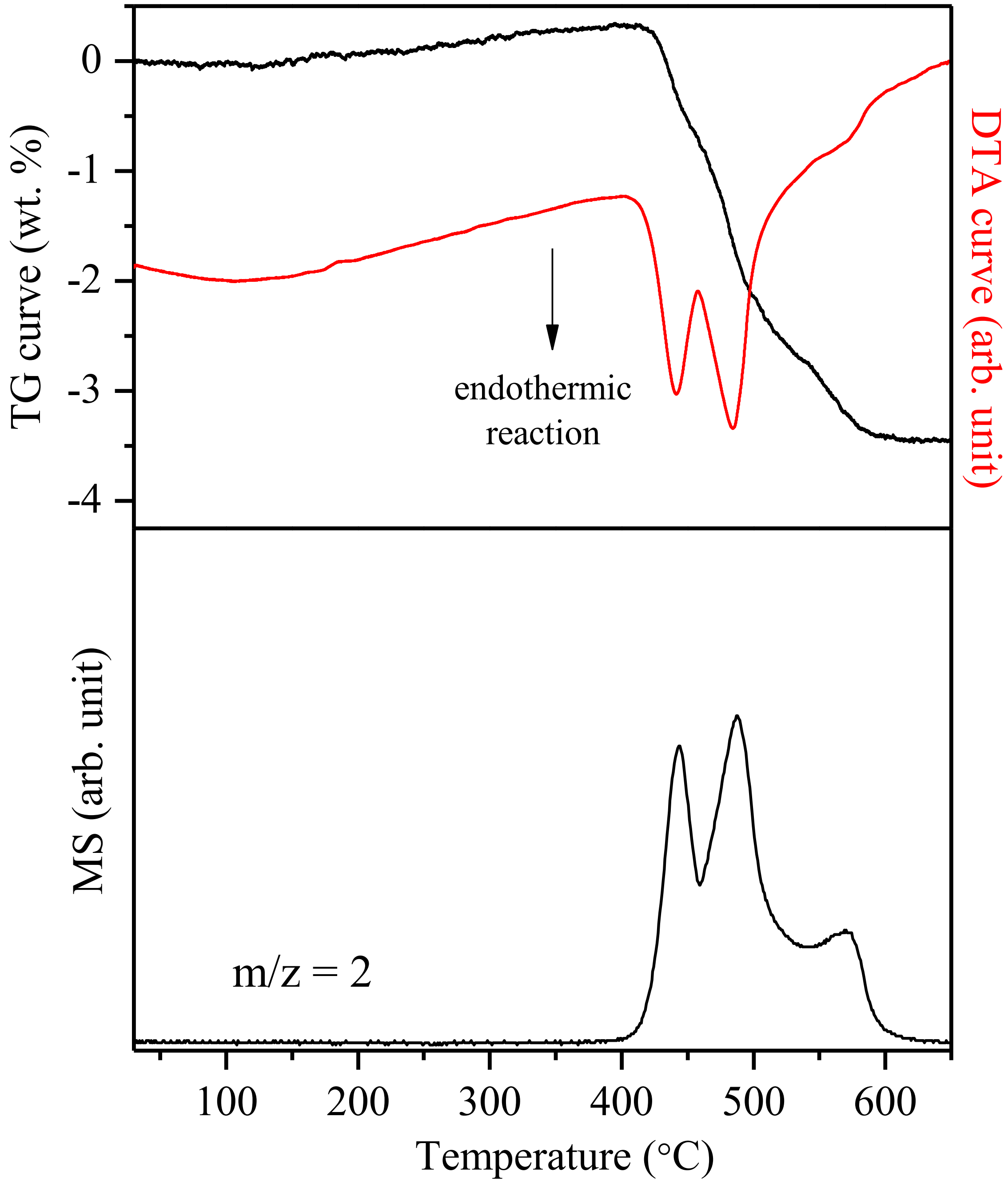

Figure 4.1.1 TG-DTA-MS result of the pristine TiH_2 measured under 0.1 MPa Ar flow up to 650 °C at 5 °C/min.

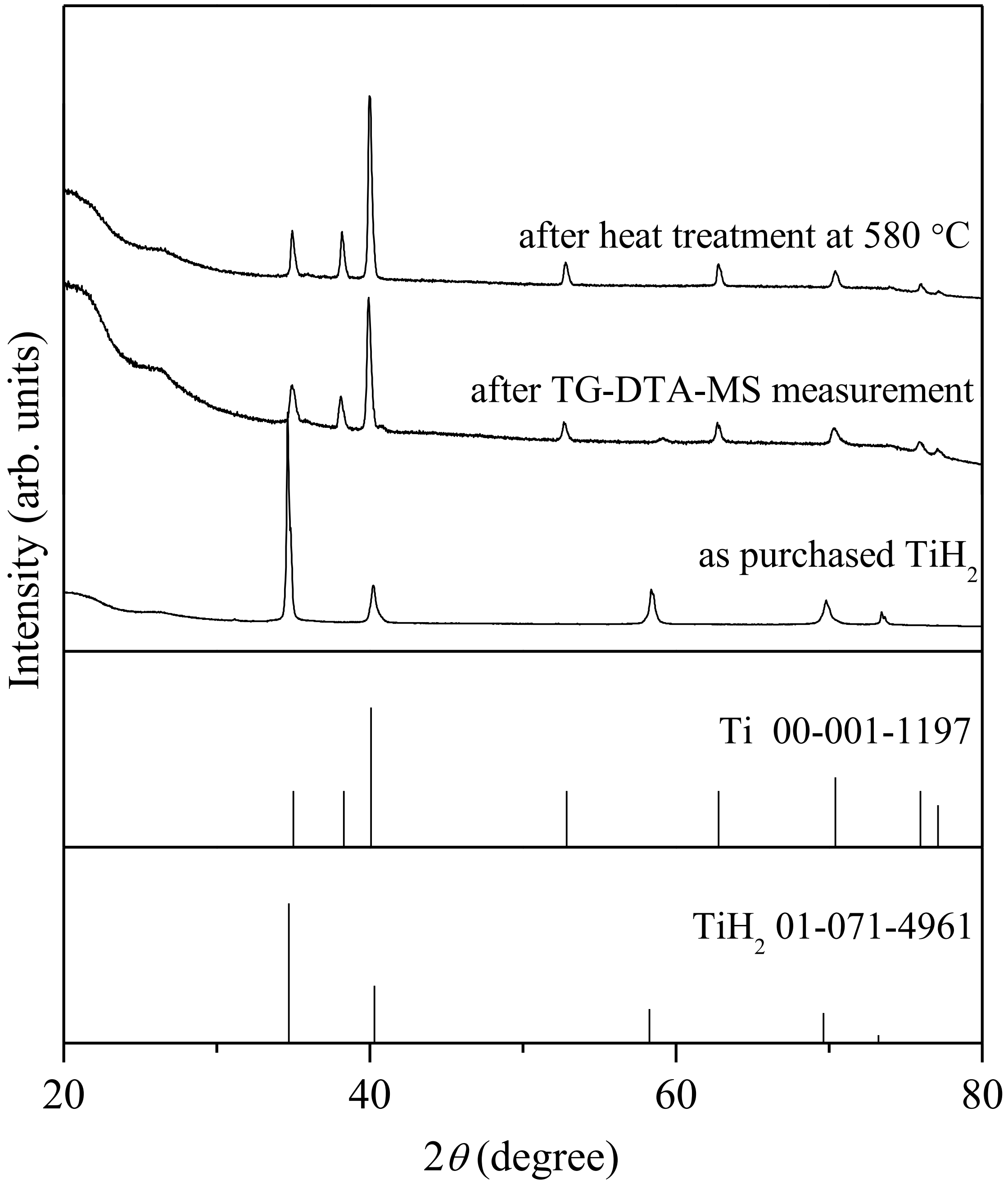

Figure 4.1.2 XRD patterns of the pristine TiH_2 before and after heating. The TG-DTA-MS measurement performed under Ar flow up to 650 °C at 5 °C/min and top figure is XRD pattern of the dehydrogenated TiH_2 at 580 °C under dynamic vacuum for 4 h.

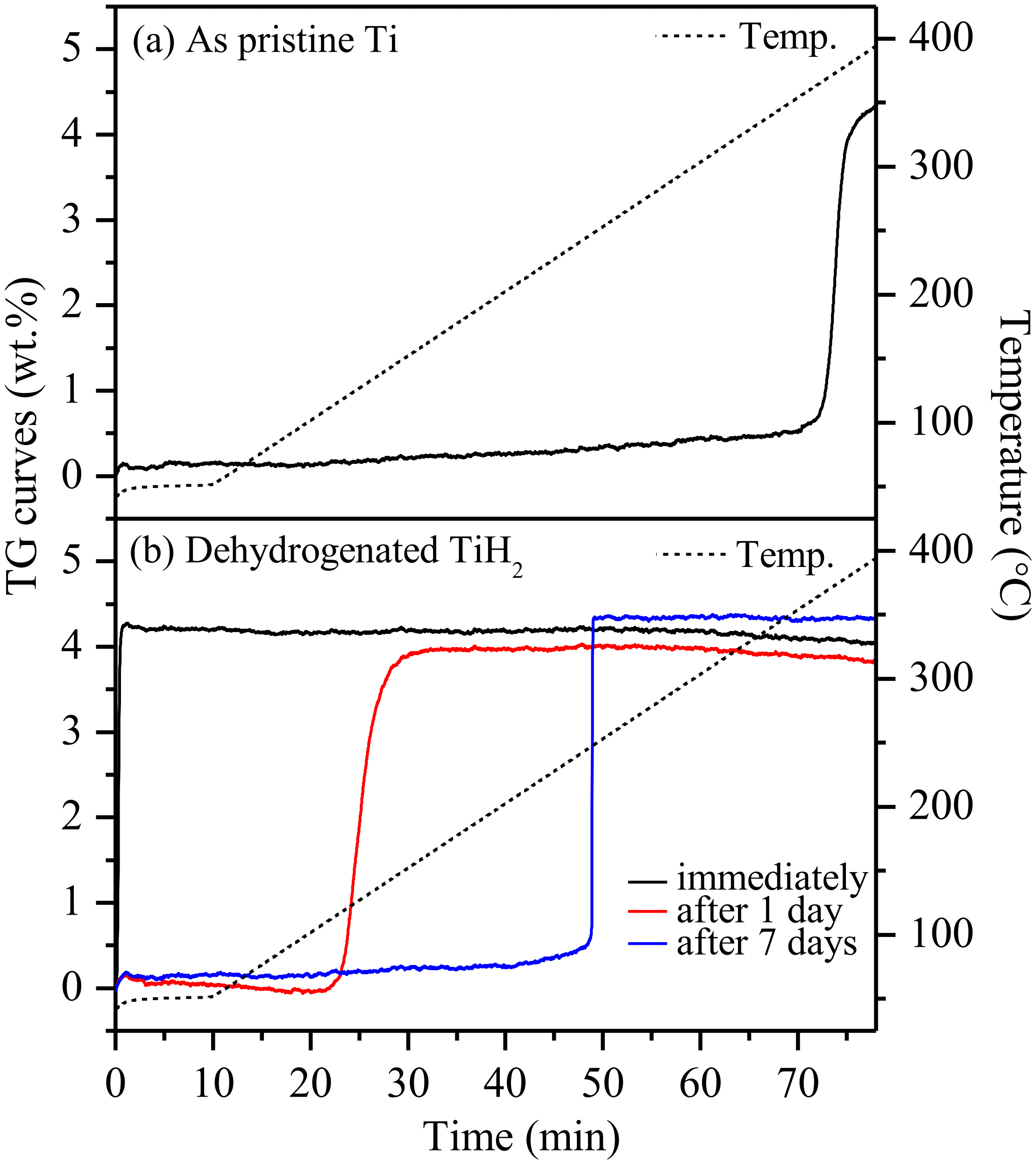

Figure 4.1.3 TG curves of (a) as pristine Ti and (b) dehydrogenated TiH_2 performed under 0.1 MPa H_2 flow.

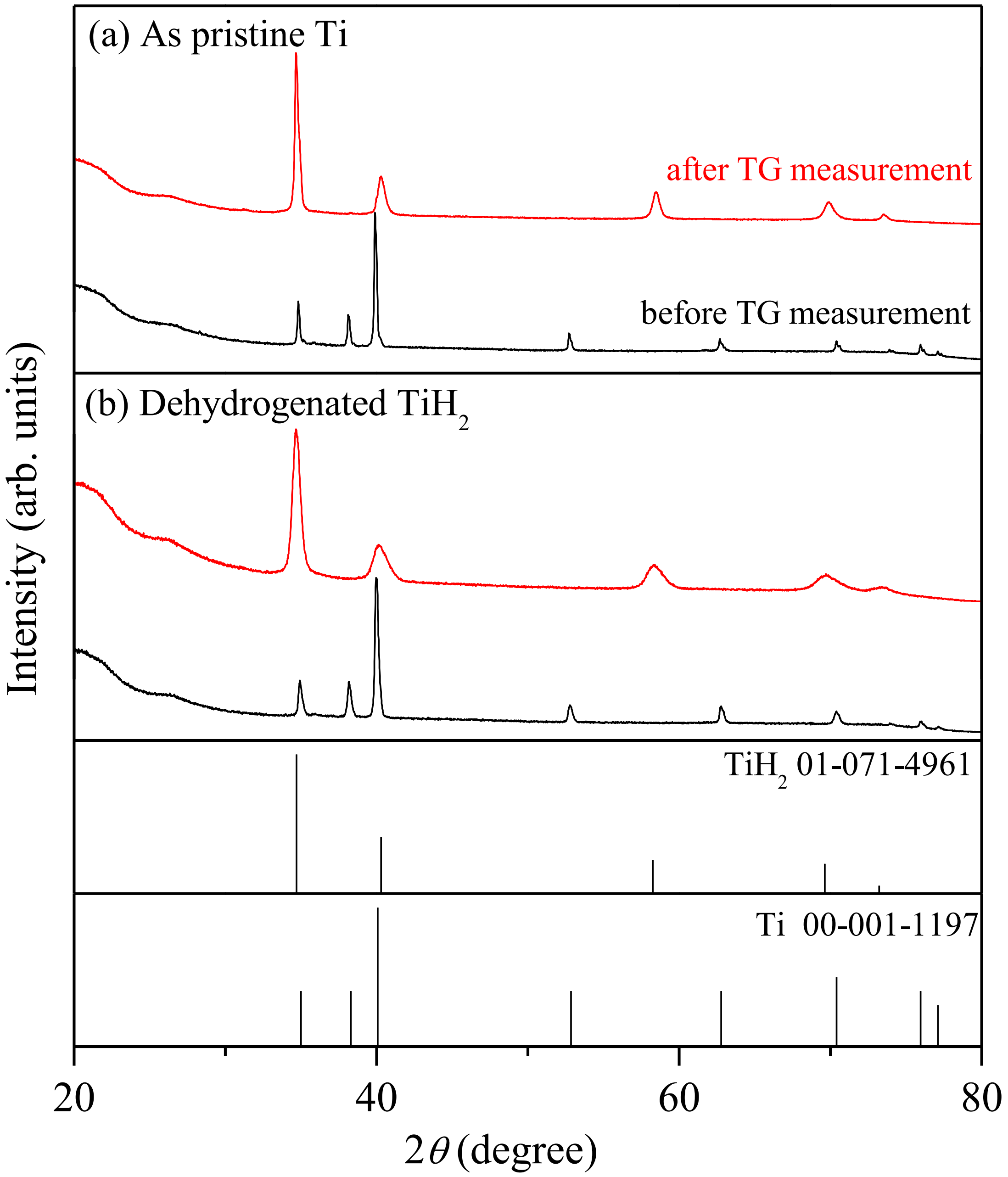

Figure 4.1.4 XRD patterns of the pristine Ti and the dehydrogenated TiH_2 before and after TG measurement. These TG measurements were carried out under 0.1 MPa H_2 flow up to 400 °C.

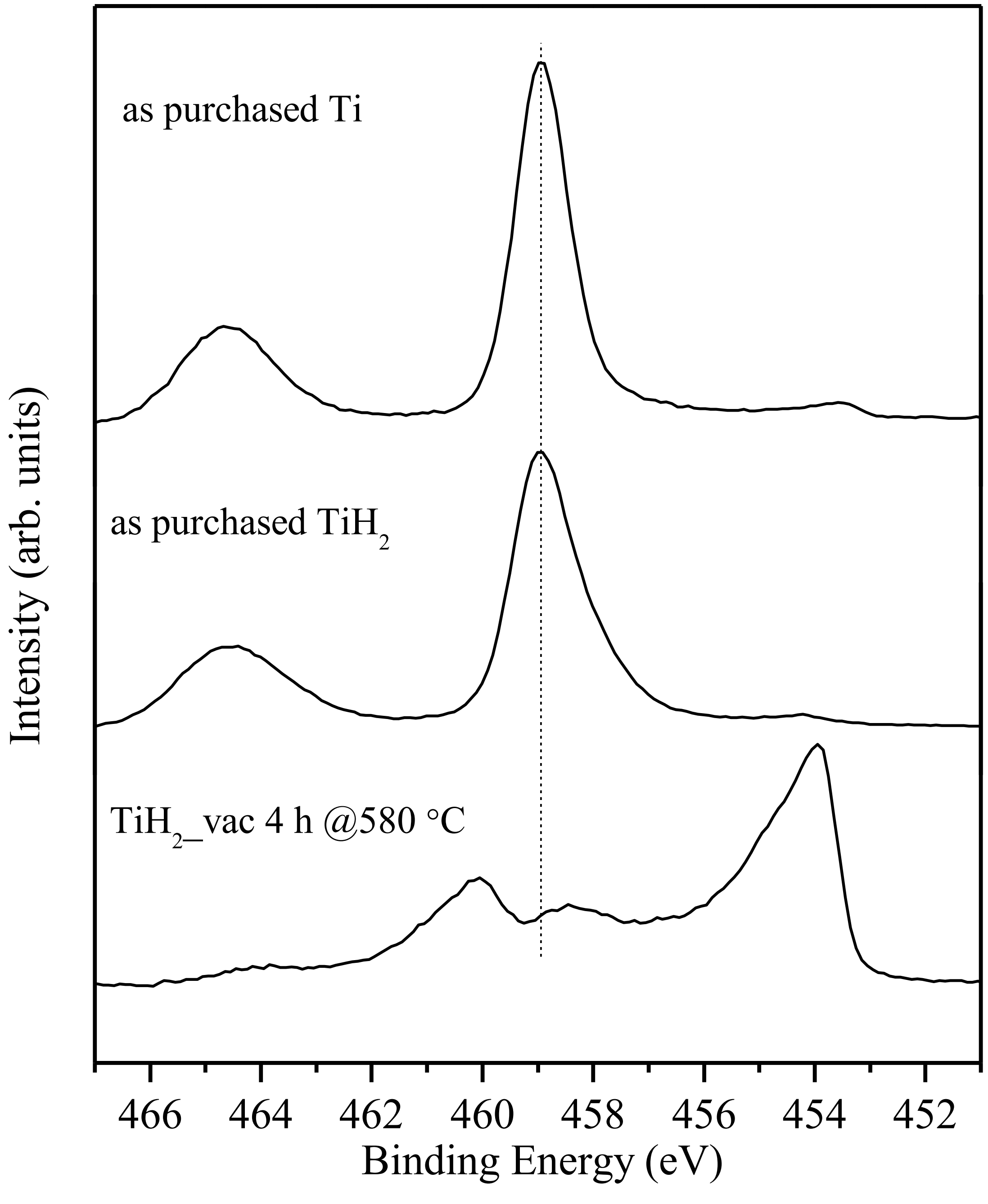

Figure 4.1.5 Ti2p XPS results of the pristine Ti, TiH_2, and the dehydrogenated TiH_2.

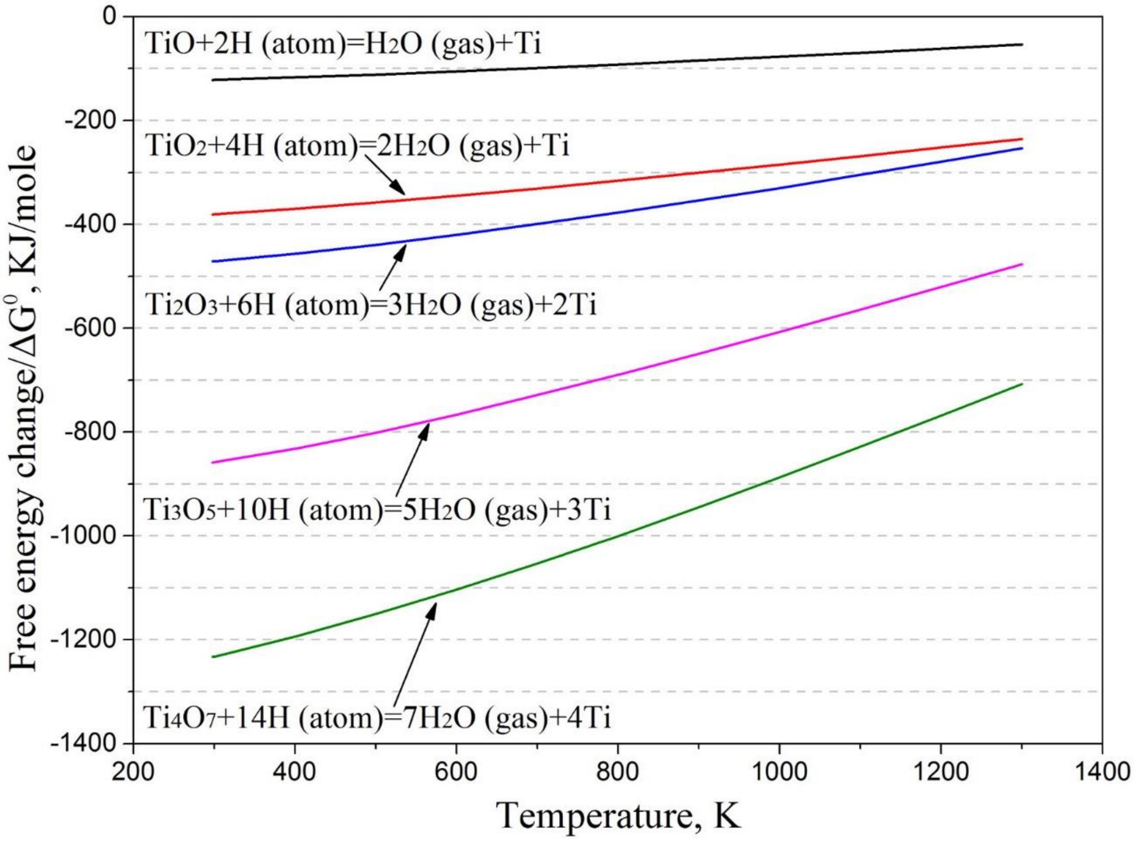

Figure 4.1.6 Standard Gibbs free energy changes in the reaction for hydrogen reduction with different Ti oxides presented by Wang *et al*.[3]

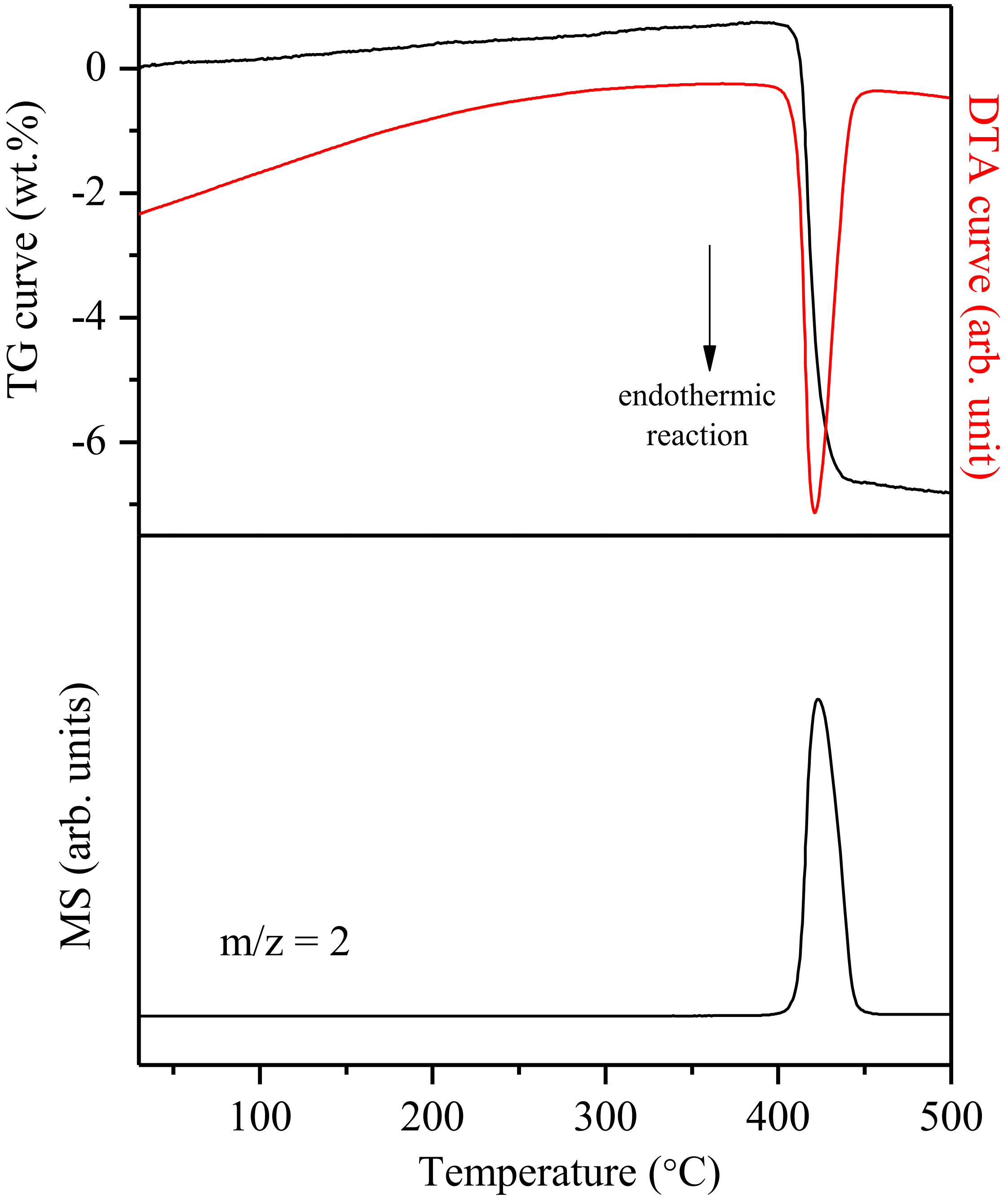

Figure 4.1.7 TG-DTA-MS curve of the pristine MgH_2 measured under 0.1 MPa Ar flow up to 500 °C at 5 °C/min.

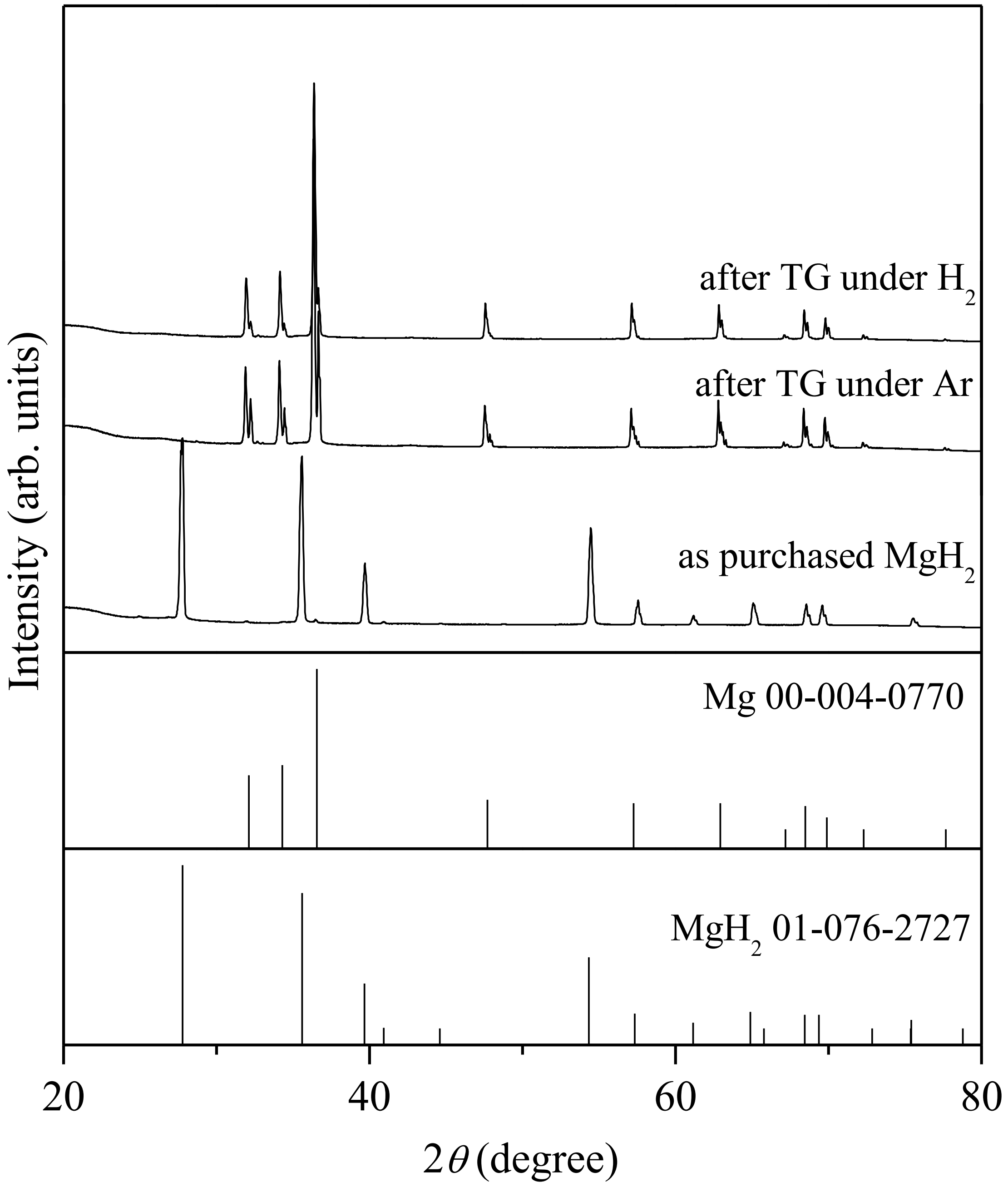

Figure 4.1.8 XRD patterns of the pristine MgH_2 before and after the TG-DTA-MS measurement, performed under Ar flow up to 650 °C at 5 °C/min, and after hydrogen absorption measurement.

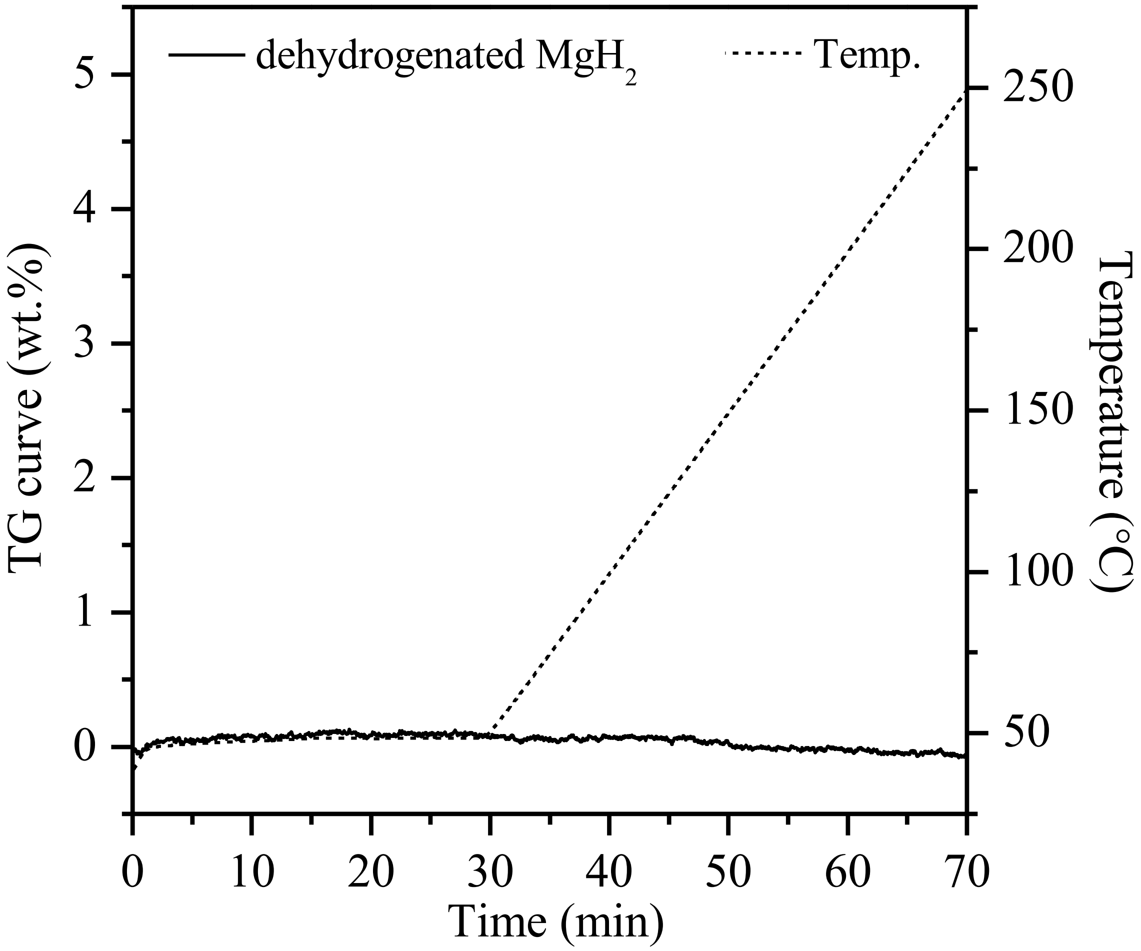

Figure 4.1.9 TG curve of the dehydrogenated MgH_2 performed under 0.1 MPa H_2 up to 250 °C. This measurement was carried out just after dehydrogenation.

4.2 Surface modification by transition metals and oxides to make active sites

In order to make an active site for hydrogen absorption of Ti, the additives were dispersed on the TiH_2 surface by ball-milling. As solid additives, Ni, Pd, Nb_2O_5, and V_2O_5 were chosen, which are well known as catalysts for hydrogenation of Mg.[5,6] To determine the dehydrogenation conditions for preparing the Ti samples from TiH_2 with each solid additive, H_2 desorption profiles of the prepared TiH_2 were obtained using TG-DTA-MS apparatus, and the results are shown in figure 4.2.1. The MS intensity of H_2 was found to be increased continuously from 100 °C for all the ball-milled samples. The results indicate that the ball-milled samples desorbed H_2 with increasing temperature from low temperature, whereas the H_2 desorption of the pristine TiH_2 could be started from 400 °C. These results suggested that the ball-milling affected the H_2 desorption properties of TiH_2 significantly. It is known that the crystallite size and defects of material are important factors for discussion of the hydrogen desorption kinetics. Crystallite size can be estimated by the full width at half maximum (FWHM) of the XRD peaks. The XRD patterns of the ball-milled samples are shown in figure 4.2.2. The peaks were broadened after ball-milling compared with the peaks of the pristine TiH_2, suggesting that the crystallite size was decreased by the ball-milling. In addition to the effects of the crystallite size, Suzuki *et al.* reported that stress and deformation also affect the destabilization of H atoms in TiH_2. It leads to low temperature hydrogen desorption.[7] No significant effects of additives were observed on the H_2 desorption of Ti. The results indicated that the activation energy for hydrogen desorption does not change by the additives. Basically, typical additives provide active sites for the surface reaction such as the recombination of the H atoms.[8] These results indicated that the rate-controlling step of the hydrogen desorption of TiH_2 was not surface reaction. It is considered that the activation energy originated in the large enthalpy change for dehydrogenation of TiH_2 because TiH_2 is quite stable. After the heating, Ti was observed by XRD measurement (figure 4.2.2). According to the H_2 desorption profiles, the dehydrogenating treatment was conducted at 550 °C (corresponding to the peak temperature of hydrogen desorption) under dynamic vacuum. The XRD results of the ball-milled TiH_2 samples after the dehydrogenation treatment are shown in figure 4.2.3. The diffraction pattern of Ti phase was mainly observed in all the heat-treated samples. By using the dehydrogenated samples, hydrogen absorption properties were investigated to evaluate the effects of solid additives for hydrogenation of Ti. Figure 4.2.4 shows the TG curves of the prepared samples performed under 0.1 MPa H_2 flow. All the Ti samples showed weight gain due to hydrogenation at more than 200 °C, which was higher than that of the Ti kept in the glove box for 1 day (figure 4.1.3b). Since these were prepared by the dehydrogenation of TiH_2 samples, these samples should have an active surface for H_2, which is similar to the dehydrogenated pristine TiH_2. However, the higher temperatures required for hydrogenation, indicated that inactivation proceeded more easily than that of the dehydrogenated pristine TiH_2 due to surface oxidation. The enhanced oxidation might be due to increase of the surface area during ball-milling. Since remarkable additive effects could not be achieved, it was expected that the influence of surface oxidation was much larger than the effects of those additives. Light element based hydrogen storage materials such as Mg require the effective catalysts to improve the hydrogenation kinetics because of poor H_2 dissociation ability of the metallic Mg surface. On the other hand, it was clarified that Ti essentially possesses the active surface for dissociation of H_2 molecules, considering the results shown in figure 4.1.3b. When the oxide layer was formed on the Ti surface, hydrogenation is inhibited because hydrogen cannot penetrate into the oxide layer at room-temperatures. In fact, oxidation of the Ti surface might be accelerated by the additives and the increased surface area. In order to control the kinetics of Ti, surface modification to prevent oxidation is important rather than activation for the reaction with H_2. Therefore, the characteristic Ti surface with selective reactivity of H_2 and protection against O_2 and H_2O were required.

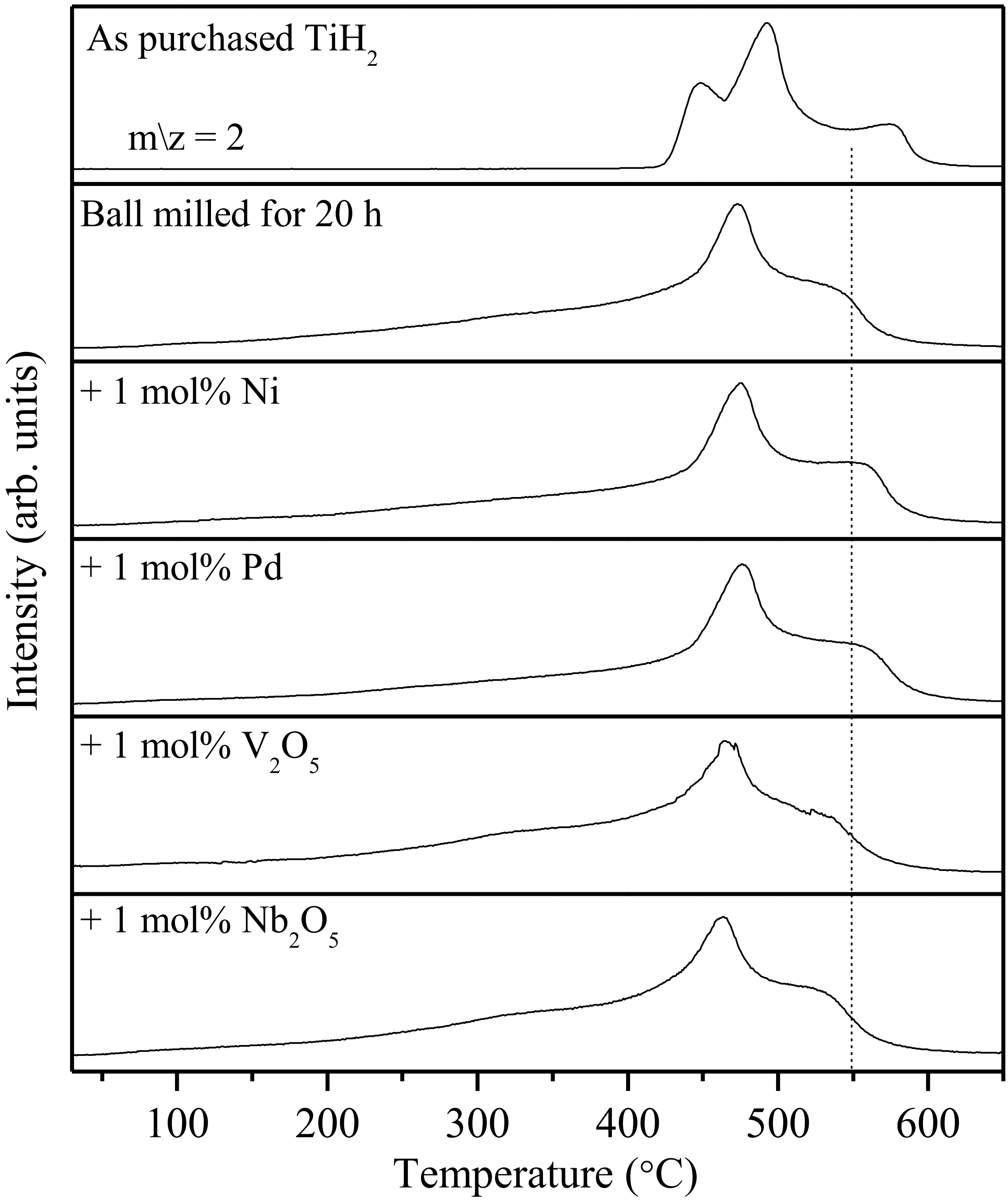

Figure 4.2.1 MS curves of H_2 for the TiH_2 samples, measured under 0.1 MPa Ar flow up to 650 °C at 5 °C/min.

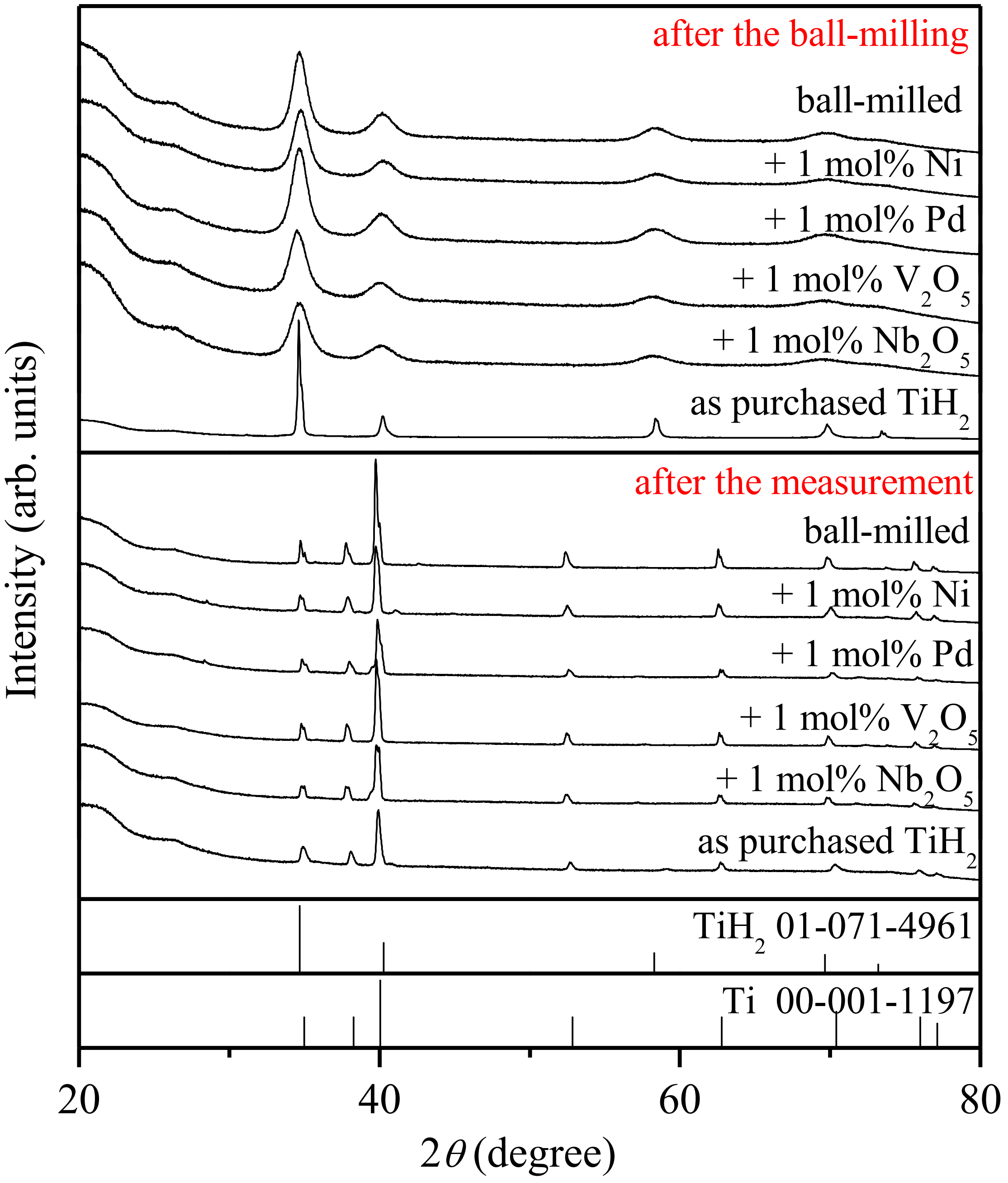

Figure 4.2.2 XRD patterns of the TiH_2 samples. These measurements were performed before and after the heating under 0.1 MPa Ar flow up to 650 °C at 5 °C/min.

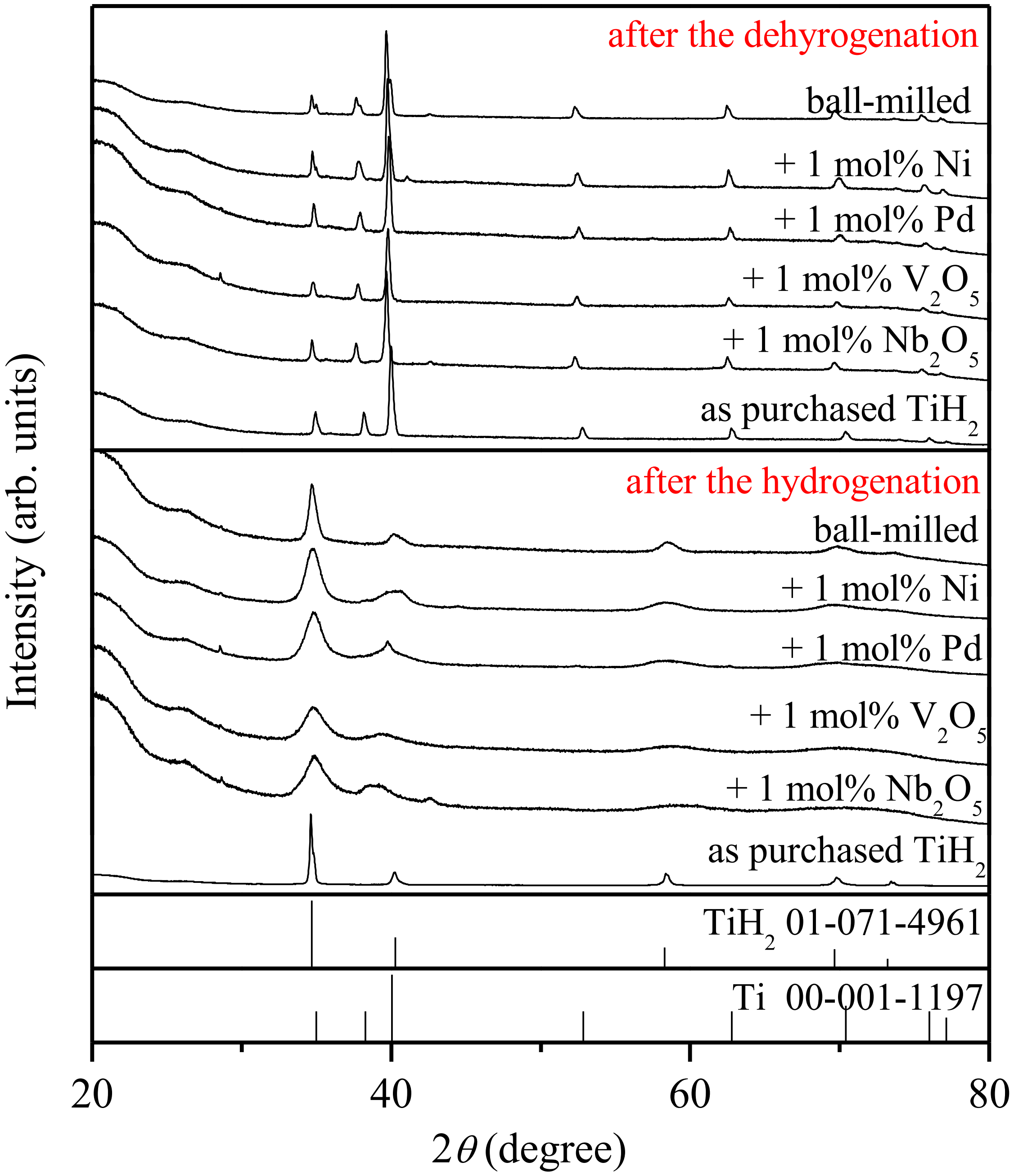

Figure 4.2.3 XRD patterns of the TiH_2 samples. These measurements were carried out after heat treatment under dynamic vacuum up to 550 °C for 4 h, and after TG measurements under 0.1 MPa H_2 flow up to 400 °C.

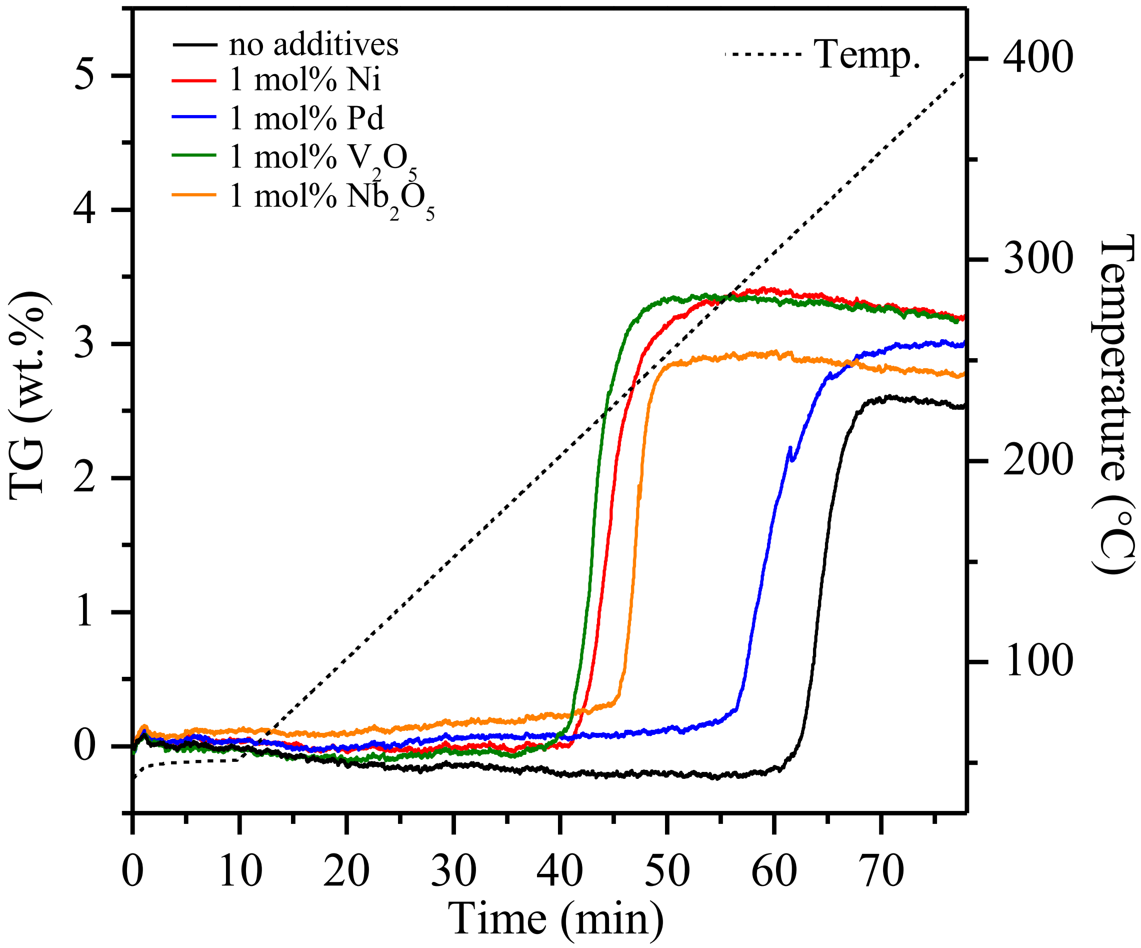

Figure 4.2.4 TG curves of TiH_2 ball-milled without additive and with each additive measured under 0.1 MPa H_2 flow.

4.3 Surface modification by organic solvents and graphite to prevent the surface oxidation

Organic solvents

As another surface modification technique, Ti was ball-milled with various kinds of organic solvents. It was expected that solvents might react with Ti during ball-milling, and the characteristic surface might be generated on the Ti surface. The XRD analyses shown in figure 4.3.1 suggested that the phase transformation from Ti to TiH_2 occurred during TG measurement, performed under 0.1 MPa H_2 up to 400 °C. Figure 4.3.2 shows the TG curves of ball-milled Ti with each organic solvent. Ti_{Xylene} absorbed H_2 even around room temperature, suggesting that the effective surface for hydrogenation of Ti could be formed by the ball-milling with xylene. Although the significant effects of organic solvent for TiFe alloy have been reported, it was speculated that the solvents including oxygen atoms in the molecule accelerate oxidation and inactivation of Ti due to its highly active nature towards O_2. However, in this work, $Ti_{Acetone}$ and Ti_{THF} could absorb H_2 at lower temperature compared with that of Ti_{Dry}, $Ti_{Cyclohexane}$, and Ti_{Hexane}. It is noteworthy here that the hydrogen was absorbed at around room temperature by $Ti_{Acetone}$. Thus, the Ti surface could be modified by the reaction with acetone during the ball-milling process. As mentioned earlier, all the hydrogen absorption properties of the samples were evaluated after keeping the samples in the glovebox for more than 1 day. Therefore, the influence of O_2 and H_2O was suppressed by acetone as well as xylene compared to the other samples. In other words, O_2 and H_2O molecules could not pass through the modified Ti surface, but H_2 selectively penetrated into the surface and reacted with Ti. This phenomenon is quite similar to membrane separation of H_2.

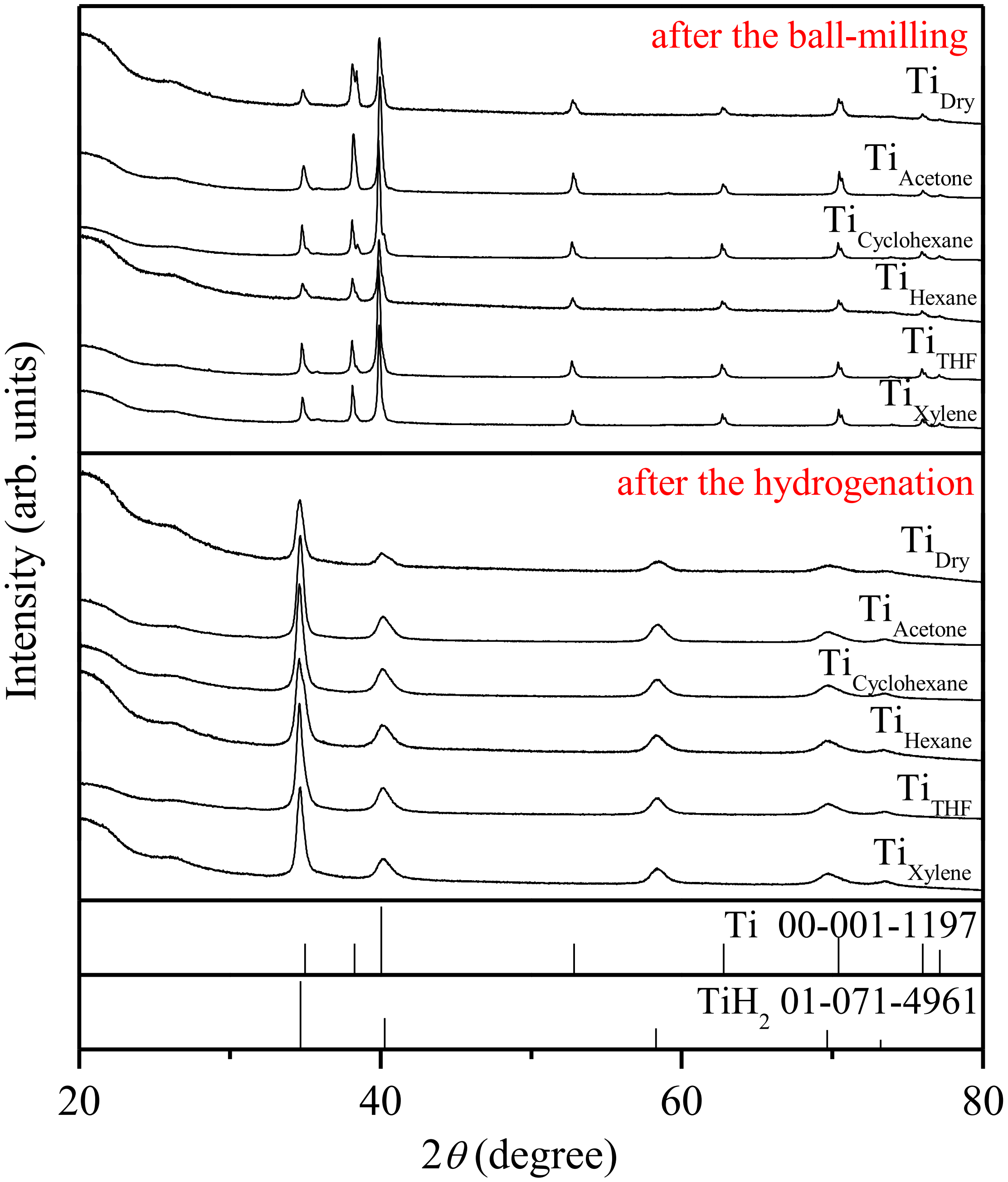

Figure 4.3.1 XRD profile of ball-milled Ti with and without additives after ball-milling and after TG measurement under 0.1 MPa H_2 flow.

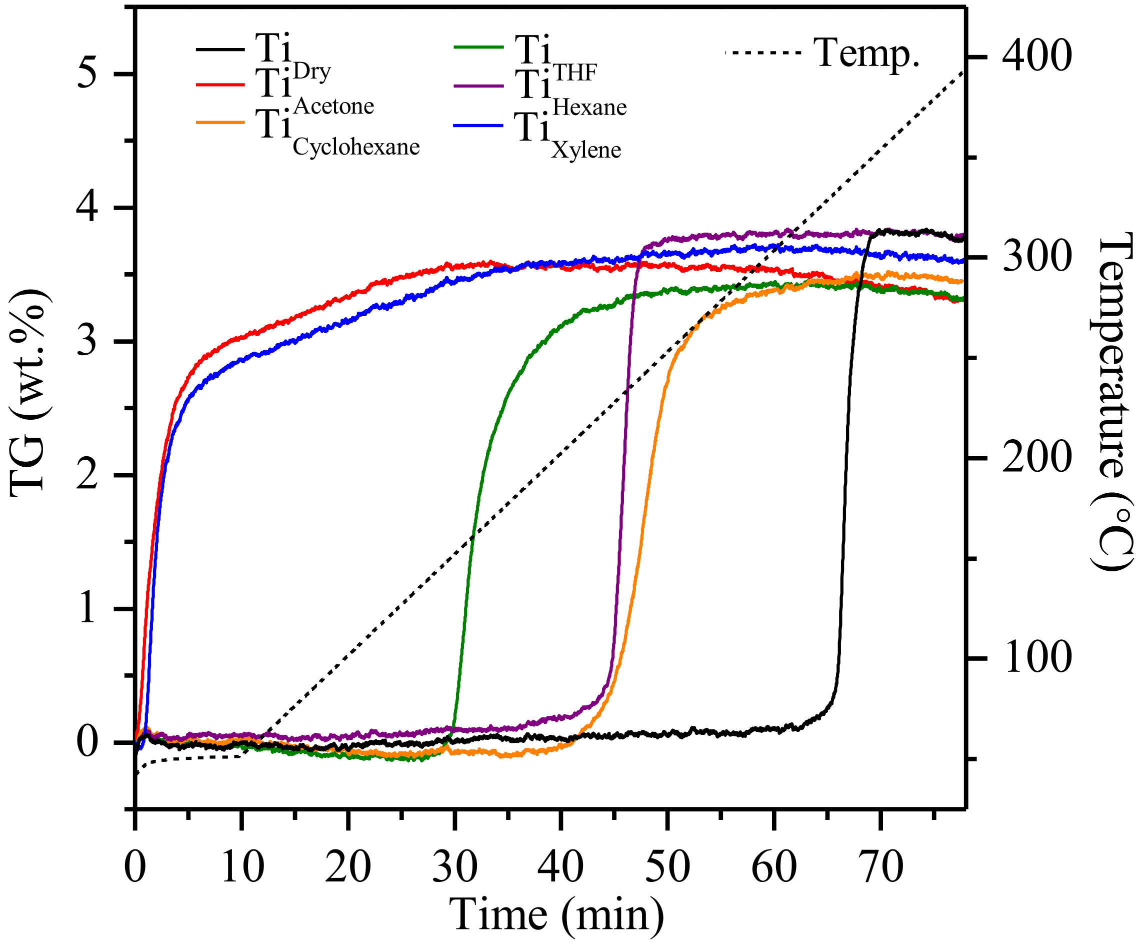

Figure 4.3.2 TG curves of ball-milled TiH_2 with and without solvents measured under 0.1 MPa H_2 flow.

Xylene and acetone

In order to understand the details of the effective factors for surface modification, 2-methyl-4-pentanone and *cis*-1,2-dimethylcyclohexane, whose structure are similar to acetone and xylene, respectively, were investigated in addition to $Ti_{Acetone}$ and Ti_{Xylene}. Figure 4.3.3 shows TG curves of the prepared samples, performed under 0.1 MPa H_2 flow at around 40 °C. These measurements were carried out every 24 h after the sample preparation. A weight gain of approximately 3 wt.% was observed in all the samples even around 40 °C during TG measurement, performed just after the sample preparation. The results indicated that all the as-prepared samples were active in the hydrogenation reaction. However, $Ti_{\textit{cis}\text{-1,2-Dimethylcyclohexane}}$ and $Ti_{\text{2-Methyl-4-pentanone}}$ could not absorb H_2 after keeping these in glove box for few days, indicating that *cis*-1,2-dimethylcyclohexane and 2-methyl-4-pentanone did not show significant effects of surface modification. On the other hand, Ti_{Acetone} and Ti_{Xylene} could absorb H_2 even after several days, indicating their positive effect as additives to modify the Ti surface. The degradation of H_2 absorption properties of Ti_{Acetone} and Ti_{Xylene} with time elapsed under glove box was different. The amount of absorbed H_2 by Ti_{Acetone} was decreased gradually, while it was decreased suddenly after 3 days for Ti_{Xylene}. These results indicated that the inactivation mechanism is different in both the samples. Several kinds of mechanism for reaction selectivity have been considered. One possibility was that the modified surface possess the similar properties as of metal membrane. As an example, palladium (Pd) thin film dissociates H_2 molecules on the surface, and then the H atoms diffuse in the Pd film.[9] These metallic membrane can separate H_2 with high selectivity from mixed gas via solution-diffusion mechanism. If the functional surface having metal membrane properties could be formed on the Ti sample, the reactivity of Ti can be kept without inactivation because oxygen and water cannot reach to Ti. However, the Ti samples were turned to inactivated state even in the case of Ti_{Acetone} and Ti_{Xylene}. As a second possibility, the modified surface has similar function as that of porous inorganic membrane such as silica[10,11], through which the gases can permeate in the surface with different permeation rates. In this case, oxygen can also permeate into Ti bulk, indicating Ti would be gradually oxidized. The inactivation behavior of Ti_{Acetone} is similar to this phenomenon. Third possibility was that the modified surface has a function of adsorbent for oxygen and water similar to activated carbon.[12] When the adsorption sites are fully occupied, the gases reach to the Ti surface, leading to an inactivation at once. The inactivation tendency of Ti_{Xylene} is similar to the adsorbent model.

To estimate the amount of carbon in modified surface indirectly, TG-DTA measurement was carried out up to 650 °C under 0.1 MPa of Ar flow. After this measurement, TiC was observed by XRD measurement in all the samples (figure 4.3.4). The TiC/Ti ratio was estimated using (101) plane of Ti, and (200) plane of TiC obtained by XRD measurement shown in figure 4.3.4 without considering the mass absorption coefficient. The calculated TiC/Ti ratio was listed in table 4.3.1. If it is assumed that carbon in modified surface was changed to TiC by heating, the amount of carbon in the $Ti_{\mathit{cis}\text{-1,2-Dimethylcyclohexane}}$ surface should be quite small compared to that of $Ti_{Acetone}$ and Ti_{Xylene}. Therefore, it was considered that TiC precursor should affect H_2 absorption properties. However, the H_2 absorption properties of $Ti_{Acetone}$, Ti_{Xylene}, and $Ti_{4\text{-Methyl-2-pentanone}}$ were clearly different even though the TiC/Ti ratio of each sample is close. Therefore, it was concluded that the amount of TiC precursor had no direct influence on H_2 absorption properties.

To characterize the chemical state of TiC precursor, Raman scattering spectrometry was carried out just after the sample preparation and after the several days elapsed in special vessel to investigate the degradation with time (figure 4.3.5). Here, noise peaks were observed from the apparatus at 1300 and 1550 cm^{-1}. Two characteristic peaks were clearly observed in 1300 to 1400 cm^{-1} and 1500 to 1675 cm^{-1} for the spectrum of $Ti_{Acetone}$. These peak were assigned to D band and G band, respectively.[13,14] The peaks corresponding to sp^3-carbon and defects of hexatomic rings would appear in the D band area, while those in the G band correspond to local sp^2 -bonded carbon. However, it was surprising that D band and G band appeared in the spectrum of $Ti_{Acetone}$ even though acetone does not have hexatomic rings. From this result, it was considered that acetone was reformed by reaction with Ti, suggesting that carbon was dissolved in the Ti surface. Namely, TiC_x was generated on the $Ti_{Acetone}$ surface as a TiC precursor. The results of TEM observation for $Ti_{Acetone}$ are shown in figure 4.3.6. From the FFT patterns, the metallic Ti was observed with high intensity. On the other hand, other spots were detected, which could not be assigned to metallic Ti, and these yellow spots were assigned to TiC_xH_y such as $TiC_{0.5}H_{0.21}$ and $TiC_{0.47}H_{0.18}$. The IFFT image obtained from the spots of metallic Ti and TiC_xH_y, respectively. In this technique, the existence areas originated the spots of compounds become lightened. These images revealed that TiC_xH_y (originated yellow spots) exists in the outside of the particle. Thus, it could be considered that TiC_xH_y could be considered as one of the possible precursors. The peak intensity in the Raman spectra for $Ti_{Acetone}$ was found to be decreased day-by-day. This result indicated that TiC_x was metastable state, and the surface was degraded with time. The degradation properties were consistent to the H_2 absorption properties. On the other hand, $Ti_{\textit{cis}\text{-1,2-Dimethylcyclohexane}}$ and $Ti_{\text{4-Methyl-2-pentanone}}$, which did not improve the hydrogenation properties of Ti, did not show clear peaks. Thus, it was clarified that TiC_x (or TiC_xH_y) formed on the $Ti_{Acetone}$ affected the hydrogenation properties of Ti. In other words, the chemical state of TiC precursor was important for the reaction selectivity. Although the peak intensity of Ti_{Xylene} was lower than $Ti_{Acetone}$, the Raman spectrum was similar to one of $Ti_{Acetone}$. However, the peak intensity did not decrease with time even after loss of the reactivity with H_2. This result suggested that the state of carbon observed in Ti_{Xylene} surface was different from TiC_x observed in $Ti_{Acetone}$. The stable G band peak was originated in the molecular structure of xylene with hexatomic ring. Considering the H_2 absorption properties, the surface of Ti_{Xylene} had the effects of adsorbent. If xylene-based product with high surface area like graphite is formed, the adsorbent effects can be understood. The spectrum of

Ti_{Xylene} was similar to amorphous carbons with a mixture of sp^2 and sp^3 hybrid orbitals.[13] Therefore, it is possible that the amorphous carbons formed on the Ti_{Xylene} surface played the role of adsorbent for water and oxygen. Thus, it was clarified that the mechanism of reaction selectivity is different between $Ti_{Acetone}$ and Ti_{Xylene}. However, the details of TiC precursor such as composition and structure were not identified. Thus, further experiments are necessary to understand the details of TiC precursor as future works. Here, D band and G band in the Raman spectrum were often discussed for graphite based materials. In other words, graphite has large amount of carbon originated in D band and G band structure. Therefore, it was considered that the functional surface like $Ti_{Acetone}$ and Ti_{Xylene} can be obtained by ball-milling with graphite. Thus, the effects of graphite was investigated and the results are summarized in next section for further improvement of the hydrogen absorption properties of Ti.

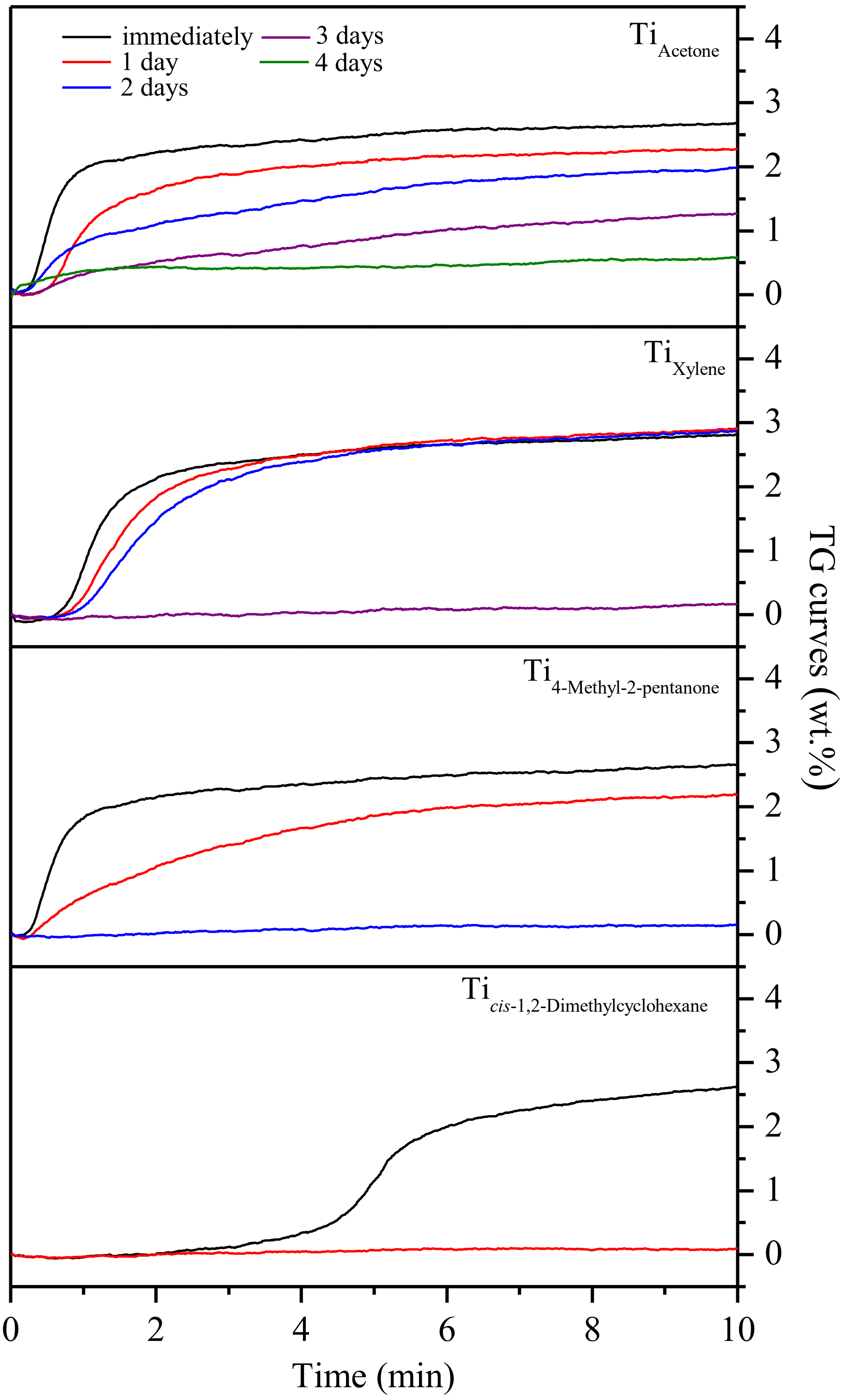

Figure 4.3.3 TG curves of Ti$_{\text{Acetone}}$, Ti$_{\text{Xylene}}$, Ti$_{\text{2-Methyl-4-pentanone}}$, and Ti$_{cis\text{-1,2-Dimethylcyclohexane}}$, measured under 0.1 MPa H_2 flow around 40 °C. These measurement were carried out every 24 h from sample preparation.

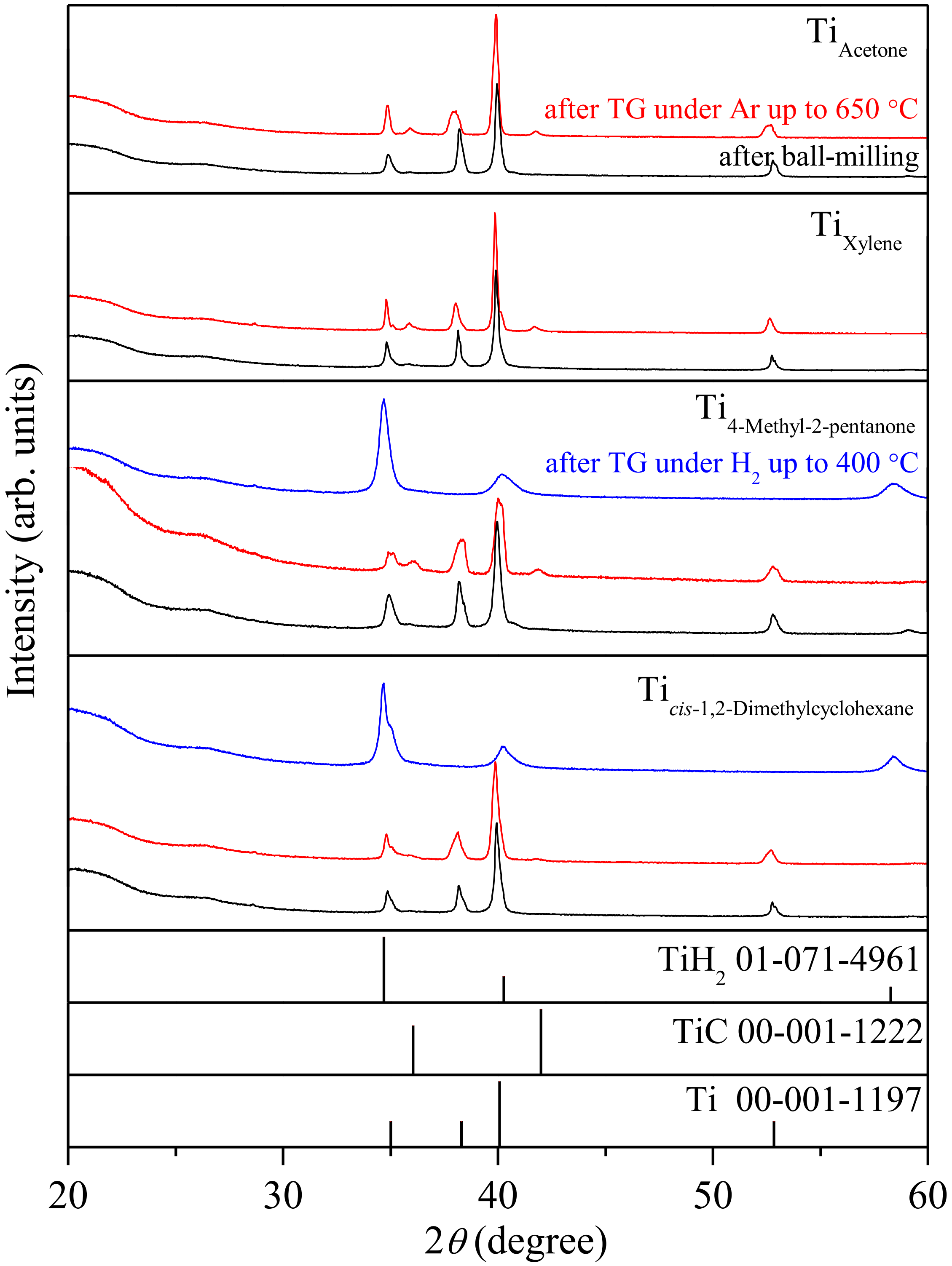

Figure 4.3.4 XRD patterns of Ti$_{Acetone}$ and Ti$_{Xylene}$ before and after TG measurement. TG measurement was performed under Ar atmosphere up to 650 °C.

Table 4.3.1 TiC/Ti ratio of each sample heated up to 650 C under Ar flow. Ti : C (carbon) was the initial molar ratio of ball-milling. The mole of C was estimated by 20 wt.% solvents. The peak areas of Ti and TiC were calculated using (101) plane for Ti, and (200) plane for TiC without considering the mass absorption coefficient, respectively.

Sample name	Ti : C	Area ratio of TiC/Ti
$\mathrm{Ti}_{\mathrm{Acetone}}$	1 : 0.5	0.06
$\mathrm{Ti}_{\mathrm{Xylene}}$	1 : 0.7	0.07
$\mathrm{Ti}_{cis\text{-}\mathrm{1,2\text{-}Dimethylcyclohexane}}$	1 : 0.6	0.03
$\mathrm{Ti}_{\mathrm{4\text{-}Methyl\text{-}2\text{-}pentanoen}}$	1 : 0.7	0.08

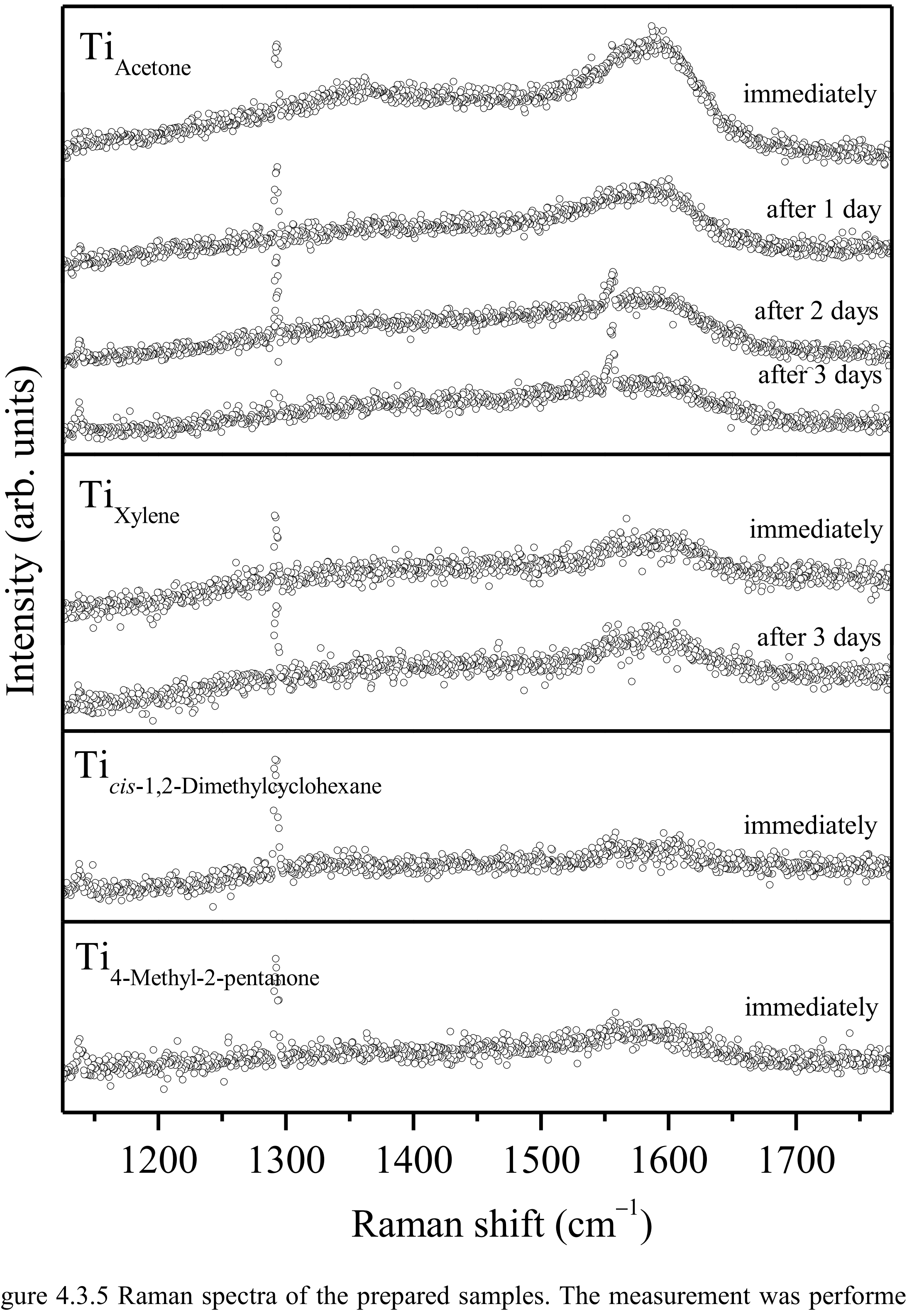

Figure 4.3.5 Raman spectra of the prepared samples. The measurement was performed just after sample preparation and after several days.

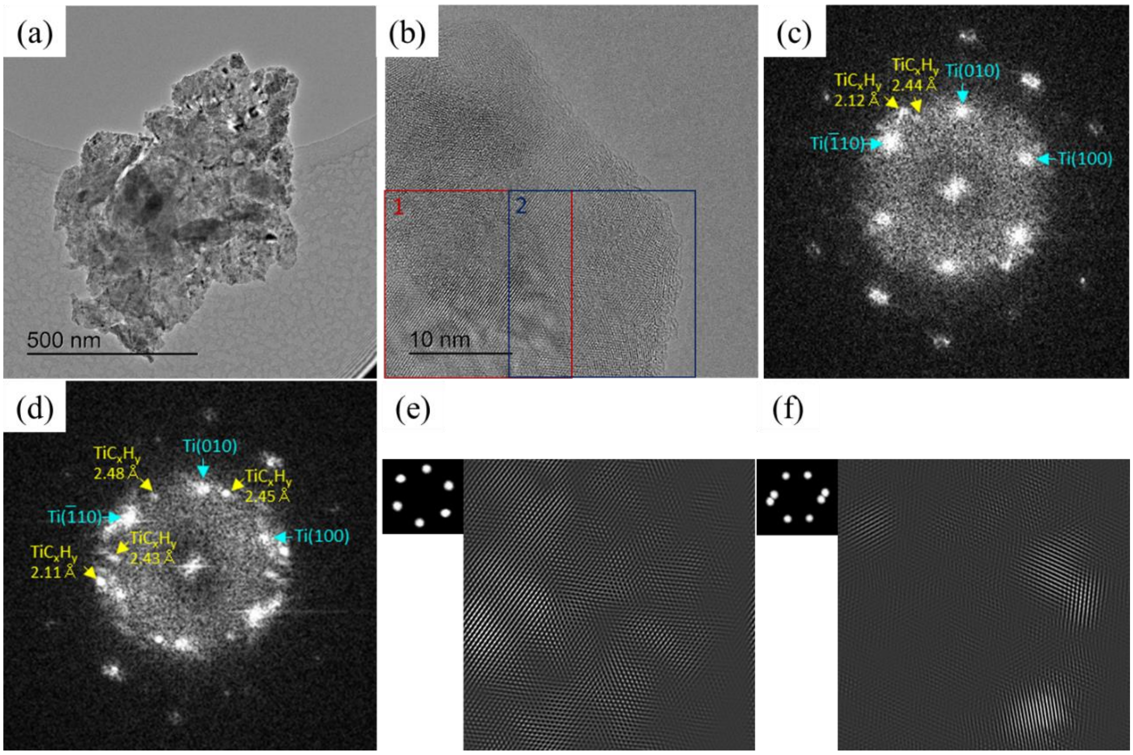

Figure 4.3.6 TEM observation results of $Ti_{Acetone}$. (a) TEM bright-field and (b) high resolution TEM (HRTEM) images. The Fast Fourier Transform (FFT) patterns were acquired from (c) area 1 and (d) area 2. Inverse FFT images from (e) blue spots and (f) yellow spots in area 2.

Graphite

From the discussion for the Ti ball-milled with organic solvents, it was concluded that graphite structure could have effects of surface modification. Therefore, Ti ball-milled with graphite ($Ti_{Graphite}$) was synthesized and investigated. Figure 4.3.7 shows XRD results of $Ti_{Graphite}$ with various treatment. After the ball-milling, only Ti phase was observed without graphite peaks. This result suggested that graphite structure was broken and it was dispersed on the Ti surface. The TG curves performed under 0.1 MPa H_2 flow at around 40 °C are shown in figure 4.3.8. A weight gain of approximately 3.4 wt.% was observed during the TG measurements, and the phase change from Ti to TiH_2 was clearly confirmed by XRD measurement. Therefore, hydrogenation occurred during the TG measurement around 40 °C. While the reactivity of $Ti_{Acetone}$ and Ti_{Xylene} with H_2 was lost after keeping these in glove box for several days, $Ti_{Graphite}$ could absorb H_2 around 40 °C even after 7 days. This result indicated that graphite has superior effects for selective H_2 absorption of Ti. Furthermore, even though the H_2 absorption temperature was increased after exposing $Ti_{Graphite}$ to the air for 1 day, it showed lower reaction temperature compared to Ti without any surface modification and high stability without burning in air (figure 4.3.9). The amount of adsorbed H_2 (3.4 wt.%) was close to the value estimated from the mixture of Ti and graphite without any reaction between both materials (3.7 wt.%), indicating excess graphite remained in the sample. Here, Wei Ye *et al.* reported H_2 absorption properties of Ti/graphene composite with Kubas-type interaction between 100 and 300 °C.[15] Although the theoretical H_2 capacity of pure Ti is 4.2 wt%, the Ti/graphene composite (20 wt% graphene) absorbed 4.3 wt% H_2, which was believed due to Kubas-type interaction at 300 °C. On the other hand, H_2 capacity of $Ti_{Graphite}$ was close to the value of the mixture as mentioned above, indicating $Ti_{Graphite}$ did not show the Kubas-type interaction. The TiC/Ti ratio was 0.82, which was estimated by XRD patterns with heating up to 650 °C. This value was much higher than that of the Ti ball-milled with organic solvents. Therefore, it was suggested that carbon was effectively doped on the Ti surface by graphite.

In order to characterize the carbon on the $Ti_{Graphite}$ surface, Raman spectrometry was carried out. Figure 4.3.10 shows the Raman spectra of the pristine graphite and $Ti_{Graphite}$. The measurements of $Ti_{Graphite}$ were performed just after sample preparation and after 3 days. Here, it should be note that the spectrum of $Ti_{Graphite}$ includes residual graphite as mentioned in the discussion for TG results. D band (1300 ~ 1400 cm^{-1}) and G band (1500 ~ 1675 cm^{-1}) were detected in the pristine graphite, then the D/G ratio was increased after ball-milling. In addition, the spectrum of $Ti_{Graphite}$ was similar to turbostratic carbon.[16] These results suggested that graphite structure was partially broken by the ball-milling. The results were consistent to the XRD results. In addition, the peak intensities of D band and G band in Raman spectra were not changed after 3 days. This result indicated that the carbon existed on the $Ti_{Graphtie}$ was stable. For the H_2 separation using turbostratic carbon, the gaseous molecules permeate into turbostratic carbon through its pore or cracks. The permeability of molecules into carbon was suggested to be dependent on the kinetic diameter. Therefore, the permeation of oxygen was inhibited due to larger size than H_2. In addition, Wollbrink *et al.* reported that the permeation of water could be prevented due to hydrophobic characteristics of carbon.[16] Therefore, it was indicated that turbostratic carbon can prevent the permeation of water as well as oxygen. Although it was difficult to know the chemical state of Ti species on the $Ti_{Graphite}$ surface by Raman spectroscopy, turbostratic graphite existed in the $Ti_{graphite}$.

XPS measurements were also conducted to understand the chemical state of the $Ti_{Graphite}$ surface, and the results are shown in figure 4.3.11. The measurements were performed by using the apparatus of JPS-9200. As discussed in the Ti_{Fresh} part, the pristine Ti was covered by the TiO_2 layer (Ti^{4+}). In the case of the pristine TiC, the low-valence Ti was detected at 454.8 eV (and 460.8 eV) with higher intensity, which was consistent with typical $Ti2p_{3/2}$ (and $Ti2p_{1/2}$) peak of TiC.[17] TiO_2 peak was also observed in the pristine TiC with lower intensity. The spectrum of TiC indicated that the oxide layer on the TiC particle was thinner than one of the pristine Ti. The spectrum of $Ti_{Acetone}$ was similar to the pristine TiC, indicating TiC_x existed on the $Ti_{Acetone}$. This result was consistent with the results of the Raman spectrum and TEM observation for $Ti_{Acetone}$. $Ti_{Graphite}$ also showed a peak at 454.8 eV in the Ti 2p XPS spectrum, indicating TiC_x was formed by the ball-milling of Ti and graphite. It is noteworthy that the intensity was quite low compared with one of $Ti_{Acetone}$, indicating carbon with a thickness of several nm covered Ti particle. Considering the results of the Raman spectrum and XPS, it was concluded that turbostratic graphite covered the Ti surface.

For the further characterization of $Ti_{Graphite}$, TEM observation was carried out and the results are shown in figure 4.3.12. Figure 4.3.12a and 4.3.12b are high-angle annular dark-field scanning TEM (HAADF-STEM) image of $Ti_{Graphite}$ and the energy-dispersive X- ray spectrometry (EDS) mapping of Ti, C, and O elements. For the HAADF-STEM image, electron-rich areas were observed as the bright part. Because Ti element was detected by EDS mapping, the bright part of HAADF-STEM image was mainly corresponding to Ti. EDS mapping of C showed that carbon surrounded the Ti particle. It was also confirmed by HRTEM observation that turbostratic graphite was formed on the Ti surface, which is shown in the inset of figure 4.3.12c. These results were well-consistent with the results of Raman spectra and XPS. Line analyses of energy-loss spectroscopy (EELS) were performed across the boundary between Ti and C. The measurement areas are expressed as a square in figure 4.3.12d. The peaks were observed at 285 eV and in 287 to 310 eV (figure 4.3.12e), which were assigned to π and σ bonding of carbon, respectively.[18] These peak positions and shapes were similar to one of amorphous carbon. Therefore, the mixed carbon phase of amorphous and turbostratic carbons existed on the $Ti_{Graphite}$ surface. This result indicated that $Ti_{Graphite}$ should have the effects of the adsorbent functions for oxygen like Ti_{Xylene} as well as hydrophobic effects for water like turbostratic carbon. For the spectra of Ti $L_{2,3}$-edge in the Ti bulk (areas 1-4), two peaks were observed at 457 and 463 eV. These peaks were corresponding to metallic Ti.[19] The peaks of Ti $L_{2,3}$-edge obtained at the interface between Ti and graphite were shifted to ~1 eV higher energy than metallic Ti (Fig. 4.3.12f). This spectrum was similar to TiC_x reported before.[20] It has been reported that the peaks were gradually shifted to 1.4 eV higher energy with increasing N atom in TiN_x (x = 0 to 1).[19] The presence of TiC_x was already confirmed by XPS measurements (figure 4.3.11). These results indicated that TiC_x was formed in the interface between Ti and graphite. Therefore, it was considered that $Ti_{Graphite}$ should have inorganic porous membrane effects by the TiC_x layer, which had a similar function to that of $Ti_{Acetone}$. Thus, the inactivation of $Ti_{Graphite}$ was prevented by the mixture of turbostratic and amorphous carbons with "hydrophobic adsorbent effects" and the TiC_x layer with inorganic porous membrane effects.

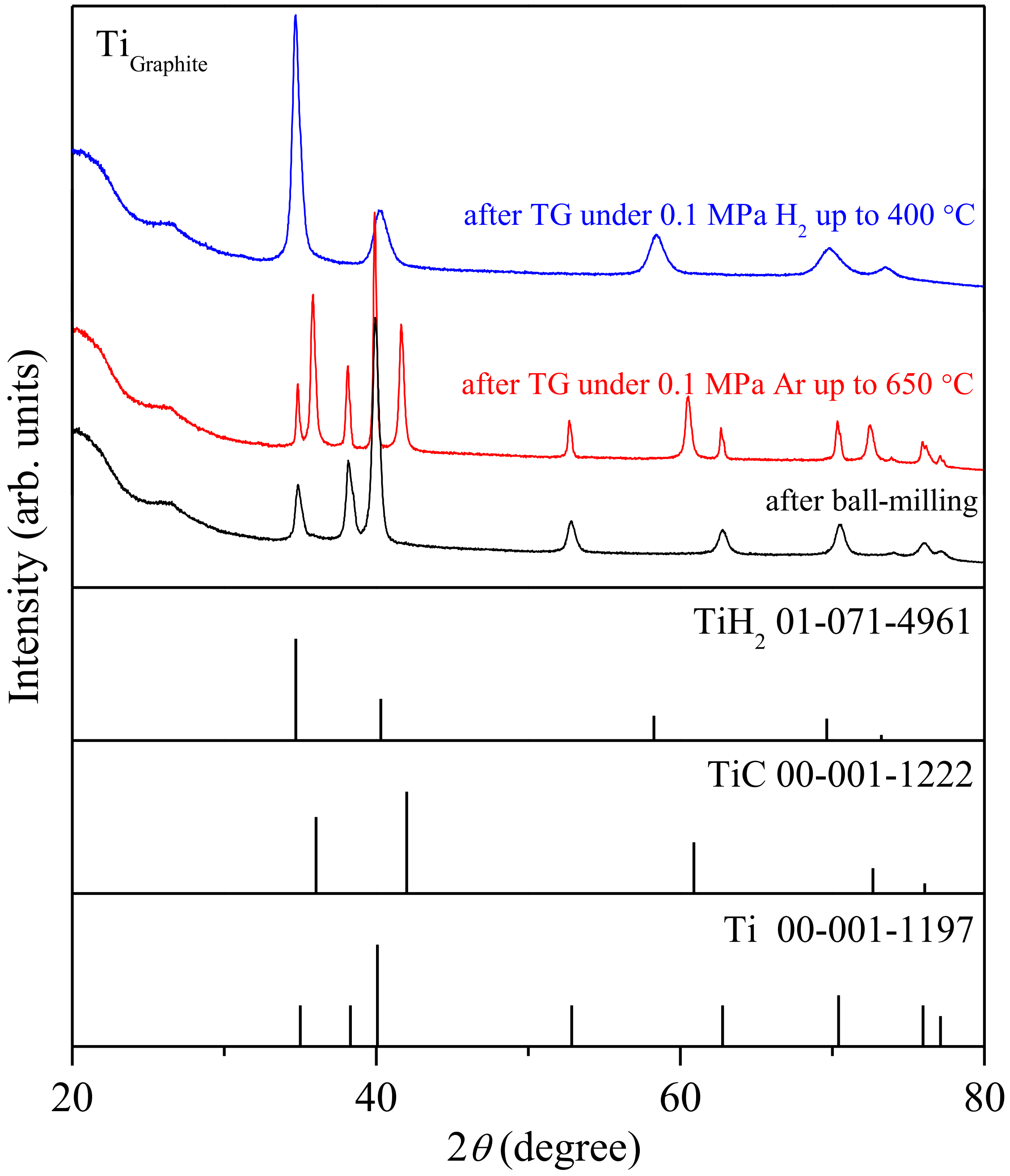

Figure 4.3.7 XRD patterns of $Ti_{Graphite}$ before and after TG measurements. The TG measurements were performed under H_2 or Ar flow up to 400 or 650 °C at 5 °C/mink, respectively.

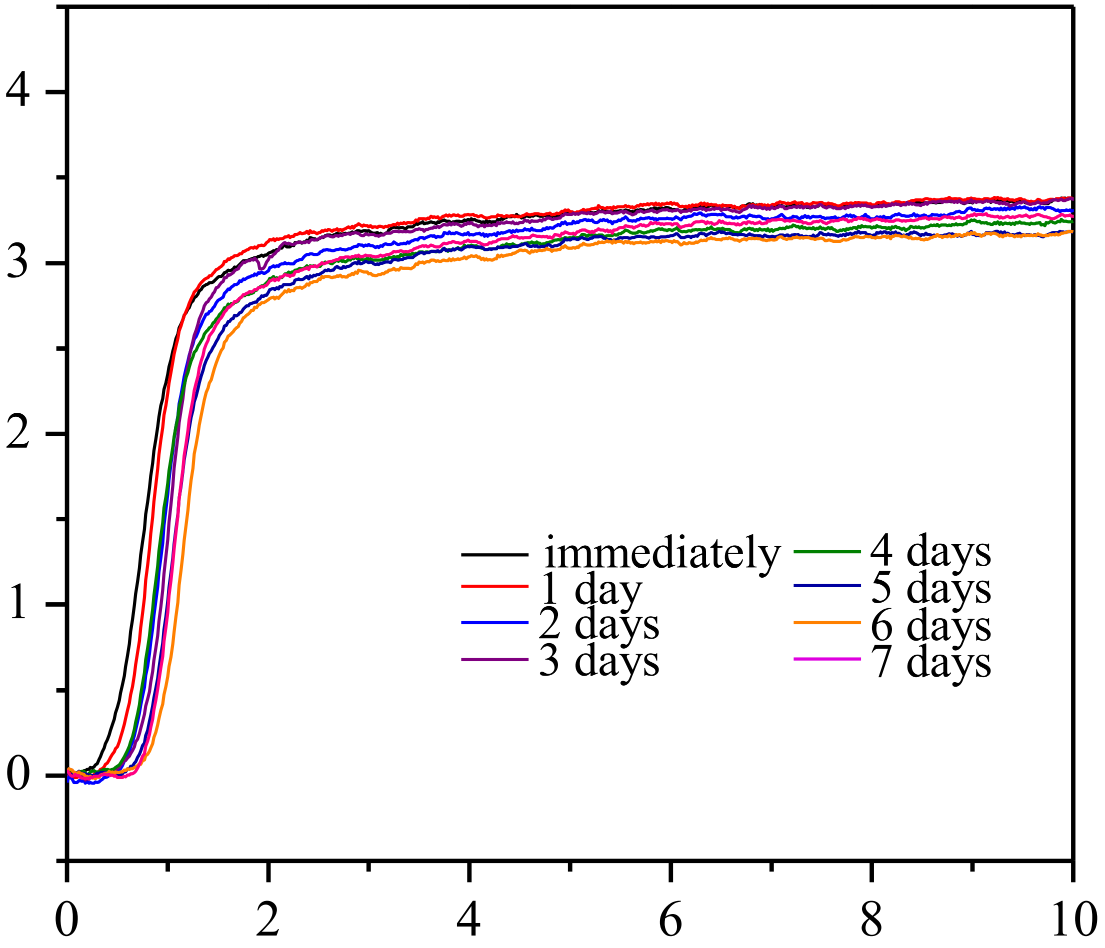

Figure 4.3.8 TG curves of $Ti_{Graphite}$ measured under 0.1 MPa H_2 flow around 40 °C. The measurements were performed every 24 h from sample preparation.

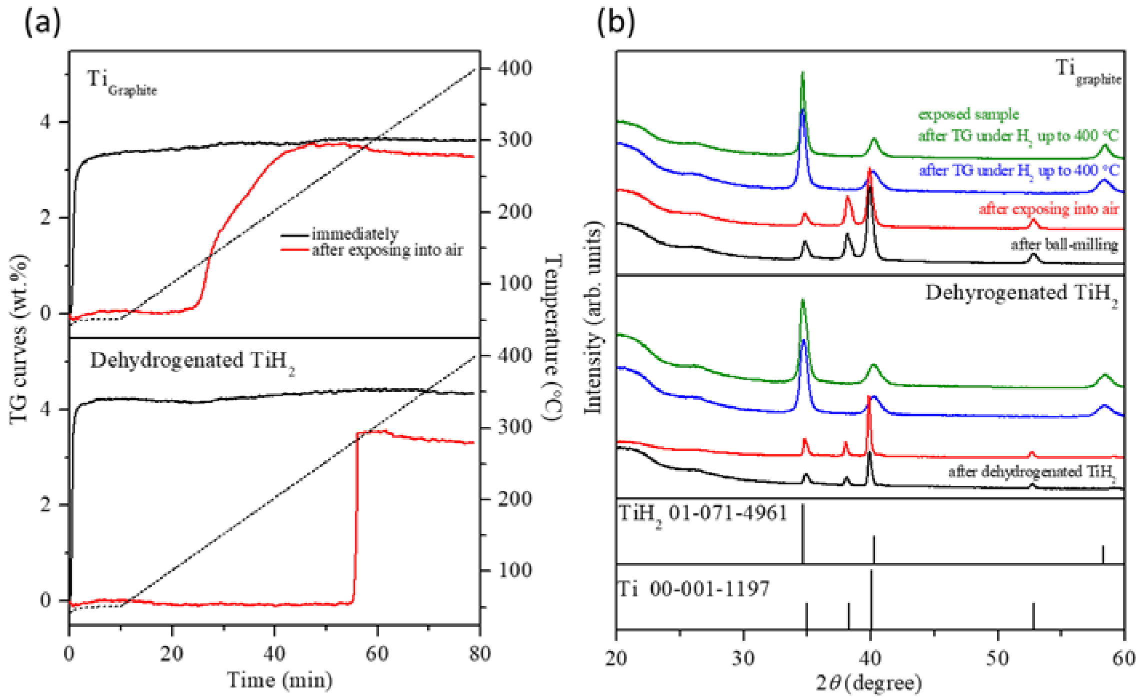

Figure 4.3.9 (a) TG curves of Ti_{Fresh} and $Ti_{Graphite}$ before and after exposing in air for 1 day, performed under 0.1 MPa H_2 flow. (b) XRD patterns of both samples.

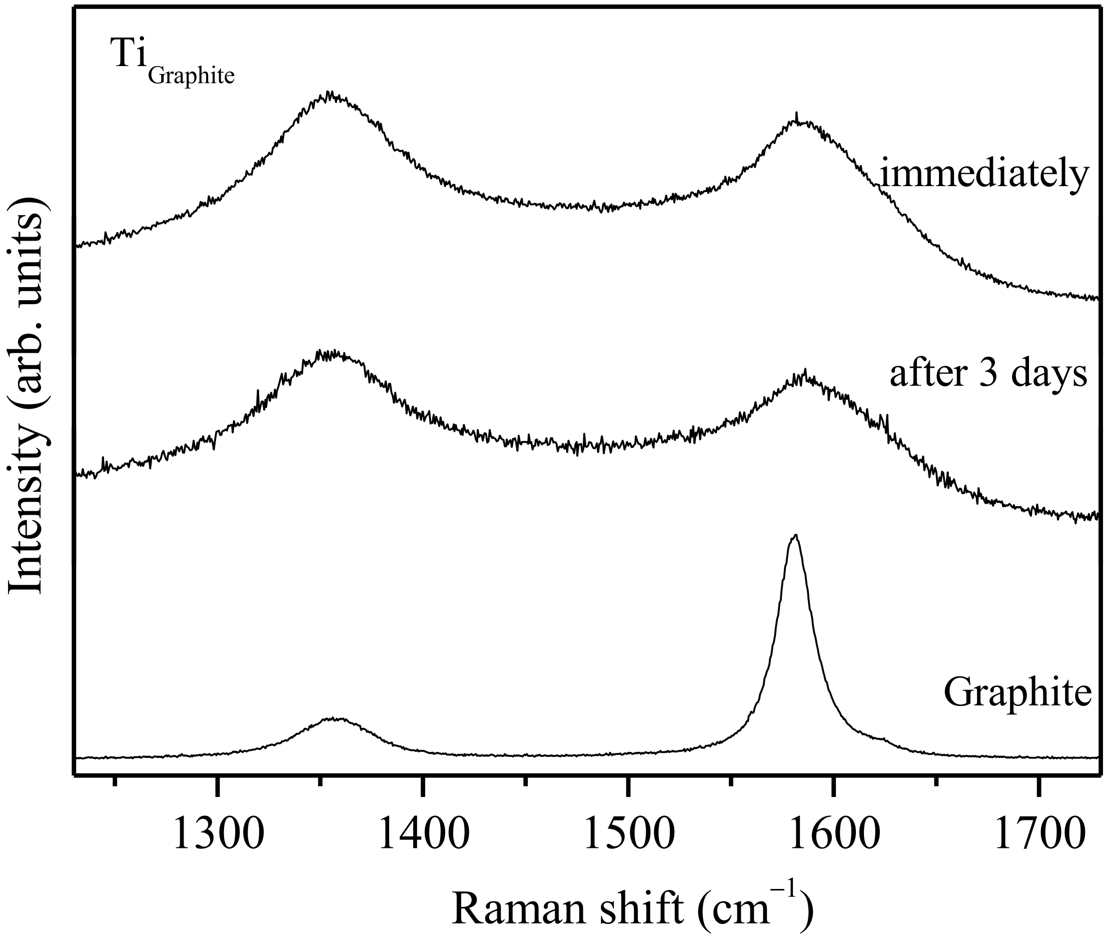

Figure 4.3.10 Raman spectra of the pristine graphite and Ti$_{Graphite}$. The measurements of Ti$_{Graphite}$ were carried out just after sample preparation and after 3 days.

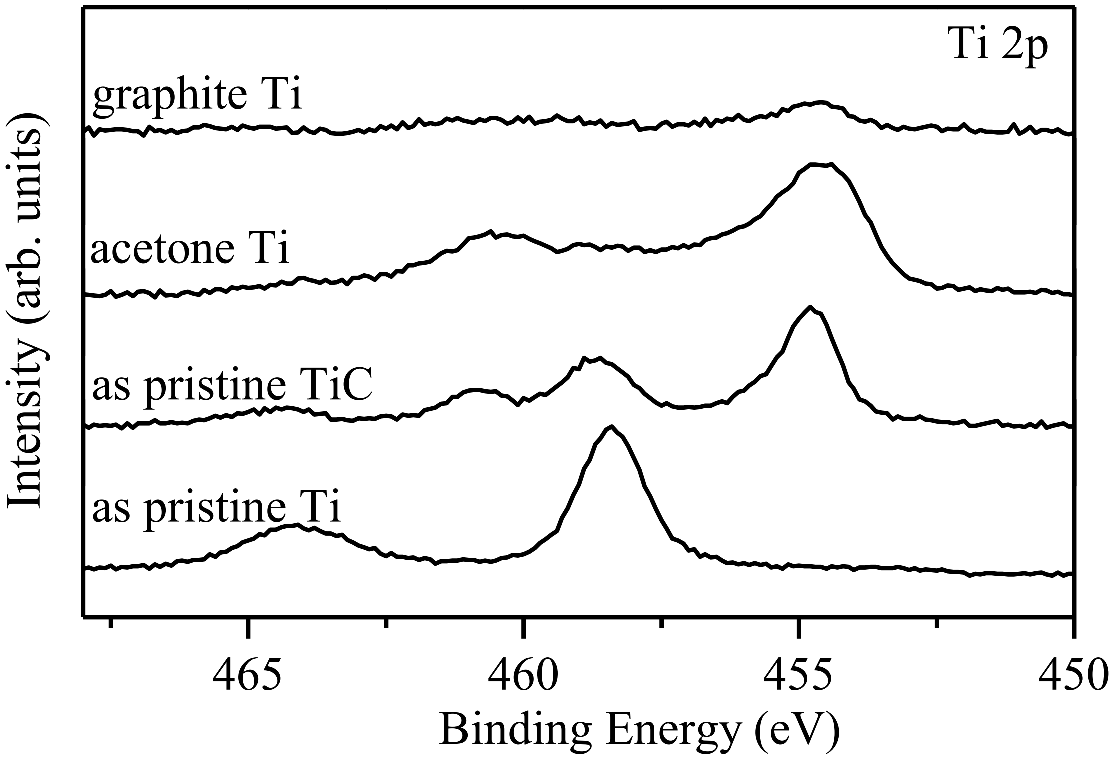

Figure 4.3.11 Ti2p XPS spectra of $\mathrm{Ti}_{\mathrm{Graphite}}$, $\mathrm{Ti}_{\mathrm{Acetone}}$, as purchased TiC, and Ti.

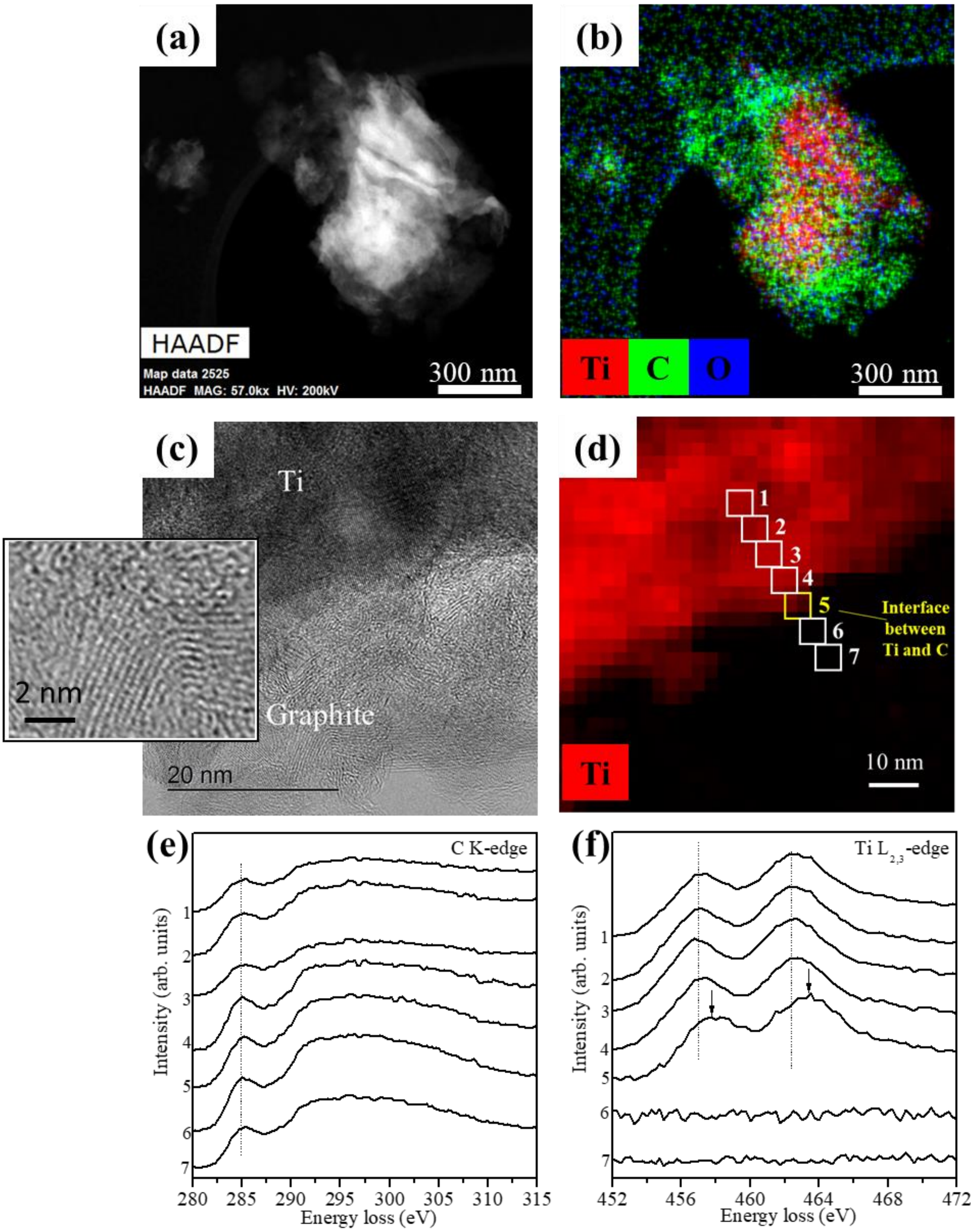

Figure 4.3.12 TEM observation results of Ti$_{\text{Graphite}}$. (a) HAADF-STEM image and (b) EDS mapping of Ti, C, O elements. (c) HRTEM image in the interface between Ti and graphite. Inserted figure is high magnification image of the graphite area. (d) STEM-EELS mapping of Ti, and spectra of (e) C K-edge and (f) TiL$_{2,3}$-edge at each area.

References

1. Milošev, I., Kosec, T. & Strehblow, H. H. XPS and EIS study of the passive film formed on orthopaedic Ti-6Al-7Nb alloy in Hank's physiological solution. *Electrochim. Acta* **53**, 3547–3558 (2008).
2. Wang, C., Pan, L., Zhang, Y., Xiao, S. & Chen, Y. Deoxidization mechanism of hydrogen in TiH_2 dehydrogenation process. *Int. J. Hydrogen Energy* **41**, 14836–14841 (2016).
3. Wang, C. *et al.* XPS study of the deoxidization behavior of hydrogen in TiH_2 powders. *Powder Technol.* **302**, 423–425 (2016).
4. Shang, C. X. & Guo, Z. X. Effect of carbon on hydrogen desorption and absorption of mechanically milled MgH_2. in *Journal of Power Sources* vol. 129 73–80 (Elsevier, 2004).
5. Barkhordarian, G., Klassen, T. & Bormann, R. Fast hydrogen sorption kinetics of nanocrystalline Mg using Nb_2O_5 as catalyst. *Scr. Mater.* **49**, 213–217 (2003).
6. Denis, A., Sellier, E., Aymonier, C. & Bobet, J. L. Hydrogen sorption properties of magnesium particles decorated with metallic nanoparticles as catalyst. *J. Alloys Compd.* **476**, 152–159 (2009).
7. Suzuki, H., Taniguchi, H., Hanada, N., Takai, K. & Hagihara, Y. Effects of deformation on hydrogen absorption and desorption properties of titanium. in *Journal of Alloys and Compounds* vol. 509 S759–S762 (Elsevier, 2011).
8. Hu, M., Xie, X., Chen, M., Zhu, C. & Liu, T. TiC_X-decorated Mg nanoparticles confined in carbon shell: Preparation and catalytic mechanism for hydrogen storage. *J. Alloys Compd.* **817**, 152813 (2020).
9. Uemiya, S. *et al.* Separation of hydrogen through palladium thin film supported on a porous glass tube. *J. Memb. Sci.* **56**, 303–313 (1991).
10. de Vos, R. M., Maier, W. F. & Verweij, H. Hydrophobic silica membranes for gas separation. *J. Memb. Sci.* **158**, 277–288 (1999).
11. Lee, H. R., Kanezashi, M., Shimomura, Y., Yoshioka, T. & Tsuru, T. Evaluation and fabrication of pore-size-tuned silica membranes with tetraethoxydimethyl disiloxane for gas separation. *AIChE J.* **57**, 2755–2765 (2011).
12. Hao, P., Shi, Y., Li, S. & Cai, N. Hydrophobic activated carbon for elevated-

temperature pressure swing adsorption. *Adsorption* (2020) doi:10.1007/s10450-020-00223-6.

13. Zhang, L. & Koka, R. V. A study on the oxidation and carbon diffusion of TiC in alumina–titanium carbide ceramics using XPS and Raman spectroscopy. *Mater. Chem. Phys.* **57**, 23–32 (1998).
14. Mermoux, M., Chang, S., Girard, H. A. & Arnault, J.-C. Raman spectroscopy study of detonation nanodiamond. *Diam. Relat. Mater.* **87**, 248–260 (2018).
15. Ye, W., Chi, Q., Zhou, H. & Gao, P. Ball-milling preparation of titanium/graphene composites and its enhanced hydrogen storage ability. *Int. J. Hydrogen Energy* **43**, 19164–19173 (2018).
16. Wollbrink, A. *et al.* Amorphous, turbostratic and crystalline carbon membranes with hydrogen selectivity. *Carbon N. Y.* **106**, 93–105 (2016).
17. El Mel, A. A., Angleraud, B., Gautron, E., Granier, A. & Tessier, P. Y. XPS study of the surface composition modification of nc-TiC/C nanocomposite films under in situ argon ion bombardment. *Thin Solid Films* **519**, 3982–3985 (2011).
18. Jin, T. *et al.* Mechanical polishing of ultrahard nanotwinned diamond via transition into hard sp^2-sp^3 amorphous carbon. *Carbon N. Y.* **161**, 1–6 (2020).
19. Abdallah, I., Dupressoire, C., Laffont, L., Monceau, D. & Vande Put, A. STEM-EELS identification of TiO_XN_Y, TiN, Ti_2N and O, N dissolution in the Ti2642S alloy oxidized in synthetic air at 650°C. *Corros. Sci.* **153**, 191–199 (2019).
20. Woltersdorf, J., Feldhoff, A. & Lichtenberger, O. The Complex Bonding of Titanium Nitride Layers in C/Mg Composites Revealed by ELNES Features. *Cryst. Res. Technol.* **35**, 653–661 (2000).

5 Conclusion

In this study, the essential H_2 absorption properties of Ti with fresh surface, and the surface modification techniques to improve the H_2 absorption kinetics were investigated.

(1) The reaction between Ti and H_2

The Ti with the fresh surface prepared from TiH_2 by dehydrogenation. This Ti absorbed H_2 even at around 40 °C without any catalysts and heat-activation. On the other hand, Mg with fresh surface did not react with H_2 even heating up to 250 °C. These results indicated the difference of the surface properties between Ti and Mg. This difference is consistent with the general understanding, where *d*-electron is active for H_2 dissociation. However, the Ti surface was easily inactivated even in the glove box after 1 day because of its high reactivity. As a result, the hydrogen absorption was inhibited by the oxide layer, and heat-activation was required to realize the reaction after formation of the oxide layer. Thus, to improve the hydrogen absorption properties of Ti, the suitable surface modification is required to realize the selective reaction for H_2 without the degradation of surface activity due to oxygen and water.

(2) Surface modification by transition metals and oxides to make active sites

Various kinds of solid additives, which were typical metal and oxide catalysts for hydrogen dissociation, were dispersed on the Ti surface to make an active site for the hydrogenation, and the hydrogenation properties were evaluated. However, these samples absorbed H_2 at more than 200 °C. Thus, it was found that the influence of surface oxidation on H_2 absorption by Ti was much larger than effects of the additives. The above results also suggested that the special surface modification to prevent oxidation was required for selective reaction of Ti with H_2.

(3) Surface modification by organic solvents and graphite to prevent the surface oxidation

Ball-milling with organic solvents was performed as another method for modifying the Ti surface. Hydrogen could be absorbed by $Ti_{Acetone}$ and Ti_{Xylene} at around room temperature even after keeping those samples for 3-4 days in the glove box. These results indicated that H_2 could selectively penetrate into the surface and react with Ti. The degradation tendencies of hydrogenation reactivity of $Ti_{Acetone}$ and Ti_{Xylene} were different. The reactivity of $Ti_{Acetone}$ with H_2 was degraded gradually, and this tendency could be explained by the porous inorganic membrane model. And, Ti_{Xylene} degraded suddenly after 3 days, which could be understood by the adsorbent model. Raman spectroscopy revealed that the chemical state of carbon formed on the Ti surface was important for the selective reaction. In addition, the TiC_x layer was observed in $Ti_{Acetone}$ by Raman spectroscopy and TEM observation. On the other hand, the Raman spectrum of Ti_{Xylene} indicated the formation of amorphous carbon on the Ti_{Xylene} surface. Furthermore, the hydrogenation properties of Ti could be more improved by graphite. The reactivity of $Ti_{Graphite}$ was kept at least 7 days, indicating that graphite showed the superior surface modification effects for Ti. To understand the effective factors of surface modification for improvement of the hydrogenation properties of Ti, the characterization of the $Ti_{Graphite}$ surface was carried out by Raman spectrometry, XPS measurement, and TEM observation as well as TG and XRD measurements. The TG and XRD measurements suggested that the amount of TiC formed on the Ti surface by heating was much larger than that of Ti modified by organic solvents, namely carbon was effectively doped on the Ti surface. Raman spectroscopy showed the transformation of crystallite graphite into turbostratic carbon by ball-milling with Ti. Further, the XPS results indicated that TiC_x was formed and the turbostratic carbon covered on the $Ti_{Graphite}$ surface. These facts were also confirmed by TEM observation. TEM results indicated the existence of amorphous carbon on the $Ti_{Graphite}$ surface, and the existence of TiC_x layer at the interface between the carbons and Ti bulk. As a summary, it was clarified that the selective reaction with H_2 by $Ti_{Graphite}$ was achieved by the mixed carbon phase (turbostratic carbon and amorphous) with the hydrophobic adsorbent effects for water and oxygen and the TiC_x layer with the molecular sieving effects.

From the above study, the fundamental reaction between Ti and H_2 could be understood. It can react with H_2 even without any catalyst and heat-activation. The influence of the surface oxidation on the hydrogenation of Ti was larger than the effects of solid additives. The functional surface could be synthesized by ball-milling with organic solvents. It was thought that the mixed turbostratic/amorphous carbon phase and the TiC_x layer have H_2 separation effects. These carbons are effectively generated from graphite, and the superior hydrogen absorption properties of Ti was achieved by ball-milling with graphite. By understanding the essential hydrogenation ability of Ti, it was proposed that the suppression of the surface oxidation to keep the active surface and simultaneously selective reaction with H_2 were important for Ti.

Acknowledgements

I would like to extend my sincere thanks to my supervisor, Professor Dr. Takayuki Ichikawa for his helpful guidance, suggestions. Thanks to him, I had lot of great experience in my doctoral course. I would like to special thanks to Professor Dr. Yoshitsugu Kojima for a lot of valuable discussion, comments, and suggestions. I learned many things about research from him. I would like to express my gratitude to Associate Professor Dr. Hiroki Miyaoka for his helpful guidance, suggestions. I always discussed with him when I was in trouble with my research, writing paper, presentation. I am special thanks to co-authors of my research paper, Assistant professor Dr. Yuki Nakagawa in Hokkaido University, Professor Dr. Norio Ogita in Hiroshima University, Mr. Yuya Hayashi in Hokkaido University, Associate Professor Dr. Shigehito Isobe in Hokkaido University, and Professor Dr. Tamaki Shibayama in Hokkaido University for their cooperation. Finally, I would like to grate thanks to my colleagues of laboratory, Mr. Tomoyuki Ichikawa, Ms. Misao Mukoda, Ms. Saori Inagaki, Mr. Hiroyuki Kurihama, Associate Professor Dr. Ankur Jain, Assistant Professor Dr. Machi Kanna, Assistant Professor Dr. Rini Singh, Dr. Rajesh Kumar, Dr. Shotaro Yamaguchi, Dr. Keita Nakajima, Dr. Hiroki Uesato, Dr. Yasuhiro Matsumura, Mr. So Hamamoto, Ms. Pratibha Pal, Ms. Fangqin Guo, Mr. Pankaj Kumar Singh, Mr. Fernando Cano-Banda, Mr. Masakuni Yamaguchi, Mr. Hiroyuki Gi for their kind help in my doctoral course.

Published Papers

[1] Room-Temperature Hydrogen Absorption of Titanium with Surface Modification by Organic Solvents

K. Shinzato, S. Hamamoto, H. Miyaoka, T. Ichikawa

The Journal of Physical Chemistry C, **123** (32), pp 19269-19274 (2019.7.10).

[2] Metal Hydrides and Related Materials. Energy Carriers for Novel Hydrogen and Electrochemical Storage

A. El Kharbachi, E.M. Dematteis, **K. Shinzato**, S.C. Stevenson, L.J. Bannenberg, M. Heere, C. Zlotea, P.Á. Szilágyi, J.-P. Bonnet, W. Grochala, D.H. Gregory, T. Ichikawa, M. Baricco, B.C. Hauback

The Journal of Physical Chemistry C, **124** (14), pp 7599-7607 (2020.4.9).

[3] Surface modification effects of graphite for selective hydrogen absorption by titanium at room temperature

K. Shinzato, Y. Nakagawa, S. Hamamoto, Y. Hayashi, H. Miyaoka, S. Isobe, T. Shibayama, N. Ogita, T. Ichikawa

Chemical Communications, **56** (53), pp 7237-7240 (2020.5.26)